PHYSIK-DEPARTMENT
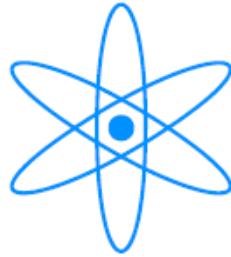
Thin films of crystalline diblock copolymers: Crystallization under different confinements

**Dissertation
von
Charles Darko**

TECHNISCHE UNIVERSITÄT MÜNCHEN

Technische Universität München
Physik Department E13

Thin films of crystalline diblock copolymers: Crystallization under different confinements

Charles Darko

Vollständiger Abdruck der von der Fakultät für Physik der Technischen Universität München zur Erlangung des akademischen Grades eines

Doktors der Naturwissenschaften (Dr. rer. nat.)

genehmigten Dissertation.

Vorsitzender: Univ.-Prof. Dr. R. Netz

Prüfer der Dissertation:

1. Univ.-Prof. Chr. Papadakis, Ph.D.

2. Priv.-Doz. Dr. P. A. Feulner

Die Dissertation wurde am 09.06.2008 bei der Technischen Universität München eingereicht und durch die Fakultät für Physik am 22.07.2008 angenommen.

This dissertation is dedicated to my dear wife
Ivy Osei-Mensah Darko
& to my son
Mario Nii Amoo Darko

Abstract

This research work focuses on the interplay between crystallization and mesophase formation and their influence on the surface and internal structures of thin films of diblock copolymers. The aim is to relate the crystallization mechanisms to the surface and the internal structures formed. In this view, the crystallization mechanisms in *unconfined*, *softly confined* and *strongly confined* thin films environment were studied.

Combining results from optical and atomic-force microscopy as well as from grazing-incidence small- and wide-angle X-ray scattering methods, a detailed view of the surface and internal structures of semicrystalline thin films could be obtained providing new information for improved understanding of polymer crystallization.

For *unconfined crystallization*, three thin films from a symmetric low molar mass Poly(styrene-*b*-ethyleneoxide) (PS-*b*-PEO) diblock copolymer were prepared and were crystallized at three different temperatures. The crystal growth rates, the resulting surface textures and the orientation of the PEO chain were vastly different. At low crystallization temperature (room temperature), the crystal growth rate is high but the crystals grow with a mean inclination angle of 35° from the film normal, building small, slightly differently oriented crystalline domains along the growth front. These growth mechanisms are attributed to repeated nucleation events at the growth front as demonstrated previously in phase-field simulations. It promotes a granular and comparatively rough surface texture. At high crystallization temperature, i.e. temperature just below the melting point, only very few nuclei are formed, and the crystal growth rate is low. Large crystallites grow with the chain stems perpendicular to the film normal. The high mobility of both blocks at this elevated temperature enables the lateral diffusion of the chains towards the growth front promoting large crystalline domains. The resulting surface morphologies consists of terraces with height comparable to a monolayer of once-folded PEO block oriented perpendicular to the substrate plane. Films crystallized between the low and high temperatures represent an intermediate case. In those films, the surface morphologies and the

growth rates are comparable to films crystallized at low temperatures but the lamellar repeat distance is similar to the film crystallized at high temperatures. This is attributed to the PEO stems having intermediate orientations.

For the *crystallization with soft confinement*, one thin film was prepared from a low molar mass poly(isoprene-*b*-ethyleneoxide) (PI-*b*-PEO) diblock copolymer. The PEO blocks form hexagonally arranged cylinders lying in the film plane confined in the PI matrix. The PI matrix, which is rubbery, provides a soft confinement. The nucleation rate for crystal formation was low, which we attribute to the confinement of the short PEO chains. Crystallization of the PEO chains, once nucleated, causes destruction of the hexagonal morphology and transforms it into lamellar morphology. This process is only completed after 148 days. The repeat distances before and after crystallization as well as the surface terrace height are comparable which suggest the presence of well defined repeat distances within the thin films.

To investigate the *strongly confined crystallization*, two thin films from a symmetric high molar mass PS-*b*-PEO diblock copolymer were prepared and were crystallized at two different temperatures. The surface morphologies did not change with temperature. With this long PEO chain, it was difficult for the chains to fold several times to form crystals. Moreover, the glassy amorphous PS hinders the chain diffusion. Only local movements of the chains allowed some ordering of these chains to form crystals within the films.

Our results show that a detailed structural analysis can explain the observed surface morphologies and relate them to the different mechanisms of crystal growth. Under different nano-confinement, the thin film geometry used offers an ideal possibility to correlate detailed structural analyses on various length scales with the direct-space observation of crystal growth via microscopy techniques.

Preface

The present report is the result of a Ph.D.-work, which was started in June 2005 at the Physik Department E13, Technische Universität München, under the supervision of Prof. Dr. Christine Papadakis. Some of the samples used were provided by Prof. Günter Reiter, CNRS-UHA, Mulhouse, France, Prof. S. Förster, Universität Hamburg, Hamburg, Germany, while others were purchased from Polymer Standard Service, Mainz. GISAXS experiments were performed both at BW4 beamline in Hamburger Synchrotronstrahlungslabor (HASYLAB) and at D-line at the Cornell High Energy Synchrotron Source (CHESS), Cornell University, Ithaca, New York. GIWAXS and GIXD experiments were performed at Risø National Laboratory, Roskilde, Denmark and at BW2 beamline in HASYLAB, respectively.

Acknowledgements

First and foremost, I wish to thank sincerely my supervisor Prof. Dr. Christine Papadakis for accepting me as her Ph.D. student, for her competent direction, valuable insights and continuous support both within and beyond this dissertation work. Her excellent academic guidance has made this work possible.

I thank Prof. Dr. Peter Müller-Buschbaum, acting chair person of the Physik Department E13, for his encouragement, help and advice.

I wish to express my sincere thanks to Prof. Günter Reiter at the Institut de Chimie de Surfaces et Interfaces, CNRS-UHA, Mulhouse, France for his encouragement, helps, advice and fruitful discussions.

My special thanks to Prof. Dag. W. Breiby at the Department of Physics, Norwegian University of Science and Technology, Trondheim, Norway and Dr. Jens W. Andreasen at Risø National Laboratory for Sustainable Energy, Technical University of Denmark, Roskilde, Denmark for their assistance, cooperation and fruitful discussions during the GIWAXS experiments and the simulation of the diffraction patterns.

I wish to acknowledge Dr. Detlef-M. Smilgies at the Cornell High Energy Synchrotron Source (CHESS), Cornell University, Ithaca, New York and Dr. Stephan V. Roth at the Hamburger Synchrotronstrahlungslabor (HASYLAB) for their enormous help, assistance and fruitful discussions during the GISAXS experiments.

Many thanks go to all past and present E13 group members especially Dr. Tarik Mehaddene, Dr. Tune Bonné, Dr. Edith Maurer, Dr. Emmanuel Longueteau, Dr. Volker Körstgens, Dr. Ezzeldin Metwalli Ali, Dr. Amit Kulkarni and Zhenyu Di for their help and kindness.

Contents

Chapter 1

Introduction

1.1   Semicrystalline diblock copolymers

Diblock copolymers are polymers which consist of two chemically different polymer chains joined at one end by a covalent bond which are able to microphase-separate into nano- and micro-phase structures (hexagonal, lamellar, gyroid etc.) due to their ability to self-assemble [1,2,3,4,5]. The structures formed depend on the variation in block lengths. In thin film geometry, the thin film offers confinement to diblock copolymers which induces macroscopic orientation. The orientations of these structures can be tuned to generate unique surface topographies enabling diblock copolymer thin films to serve as templating tools in many fields of nanoscience and technology such as surface patterning [6], lithography [7], and for the fabrication of quantum dots [8,9], nanowires [10,11], magnetic storage media [12], nanoholes [13] and silicon capacitors [14]. The ordering of structures are influenced by factors such as the substrate used [15], film thickness [16] and the presence of an external electric field [17,18].

In semicrystalline diblock copolymers (i.e. having one amorphous and one (semi-) crystalline block), the final structure formed depends on the competition between three transitions: the order-disorder transition (ODT) of the diblock copolymer, the crystallization of the crystallizable block, and the glass transition of the amorphous block [19,20,21,22,23,24,25,26,27,28,29]. Depending on the ODT temperature, T_{ODT}, the melting temperature of the crystallizable block, T_{m}, and the glass transition temperature of the amorphous block, T_{g}, both unconfined and confined crystallization have been observed (Fig. 1.1). Confined crystallization

involves two cases: Below T_g (i.e. $T_{ODT} > T_g > T_x$, where T_x is the crystallization temperature), crystallization is completely confined within the pre-existing morphology (Fig. 1.1*a*), whereas above T_g (i.e. $T_{ODT} > T_x > T_g$), it is solely governed by the segregation of two blocks in which crystallization occurs 8soft confinement). For unconfined crystallization (i.e. $T_x > T_{ODT} > T_g$), the phase separation between the blocks is driven by crystallization of the crystallizable block, i.e. the crystallization process dominates the microphase separation (Fig. 1.1*b*).
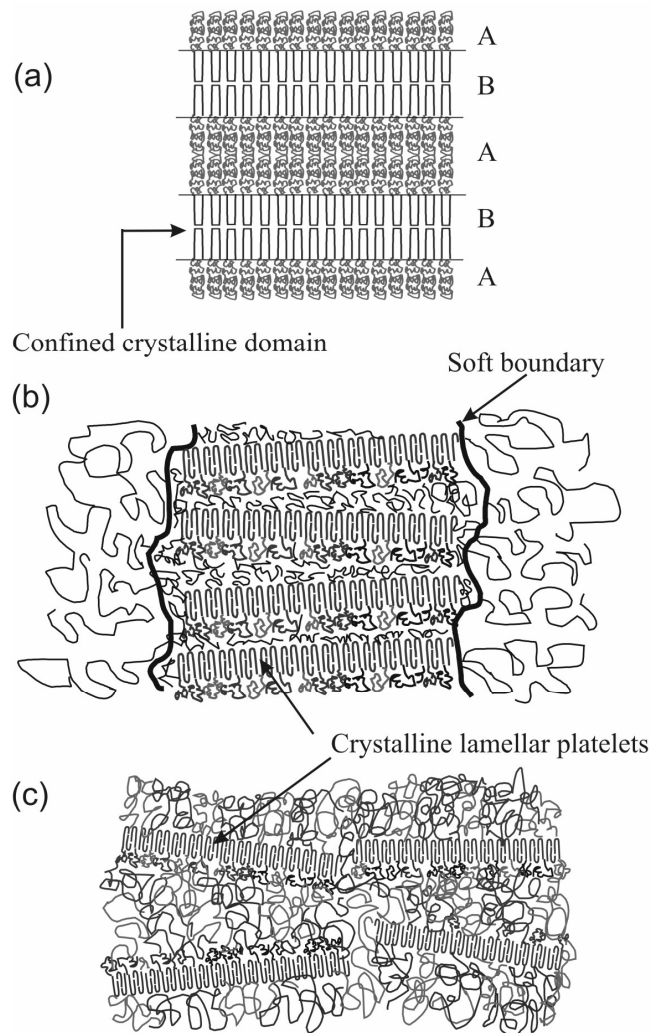
Figure 1.1   Schematic representation of hard confined (*a*), soft confined (*b*) and unconfined (*c*) crystallization in diblock copolymers. *A* and *B* symbols represent the amorphous and crystalline domain.

If crystallization and the microphase separation of the two blocks start at the same time with small and comparable rates, the dynamic coupling and the kinetic competition between crystallization and microphase separation can result in more complex morphologies [30].

In polymer crystallization, after nucleation, the long chain macromolecules crystallize by chain folding into thin crystalline lamellar with thickness orders of magnitude smaller than extended chain dimensions [31,32,33]. In general, crystal growth rate depends on the difference between the equilibrium melting temperature, $T_m°$ and T_x, i.e the degree of supercooling (Fig. 1.2) [34,35,36]. For weak supercooling, the growth rate is low due to a low thermodynamic driving force towards crystallization. For strong supercooling, the driving force is stronger and hence the growth rate is higher. However, the growth rate also decreases when T_x approaches T_g because the mobility of the chains is decreased. How fast or slow crystalline polymers fold to form crystals affects the attached amorphous polymers in semicrystalline diblock copolymers. The growth rate therefore influences the competition between chain folding of the crystallizable block and the stretching of the amorphous block in semicrystalline diblock copolymers. The competition occurs in order to accommodate the interfacial area required by the crystalline block. The final morphology depends on how fast and under which constraints (glassy or rubbery medium) chain folding occurs.
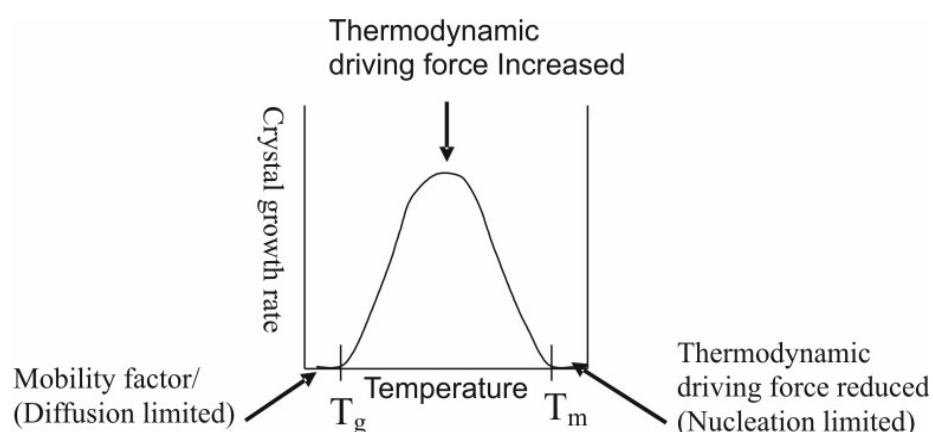
Figure 1.2   Dependence of crystal growth rate on crystallization temperature.

1.2 Present studies

The main goal of the work is to monitor the interplay between crystallization crystallization and mesophase formation in unconfined, soft confined and hard confined crystallization in thin films of diblock copolymer.

Unconfined crystallization in thin films of diblock copolymer

In thin films of semicrystalline diblock copolymers, the surface morphologies formed depend on the degree of folding of the crystalline block, the orientation (tilt) of the crystallites with respect to the mesophase interface and the degree of stretching of the amorphous block. In effect, space requirements of the two blocks at the mesophase interface influence the resulting surface textures. It is desirable to obtain complete information on various parameters contributing to the structure formation.

Poly(styrene-*b*-ethyleneoxide) (PS-*b*-PEO) diblock copolymer is an example of a semicrystalline copolymer where the PEO is the crystalline block and the PS is the glassy amorphous block (Fig. 1.3). The glass transition temperature of the PS, $T_{g,PS}$, and the melting temperature of the PEO, $T_{m,PEO}$, depend on the molecular weight [37].
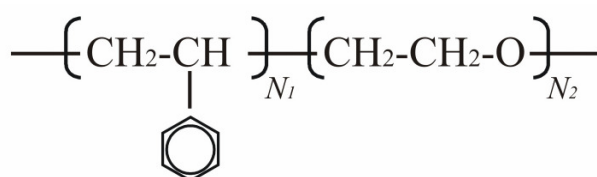
Figure 1.3 Structure of the poly(styrene-*b*-ethyleneoxide) (PS-*b*-PEO) diblock copolymer. Symbol N_1 and N_2 represent the degree of polymerization of PS and PEO monomer, respectively.

In the bulk studies of PS-*b*-PEO systems, PEO crystals as well as its crystalline orientations have been investigated in nanoconfined lamellar, hexagonally perforated layer and gyroid structures [30,38,39,40,41,42,43]. It was noted that PEO crystalline orientation depends on T_x. In lamellar one-dimensional

4

confinement [39], the PEO crystallizes with the *c*-axis changing from random to perpendicular, then inclined and finally parallel to the lamellar surface normal such that each T_x corresponds to a uniform orientation rather than a mixture of different crystal orientations (Fig. 1.4). In some cases [38], the lamellar phase formed was driven by the crystallization of PEO at low temperatures.

In thin films, a number of surface investigations including X-ray reflectometry as well as theoretical interpretations have been made on PEO crystallization [44,45,46,47]. Particularly, the PEO crystallization and its influence on the surface morphology in PS-*b*-PEO diblock copolymer systems were studied [48,49,50]. The observed morphologies and its temporal evolution directly to the molecular processes and the kinetics of the crystal growth were discussed. It was noted that changes in surface morphology with time were due to the difference in thermal histories and were consequences of the metastable nature of the polymer crystals. The growth rate of the PEO crystals was found to depend on the film thicknesses. The mechanism responsible for the differences in the growth rates were discussed in terms of availability of crystallisable polymers chains and the controlling influence of diffusion towards the crystal front.

In all the above thin film investigations, fundamental questions such as the crystalline orientations, the mesophase structures/orientation and crystal growth mechanisms within the thin film geometry influenced by the T_x, were not reported. Moreover, only surface techniques such as optical (OM) and atomic force microscopy (AFM) were employed. In some cases, X-ray reflectometry were used.

In this study, we combine surface studies with scattering techniques in order to relate the crystal growth rate and the resulting surface textures to the orientation and spacings of the mesoscopic structures and crystalline orientation within the film. This is to gain thorough understanding of the crystallization mechanisms and its influence on the surface morphology. In view of this, we have studied the unconfined PEO crystallization and have compared their chain formation processes and the resulting surface patterns.

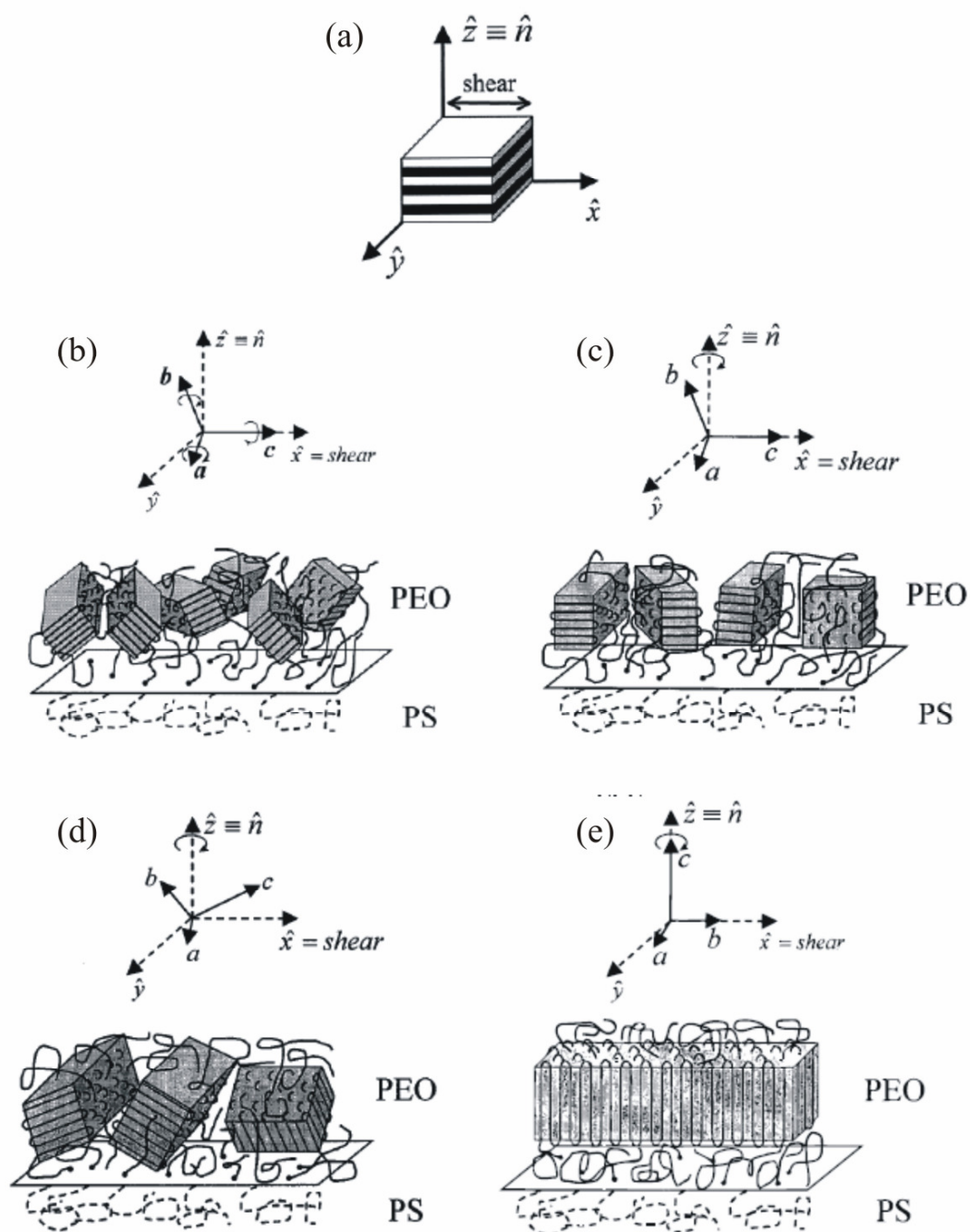**Figure 1.4** Schematic diagram of shear-aligned PS-*b*-PEO sample showing the shear lamella geometry (*a*) and PEO crystal chain orientation within the confined lamella with the chain stems (*c*-axis) being random at $T_x \leq$ -50°C (*b*), parallel at -50°C $\leq T_x \leq$ -10°C (*c*), inclined at -5°C $\leq T_x \leq$ 30°C (*d*), perpendicular at $T_x \geq$ 35°C, with respect to the film/substrate interphase. Adopted from ref 39.

Soft confined crystallization in thin films of diblock copolymer

In soft confined block copolymer systems, as shown on figure 1.1*b*, disruption of the pre-existing morphology during/after crystallization have been investigated [51,52,53,54,55,56,57,58,59,60]. For instance, the original hexagonal microphase-separated morphology was destroyed by chain folding upon crystallization promoting non-ordered lamellae [51]. This was realized when the sample was cooled below the melting point of the crystallizable block. In other studies, disruption of conventional qyroid amorphous microdomain morphology upon crystallization leading to layered morphology was noted [52,54]. Interestingly, the morphology produced by crystallization in soft confined hexagonal-packed cylinder was noted to depend on the thermal history [53]. In this view, it was found that fast cooling kinetically confines crystallization to the cylinders, while slow cooling results in complete disruption of the cylindrical melt mesophase upon crystallization, leading to a lamellar morphology with larger domain spacing. In the above investigations, crystallization of the crystallizable block proceeded more or less immediately after cooling from the melt phase to the solid phase. In a system where much time (days to months) is needed to induce crystallization, the breakout effect cannot be observed at once.

We present here, the time dependent crystallization behaviour in low molar mass thin film of cylinder-forming poly(isoprene-*b*-ethyleneoxide) (PI-*b*-PEO) diblock copolymer (Fig. 1.5) with PEO being the minority block. PI-*b*-PEO systems have been studied and have been used as template for voltaic cells [61]. PI is a rubbery amorphous block and its glass transition temperature, $T_{g,PI}$, depend on the molecular weight [37].

$$-\left[CH_2\text{-}\underset{\underset{CH_3}{|}}{CH}\text{=}CH\text{-}CH_2 \right]_{M_1} \left[CH_2\text{-}CH_2\text{-}O \right]_{N_2}-$$

Figure 1.5   Structure of the poly(isoprene-*b*-ethyleneoxide) (PI-*b*-PEO) diblock copolymer. Symbol M_1 and N_2 represent the degree of polymerization of PI and PEO monomer, respectively.

In our studies, long time was required to crystallize the system in which we focused on the disruption mechanism of the microdomain by PEO crystallization. The thin film geometry allowed us to visualize the growth of the PEO crystals within the PI domain. In similar asymmetric systems where PEO crystallizes within rubbery domains, the orientations of the crystalline chain stems were not given full consideration in order to relate them to the morphologies/mesophases obtained [55,57,58,60]. Here, we combined surface investigations by optical (OM) and atomic force microscopy (AFM) with scattering techniques to study the surface morphology and the microdomain structures within the thin films before and after the PEO crystallization. While grazing incidence small- and wide-angle X-ray scattering (GISAXS and GIWAXS) enabled us to characterize the buried mesoscopic structures and crystalline orientations, respectively within the thin film.

Hard confined crystallization in thin films of diblock copolymer

Although polymer crystallization under rigid confinement in block copolymers have been studied, little is known on a very long crystallisable chain confined in a very strong glassy environment [62,63]. This is what we called *hard confinement*. There are characteristic behaviours and properties in the crystallization processes of the hard confined system, which are different from those of the normal rigid crystallization confinement. Such characteristics behaviour and properties are the crystallinity, the orientation of chains and the chain folding mechanisms. For example, in the figure 1.6 below, the illustration depicts the frustration in maintaining the crystallization condition of the long crystallisable chains within the strong glassy amorphous confinement. Thus, it is very difficult to estimate the role and the effect of various factors individually and to obtain systematic knowledge of the ordering mechanism.
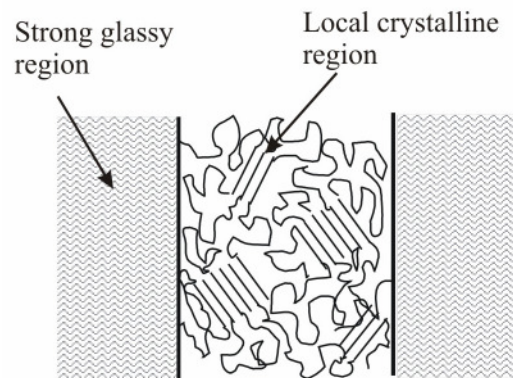
Figure 1.5 Illustration of crystallization in hard confinement. Chain folding is frustrated by the very long crystallisable chain and the confinement by strong glassy amorphous domain.

In view of the above problem, we have investigated crystallization of very a long PEO chain confined in a very strong glassy PS domain in thin films. Focus was cantered on the local chain movement within thin films and its influence on the surface morphologies. We hope to gain some understanding under such frustrations in chain folding.

Chapter 2

Experimental

2.1 Sample preparation

The thin films were prepared differently in accordance to the goal of the investigations. The following describe the sample preparations used in the various studies.

2.1.1 Unconfined crystallization

For soft crystallization confinement, we have investigated PEO crystallization in PS-*b*-PEO diblock with block molar masses of 3,000 g/mol each resulted in lamellae morphology. The polydispersity is less than 1.1. From DSC at a rate of $\pm$ 10K/min, the melting point of PEO, T_{mPEO}, was found between ~45°C and 55°C, depending on T_x. The T_g of PS is ~67°C. The T_{ODT} was found to be -90°C (i.e. unconfined at room temperature) calculated from the relation $\chi_f = 29.8/T$ -0.0299 [64] as shown in appendix A, where χ_f is the Flory-Huggins interaction parameter. The diblock copolymer thin films were prepared by spin-coating from toluene solutions (20 mg/ml) onto UV/ozone cleaned silicon wafers. The film thickness was ~100 nm, obtained using ellipsometry.

After spin-coating, the films were annealed at 62°C for a few minutes in dry atmosphere (using TS62 heating plate from Instec, Inc., temperature resolution of 0.1°C), i.e. above the melting point of PEO while monitoring the morphological changes of the surface with optical microscopy (Fig. 2.1*a*). Fully crystallized thin films were obtained following the protocol (Fig. 2.1*b*): (i) heating the films to

62°C, i.e. slightly above T_m for about 5 minutes to ensure complete melting of the PEO domain, (ii) quenching to the chosen T_x, i.e. 25, 40 or 50°C with typical cooling rates of 50 K/min, (iii) leaving the films at this temperature until no further changes were observed. The films prepared are as shown on table 2.1.
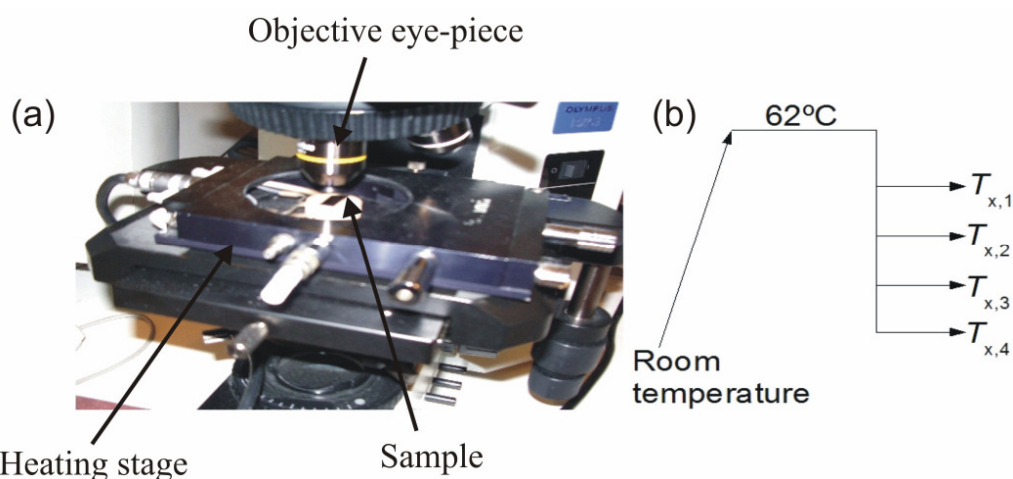
Figure 2.1 (*a*) Sample preparation setup showing the heating stage, the sample and the microscope objective eye-piece on top of the sample. (*b*) Crystallization procedure in which films are heated to 62°C and then quenched to a preset temperature T_{x1}, T_{x2} or T_{x3}.

Table 2.1. Films prepared for soft crystallization investigations

Symbols	Sample	Molar Mass (g/mol)	Film thickness (nm)	T_x (°C)
$T_x = 25°C$	PS-*b*-PEO	3k -3k	~100	25
$T_x = 40°C$	PS-*b*-PEO	3k -3k	~100	40
$T_x = 50°C$	PS-*b*-PEO	3k -3k	~100	50

2.1.2 Soft confinement crystallization

The poly(isoprene-*b*-ethyleneoxide) (PI-*b*-PEO) diblock copolymer was synthesized within the group of Prof. S. Förster. The blocks have weight-average molar masses of 2.1 and 1.1 kg/mol with a polydispersity index of about 1.1. The

volume fraction for PEO, f_{PEO}, is 0.23 resulted in a hexagonal morphology. Using differential scanning calorimetry at a rate of ±10°C/min, the melting point of PEO, $T_{m,PEO}$, was found to be ~30°C. The T_g of PI, $T_{g,PI}$, was found to be below room temperature (i.e. -53°C) while the PI-*b*-PEO block systems are well known to form a highly phase separated microdomains [65,66]. However, we did not observed any changes upon heating to 62°C. Hence, soft confined system was obtained.

The diblock copolymer thin films were prepared by spin-coating toluene solutions (25 mg/ml) onto UV/ozone cleaned silicon wafers. The film thickness was 110 nm estimated using ellipsometry. After spin-coating, the films were annealed at 62°C for a few minutes in dry atmosphere (using a heating plate from Instec, Inc., temperature resolution of 0.1°C), i.e. above the melting point of PEO, and then quenched to room temperature. The crystallization of the PEO block was monitored using optical microscopy for several months (i.e. 148 days) until no more changes occurred. It took a long time for crystallization to begin. We have followed the long time crystal growth process of one of the prepared film as shown in table 2.2.

Table 2.2. Films prepared for soft confinement crystallization investigations

Symbols	Sample	Molar Mass	Film thickness	Annealed temperature
		(g/mol)	(nm)	(°C)
IEO	PI-*b*-PEO	2.1k -1.1k	~110	62

2.1.3 Hard crystallization confinement

For hard crystallization confinement, we have monitored PEO crystallization in PS-*b*-PEO having molar masses of 109, 000 g/mol each with polydispersity index of 1.09. The sample was purchased from PSS, Mainz, Germany. The volume fraction for PEO, f_{PEO}, is 0.46. Using DSC at a rate of ± 10°C/min, the T_{mPEO} was found to be ~62°C (onset of melting ~38°C) and the T_g of PS is ~was found to be

~98°C. The T_{ODT} was found to be 841°C (see appendix A), i.e. highly confined crystallization is expected.

Two thin films were prepared by spin-coating toluene solutions onto UV/ozone cleaned Si(100) wafers having equal thicknesses of 170 nm determined by ellipsometry. The films were later annealed at 120°C overnight. To control crystallization within the rigid matrix, and following the protocol of the film preparation in the soft confinement, the films were heated at 62°C for about 10 minutes and then quenched back to $T_x = 25$°C and 40°C as shown in table 2.3.

Table 2.3. Films prepared for hard crystallization investigations

Symbols	Sample	Molar Mass (g/mol)	Film thickness (nm)	T_x (°C)
$T_x = 25$°C	PS-*b*-PEO	109k -109k	~170	25
$T_x = 40$°C	PS-*b*-PEO	109k -109k	~170	40

2.2   Experimental techniques

Under this section, the experimental techniques used in the work were described. They were optical and atomic-force microscopy for surface analysis, differential scanning calorimetry (DSC) for obtaining thermodynamic data of the samples and ellipsometry for estimating the film thicknesses. Within the thin films, grazing-incidence small-angle X-ray scattering (GISAXS) was used to obtain the buried large scale structures, grazing-incidence wide-angle X-ray scattering (GIWAXS) was used for determining the crystalline orientation and grazing-incidence X-ray diffraction (GIXD) for estimating the crystallites characteristic length scales.

2.2.2.1 Optical microscopy (OM)

Optical microscope is a type of microscope which uses visible light and a system of lenses to magnify images of objects too small to be seen with the naked eye [67].

2.2.1.1 Principles of OM

In this method, light is directed vertically through the microscope objective and reflected back through the objective to an eyepiece or a camera. The sample surface is uniformly illuminated by incident light rays directed perpendicular to the sample surface as shown in figure 2.3. Light reflected back toward the objective lens is collected and focused on the eyepieces or the camera to form the observed image. The magnification of the sample image is obtained by light refraction through combinations of lenses, comprising the objectives and the eyepiece or the camera. Image contrast is enhanced with differential interference contrast (DIC) methods (dark and bright field contrast can also be used). In the differential interference contrast, contrast is produced between features with different heights and topographic orientations resulting in a three-dimensional image.
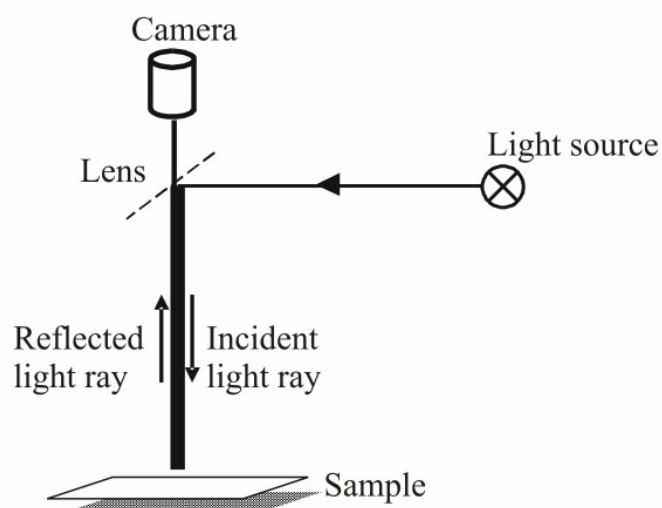
Figure 2.3 Principle of OM in a reflective mode. The light is refracted to the sample and the reflected light collected by the camera.

2.2.1.2   Experimental

The optical microscope (i.e. Olympus BX51 optical microscope and Axio Imager from Zeiss with a DIC and having lateral resolutions of about 1 µm) was placed on top of the heating stage as described in section 2.1.1.1. Objectives lens settings of typically 50X and 20X were used providing images sizes of about 170 µm × 130 µm for detail viewing of the surface and 860 µm × 650 µm for global viewing of the surface, respectively. No polarization or other phase contrast was used. Contrast was due to the interference of the reflected white light at the substrate/film and film/air interface, resulting in well-defined interference colours. This was sufficient to allow visualization of crystal growth at a rate of 2 min per image using a *c*-mount camera. To monitor the growth rate, contrast was generated between the crystalline and the amorphous regions which were due to the differences in reflectivity indexes of the two regions as shown in figure 2.4. Using integrated software, the lateral feature dimensions as well as the area/volume of particles could be measured.

Figure 2.4   Optical micrograph showing growth of a crystalline domain at a rate of about 0.8 µm/sec. (*a*) Measured at $t_0 = 0$ min, (*b*) at $t_0 = 1$ min and (*c*) $t_0 = 3$ min.

2.2.2 Atomic-force microscopy (AFM)

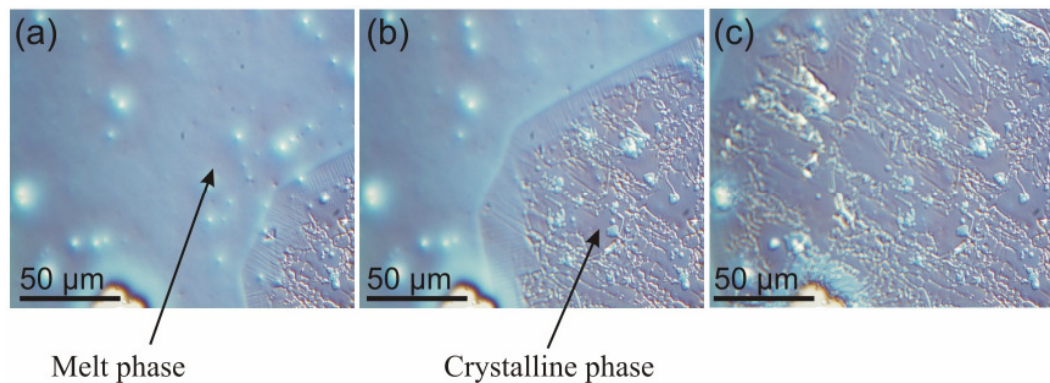The AFM is one of the foremost tools for imaging, measuring and manipulating matter at the nanoscale. Piezoelectric elements that facilitate tiny but accurate and precise movements on (electronic) command are what enable the very precise scanning [68].

2.2.2.1   Principles of AFM

The AFM consists of a microscale cantilever with a sharp tip (probe) at its end that is used to scan the specimen surface. The cantilever is typically silicon or silicon nitride with a tip radius of curvature on the order of nanometers. The tips and cantilevers come with a wide range of properties. The properties of an AFM tip are depending on material size and shape and are characterized by its spring constant or resonance frequency. The AFM can be operated in a number of imaging modes, depending on the application. In general, possible imaging modes are divided into static or contact modes (the static tip deflection is used as a feedback signal) and a variety of dynamic modes (the cantilever is externally oscillated at or close to its resonance frequency). For imaging of soft and sensitive materials like biological surfaces or unstable surface features and in order to avoid sample deformation, the so-called tapping mode atomic force microscopy (TM-AFM), also referred to as intermittent contact mode AFM are used [69]. In this dynamic mode, the cantilever with the tip was modulated to vibrate close to its resonance frequency with free amplitude in the range of 10 to 150 nm. Phase imaging mode TM-AFM could also be obtained. This technique was based on energy dissipation during tapping. Areas with different viscoelasticity or adhesion shifted the time response of the oscillating tip as the tip "sticked" to the surface and a relative difference in phase was produced.

2.2.2.2 Experimental

A TM-AFM digital instrument (Multimode JSPM-5200 scanning probe microscope, Joel Ltd) was used. A diode laser was focused onto the back of this reflective cantilever. When the tip of the cantilever was brought into proximity of the film surface, the forces between the tip and the film causes deflection of the cantilever according to Hooke's law. The deflection of the cantilever transferred feedback to the photodiode which helps maintain some contact between the tip and the film surface automatically. As the tip scans the surface of the sample, moving up and down with the contour of the surface, it causes deflection in the laser beam which is monitored by the array of photodiodes. The photodetector measured the difference in light intensities between the upper and lower photodiodes, and converted it to voltage. These changes in the voltages were then converted into images.

The sample was mounted on a piezoelectric tube that can move the sample in the z direction for maintaining a constant force, and the x and y directions for scanning the sample. The basic components of the multimode AFM are schematically illustrated in figure 2.2. In our studies, we used silicon made cantilevers (NSC35/ABS) purchased from MikroMasch. The scan rates were between 2.8 and 9.3 Hz. A force constant of 3.5 N/m and a resonance frequency of about 135 kHz were used. Measurements were performed at room temperature.
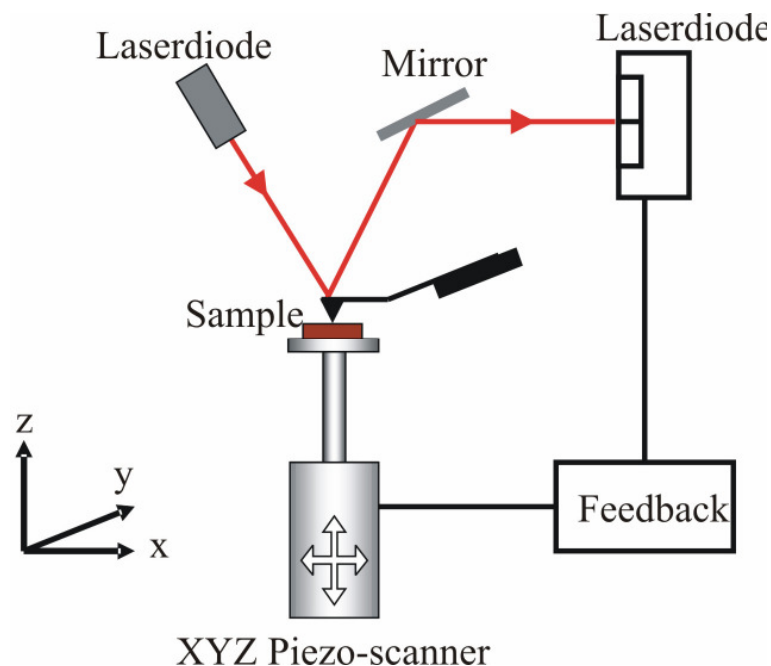
Figure 2.5   General scheme and basic components of a multi-mode AFM. A fine tip is mounted on a cantilever spring and scanned over the surface. The vertical deflection of the cantilever is detected by reflecting a laser beam onto an array of photodiodes. The photodiode signal is used to drive a system which controls the movement of the piezo xyz-translator. In this manner, the applied force between the tip and the sample can be kept constant within some tens of piconewtons.

2.2.2.3   Data Analysis

In our case, digital images obtained from the AFM were stored as tiff files. The raw data were later processed using the WinSPM processing software. The software enables adjusting the colour scale, the background brightness gradient and also corrects the flatness of the image horizontal plane. Information on the surface such as the surface topography height, grain sizes as well as surface roughness could be obtained. In obtaining the surface topography step-heights, line profiles were made on specific location of interest and information were obtained with a resolution of about 4%.

When using the AFM and interpreting the results, we had to be aware of possible artifacts caused by vibrations, convolution of surface features with the tip geometry, deformation or scratching of the surface by the force load, drifts or

contamination of the tip. These disadvantages could be avoided in most of the cases by careful alignment of the sample and avoiding strong approaching force of the tip towards the surface so as to gently touch the surface.

2.2.3 Ellipsometry

Ellipsometry is a very sensitive measurement technique that uses polarized light to characterize thin films, surfaces, and material microstructure [70]. We have used the ellipsometry estimating the film thickness.

2.2.3.1   Principles of Ellipsometry

Ellipsometry measures the change of polarization upon reflection or transmission. Typically, ellipsometry is done only in the reflection setup. The exact nature of the polarization change is determined by the sample's properties (thickness, complex refractive index or dielectric function tensor). Although optical techniques are inherently diffraction limited, ellipsometry exploits phase information and the polarization state of light, and can achieve angstrom resolution. In its simplest form, the technique is applicable to thin films with thickness less than a nanometer to several micrometers.

The arrangement of the optical components between the source and detector defines the type of ellipsometer (Fig. 2.6). We have used the null ellipsometer. The null ellipsometer operates by adjusting the orientation of the polarizer, compensator, and analyzer so that the light incident on the detector is extinguished or "nulled". The shape of the ellipse depends on the angle of incidence, the direction of the polarization of the incident light, and the reflection properties of the surface.
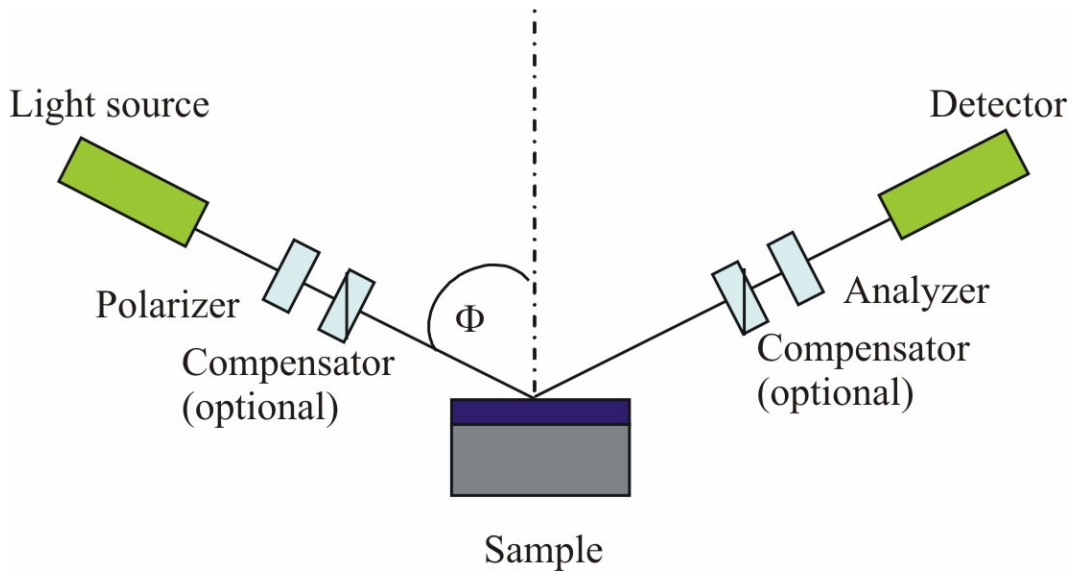
Figure 2.6   Schematic setup of an ellipsometry experiment. Polarize light from the source is reflected from the film surface which is analyzed by the detector.

Ellipsometry does not measure directly the optical constants or film thickness but measures Ψ (the relative phase change) and Δ (the relative amplitude change) which describe the polarization change. These values are related to the ratio of Fresnel reflection coefficients, $\tilde{R}_p$ and $\tilde{R}_s$ for p- and s-polarized (*s* and *p* represent oscillating perpendicular and parallel to the plane of incidence, respectively) light, respectively by the following equation;

$$\frac{\tilde{R}_p}{\tilde{R}_s} = \tan \Psi \exp\left(i\Delta\right) \qquad (1)$$

2.2.3.2   Experimental

Using the null setup as described above, the laser light source (wavelength, λ = 632.8 nm) was inclined with $\Phi = 70°$ with respect to the film normal. Initially, we obtained Ψ and Δ values of bare silicon wafers to enable determined the oxide layer thickness. In the actual measurements, we measure Ψ and Δ values at three

different locations to have a uniform values from the sample surface. Measurements were done at room temperature.

2.2.3.3 Data analysis

To estimate the film thickness, layer models were made using the Elli software. In the layer model, silicon was chosen to be the first layer, followed by silicon oxide, the polymer and the air interface (Fig. 2.7). The thickness of the oxide layer used was 2 nm (measured initially). The refractive indexes of our polymers were $n_{PS-b-PEO}$ = 1.523 for the PS-*b*-PEO and $n_{PI-b-PEO}$ = 1.489 for the PI-*b*-PEO diblock copolymer. The common refractive indexes used for the block copolymer were calculated from the average of the individual refractive indexes (n_{PS} =1.59, n_{PEO} = 1.456 and n_{PI} = 1.521;[37]). In the model, the refractive index for air, n_{AIR} = 1 was used. After fitting, using the layer models with the above values and the obtained experimental Ψ and Δ values, the thicknesses were extracted.

In this type of experiment, the sample surface must be almost flat and must composed of small number of discrete, well-defined layers that are optically homogeneous and isotropic.
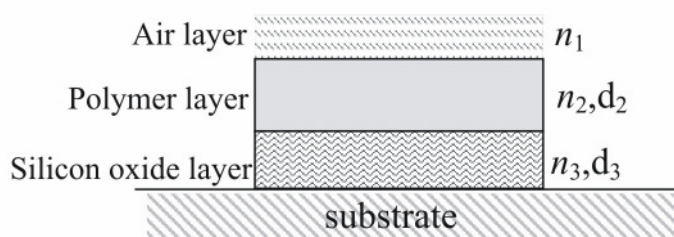

Figure 2.7   Schematic diagram of the layer model in ellipsometry.

2.2.4 Differential scanning calorimetry (DSC)

Differential scanning calorimetry (DSC) is a technique for measuring the energy necessary to establish a nearly zero temperature difference between a substance and an inert reference material, as the two specimens are subjected to identical temperature regimes in an environment heated or cooled at a controlled rate [71]. In our case, the heat-flux DSC was used to measure the thermal transitions of our block copolymer (i.e. changes that occurs in the polymer when you heat it) such as the T_g and T_m.

2.2.4.1   Principles of the heat-flux DSC

In the heat-flux DSC, the sample and reference are connected by a low-resistance heat-flow path (a metal disc). The assembly is enclosed in a single furnace (Fig. 2.8). Enthalpy or heat capacity changes in the sample cause a difference in its temperature relative to the reference. The difference in energy required to maintain the sample and the reference at a nearly identical temperature is provided by the heat changes in the sample. Any excess energy is conducted between the sample and reference through the connecting metallic disc. The thermocouples are not embedded in either of the specimens; the small temperature difference that may develop between the sample and the inert reference (usually an empty sample pan and lid) is proportional to the heat-flow between the two. The fact that the temperature difference is small is important to ensure that both containers are exposed to essentially the same temperature program. A separate thermocouple embedded in the silver block serves a temperature controller for the programmed heating cycle. An inert gas can be passed through the cell at a constant flow-rate. The thermal resistances of the system vary with temperature, but the instrument was used in the calibrated mode, where the amplification is automatically varied with temperature to give a nearly constant calorimetric sensitivity.
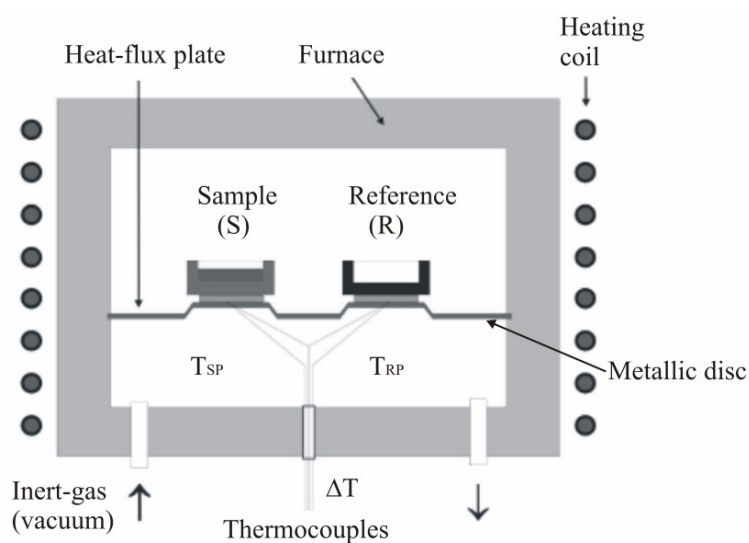
Figure 2.8   Main components of the heat-flux DSC setup.

2.2.4.2   Experimental

The temperature difference is recorded and related to enthalpy change in the sample using calibration experiments. The data was recorded as heat-flow versus temperature which was imported to Origin for analysis. A typical result is as shown in figure 2.9.
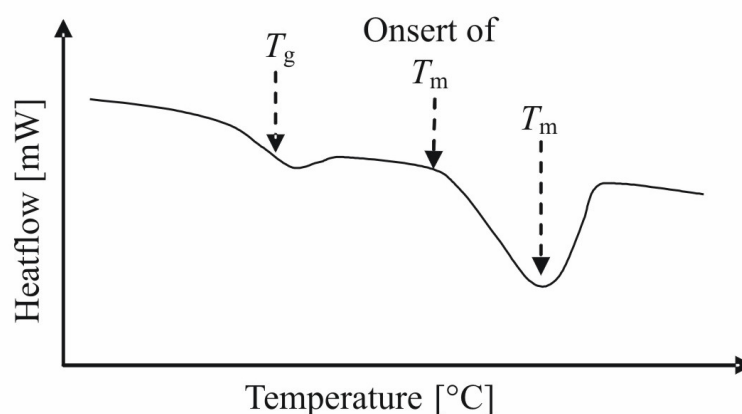
Figure 2.9   Typical DSC curve of a polymer. As the temperature increases, an amorphous polymer will become less viscous. Upon increasing the temperature, the sample eventually reaches its T_m. The melting process results in an endothermic peak in the DSC curve.

2.2.4.3   Data analysis

Data analysis was quite simple. First, a baseline was drawn through the starting line towards the end. To obtain the T_g, the middle point of the change in the baseline as shown in figure 2.9 was used. The exact T_m was taking from the fit of the melting peak (the mid-point) while the onsert of the T_m was taken from the point where the melting peak deviates from the baseline.

2.2.5   Grazing-incidence small-angle X-ray scattering (GISAXS)

Grazing-incidence small-angle X-ray scattering (GISAXS) is a versatile tool for characterizing nanoscale density correlations and/or the shape of nanoscopic objects at surfaces, at buried interfaces, or in thin films [72,73,74,75]. GISAXS combines features from small-angle X-ray Scattering (the mesoscopic length scale, incident beam definition by multiple slits, area detector) and diffuse X-ray reflectivity (the scattering geometry and sample goniometer). We have used the GISAXS to get information on the buried mesophase structure which includes the lamella repeat units and it orientation.

2.2.5.1   Principles of GISAXS

The GISAXS technique is simply probing sample surfaces or thin film surfaces under grazing incidence with a small X-ray beam and collecting the corresponding diffuse scattering on a detector placed at large distances (i.e. 1 - 2 m) from the sample stage. In this way, information on the mesoscopic structures resulting in the diffuse scattering could be obtained.

As shown in figure 2.10, the intense X-ray beam impinges under grazing incidence onto the sample and the scattered intensity is recorded with an area detector [76,77]. One can distinguish between the scattering parallel and

perpendicular to the sample surface, as indicated by the respective components of the scattering vector q_y and q_z. The intensity in the incident plane is determined by the specular and diffuse reflectivity [78,79], with diffuse Bragg sheets extending out into the q_y direction which provide information on the normal density profile of the film. Parallel to the surface small-angle scattering features can appear indicating lateral ordering in the film. The reason for the grazing-incidence geometry is not far from the fact that typical and technically interesting substrates like silicon wafers or glass have thicknesses on the order of 1 mm and would require rather hard x-ray beams for a transmission experiment. Furthermore the weak scattering from a film of typically 20 nm to 200 nm thickness can be obscured by diffuse scattering from the substrate, whereas in grazing-incidence geometry the penetration of the X-ray photons into the substrate is limited, if the angle of incidence is close to the substrate critical angle.
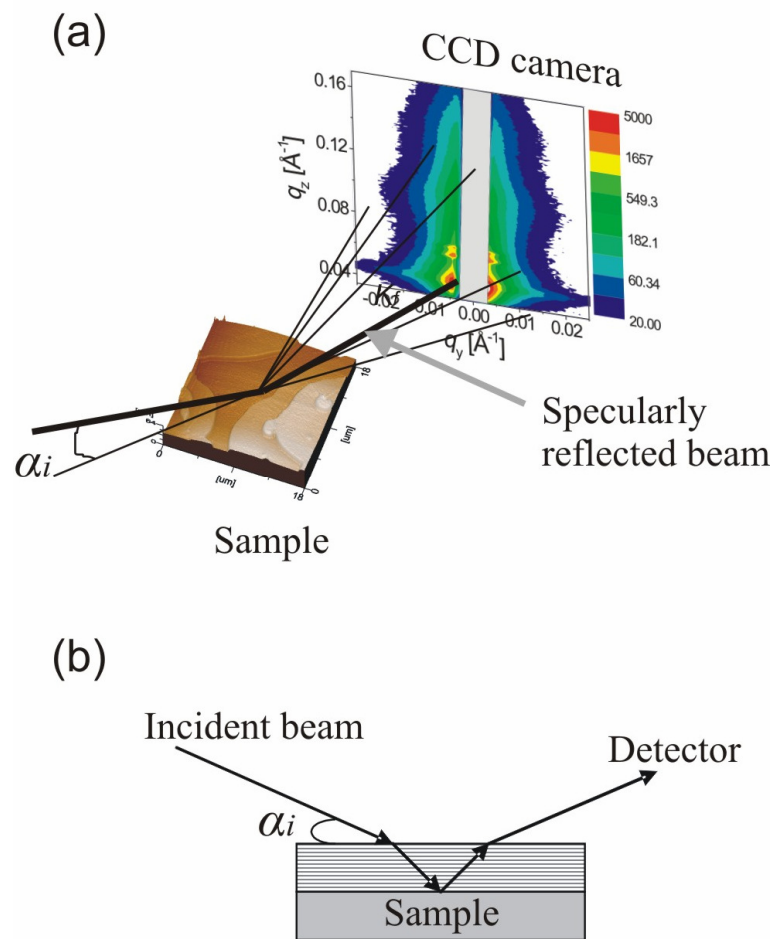
Figure 2.10 GISAXS scattering geometry. (*a*) Show the direction of the beam on the sample under incident angle, α_i, and the corresponding image obtained on the detector. (*b*) Show the scattering process at the surface where there is refraction from the sample surface, reflection from the silicon and the refraction from the polymer/air interface. The system is such a way that $\alpha_{cp} < \alpha_i < \alpha_{cs}$, where α_{cp} and α_{cs} are the critical angle of the polymer and the silicon, respectively.

2.2.5.2 Experimental

GISAXS experiments were performed at both beamline BW4, HASYLAB [80] and beamline D1, CHESS [81] to obtain structural information within the thin film at mesoscopic length scales. At both beamlines, using evacuated pathways to define the resolution and to reduce the background by parasitic scattering, sample

to detector distances were selected between 1.08 m and 2 m. Exposure times were controlled by a fast shutter in the incident beam.

At BW4 beamline, a monochromatic beam having wavelength, $\lambda = 0.138$ nm together with a high resolution 2-dimensional (2D) CCD detector (MAR research, 2048×2048 pixel, pixel size 79 µm) were used. The beam size was focused by beryllium lens system [82] to a size of only 46 µm (vertical) $\times$ 78 µm (horizontal) at the sample position which limited the footprint to 13 mm at an incident angle of $0.2°$. After carefully aligning the X-ray beam on the sample surface (i.e. by correcting the incident and the reflected angle at different positions with several tilt angles), the sample was placed to cut half of the small beam. This was to ensure that the beam perfectly sit on the sample surface. Finally, the position of the specular peak on the detector was check to verify the precise movement of the motors during measurements.

At D1 beamline, a monochromatic beam having $\lambda = 0.124$ nm together with a high resolution 2D CCD detector (MedOptics, 1024×1024 pixel, pixel size 47.19 µm) were used. The beam size was around 1 mm (vertical) $\times$ 1 mm (horizontal). Alignment was done with the help of an ion chamber placed in front of the CCD camera. The chamber measured the intensity profile by increasing the tilt angle of the sample. With this, the onset of the intensity representing $\alpha_i = 0°$ could be obtained (Fig. 2.11). Using this setup, fine reflectivity curves could be obtained as well.
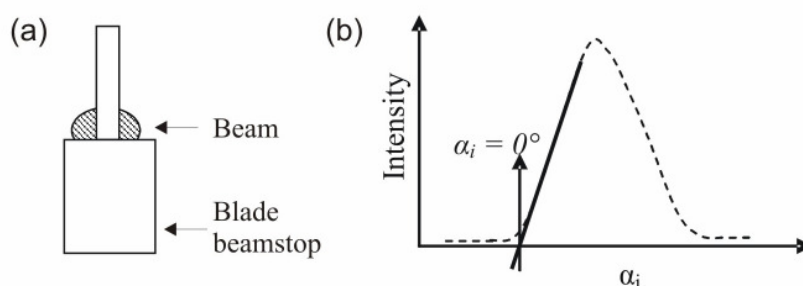

Figure 2.11 Sketch of beam alignment at D1 beamline (CHESS) showing (*a*) the blade beamstop placed in front of the ion chamber to block the direct X-ray beam and (*b*) the resulting intensity curve obtained by varying the sample tilt angle. In (*b*), the zero point representing the cut-of of the blade could be measured.

In all the measurement, the incident angle, α_i, was varied between 0.15 and 0.5°, thus above the critical angle of the polymer film ($\alpha_{cp} = 0.13°$ for $\lambda = 0.124$ nm and 0.14° for $\lambda = 0.138$ nm). Measurements were carried out at room temperature. A molybdenum rod with diameter of 1.5 mm served as beamstop to protect the detector from the specular peak and the strong diffuse scattering in the plane of incidence. In order to minimize radiation damage, the samples were moved sideways after alignment, so that a pristine sample spot was exposed to the beam during the measurements. GISAXS measurements were recorded with exposure times of 3 to 30 s at D1-beamline and about 10 to 30 minutes at BW4 beamline and both were corrected for background from dark and read-out noise. The 2D maps in pixels were transformed into reciprocal q-space values by a calibration factor depending on the scattering geometry.

At the D1 beamline and using a GISAXS sample chamber described in Ref. 83 with a cooling and heating rate of ± 6°C/s, we performed isothermal measurements from 25°C to 55°C in steps of 5°C and measurements were taken 5 minutes after reaching a particular temperature to allow for equilibration whiles moving the sample laterally to fresh spots to avoid beam-damage.

2.2.5.3   Analysis of GISAXS data

Analysis of GISAXS are handled within the framework of the distorted wave Born approximation (DWBA) [84,85,86,87]. In our work, a model based on the GISAXS scattering cross section in the context of DWBA for two cases of parallel and perpendicular orientation of lamellae formed in thin supported mesoscopically structured polymer films was used [88]. The scattering potential describing the lamellar film was assumed to be the sum of the potential of a homogeneous film with planar interfaces and a perturbation potential describing the lamellar structure in the film, including a simple model for the surface roughness for the parallel case. In addition to the scattering by the inner film structure, both the refraction at the film surface and the reflection of the incident or the scattered beam at the substrate surface are taken into account.

For two-dimensional GISAXS maps of laterally ordered films (Fig. 2.12*a*), interference peaks (Bragg rods) are expected at parallel momentum transfers being a multiple of $2\pi/L$ (where L is the lamellar thickness) and with a q_z-profile mainly being a function of film thickness.

(a) perpendicular   **(b) parallel**

$2\pi/D_{lam}$ q_z q_z

q_y q_y

Interference   Spekularly   Diffuse Bragg
peaks   reflected beam   sheets
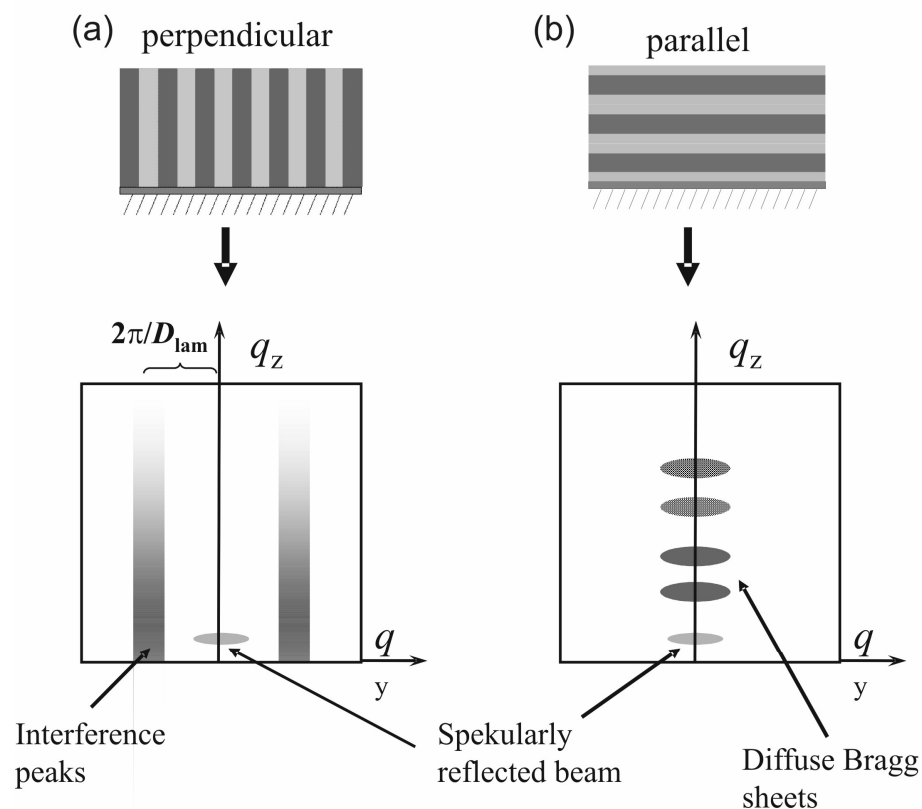
Figure 2.12 Schematic drawings of the scattering from perpendicular (*a*) and parallel (*b*) lamellae promoting interference peaks and diffuse Bragg sheets, respectively.

A lamellar diblock copolymer film with the lamellae *parallel* to the substrate surface can be viewed as a multilayer system of alternating PS and PEO layers. Flat lamellae give rise to interference peaks at distinct positions along the q_z-axis in the plane of incidence, i.e., for $q_y = 0$ (Fig. 2.12*b*). Correlated roughness of the layers with a wavelength smaller than the lateral coherence length leads to widening of the peaks along q_y, leading to the so-called diffuse Bragg sheets,

which can be observed close to the rodlike beamstop [89]. The q_z-positions of the lamellar diffraction peaks appearing in addition to the specularly reflected beam and the Yoneda peaks of the polymer film and the substrate are given by [102];

$$q_z = \frac{2\pi}{\lambda} \left\{ \sin\alpha_i + \sqrt{\sin^2\alpha_{cp} + \left[\frac{m\lambda}{L} \pm \sqrt{\sin^2\alpha_i - \sin^2\alpha_{cp}}\right]^2} \right\} \qquad (2)$$

where m denotes the order of reflection (i.e. positive odd integer). Equation 2 can be re-written such that peak positions, q_z, of the diffuse Bragg sheets depends on L, and on the vertical component of the incident wave vector, $k_{iz} = 2\pi\sin(\alpha_i)/\lambda$ by;

$$q_z = k_{iz} + \sqrt{k_{cp}^2 + \left[m\frac{2\pi}{L} \pm \sqrt{k_{iz}^2 - k_{cp}^2}\right]^2} \qquad (3)$$

where $k_{cp} = 2\pi\sin(\alpha_{cp})/\lambda$. Note that for Eq. 1 and 2, the refraction of the incoming and outgoing X-ray beams at the air-film interface was properly accounted for. The two branches of this curve for each m correspond to the Bragg diffraction of the reflected beam (upper branch) and the direct diffraction process, which merges, at α_{cp}, with the process where the diffracted beam is reflected from the substrate (lower branch) (see ref 102 and figure 2.13). We have obtained intensity profiles along q_z from our 2D maps by integrating over the region $q_y = -0.009$ to $+0.009$ Å^{-1}.
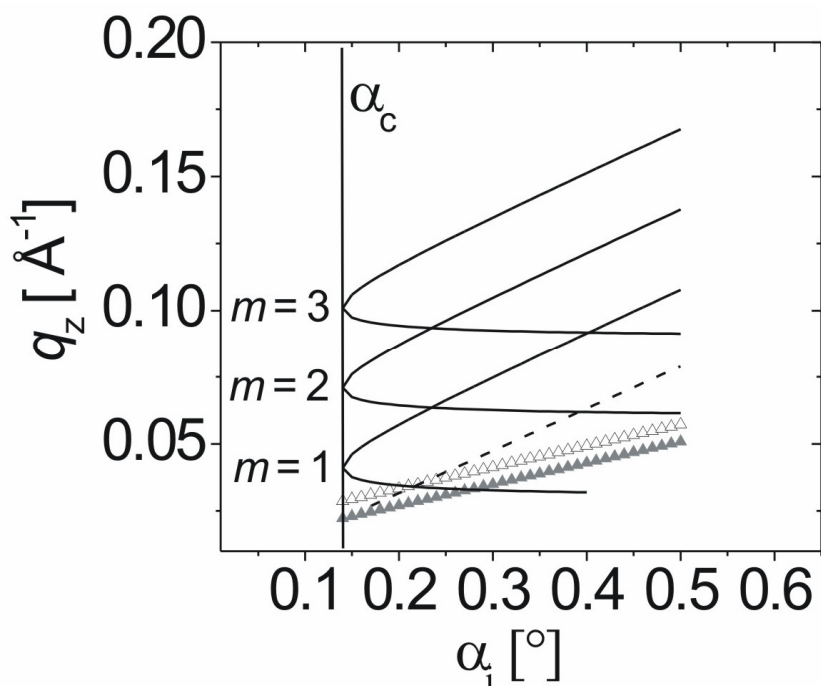
Figure 2.13 DWBA model curves (—) in the α_i–q_z plane as predicted by equation (1) for films $L = 21$ nm, $\lambda = 0.138$ nm and $\alpha_{cp} = 0.14°$. Shown are the lowest three model curves with $m = 1$, 2 and 3 together with the positions expected for the specular peak (dashed line), substrate (Δ) and polymer ($\blacktriangle$) Yoneda's.

2.2.6 Grazing-incidence wide-angle X-ray scattering (GIWAXS)

Grazing-incidence wide-angle X-ray Scattering (GIWAXS) gives information on the crystalline structure and its orientation within thin films [90]. It uses the same scattering geometry and principle as GISAXS but in this case, rather much higher q-vaules are probed with shorter sample to detector distance (i.e. ~ 15 cm) than GISAXS.

2.2.6.1 Experimental

GIWAXS experiments were performed at Risø National Laboratory, Roskilde, Denmark. A Rigaku rotating anode X-ray source with $\lambda_{Cu,k\alpha} = 0.1542$ nm was used

together with a Fuji film image plate detection system with a pixel size of 50 μm × 50 μm. The scattering geometry illustrated in figure 2.14 with a sample-detector distance of 124 mm was used. α_i = 0.18° was used for all samples. More description on the actual scattering geometry at Risø can be found in Ref. [91]. Measurements were performed at room temperature under vacuum.

Top view
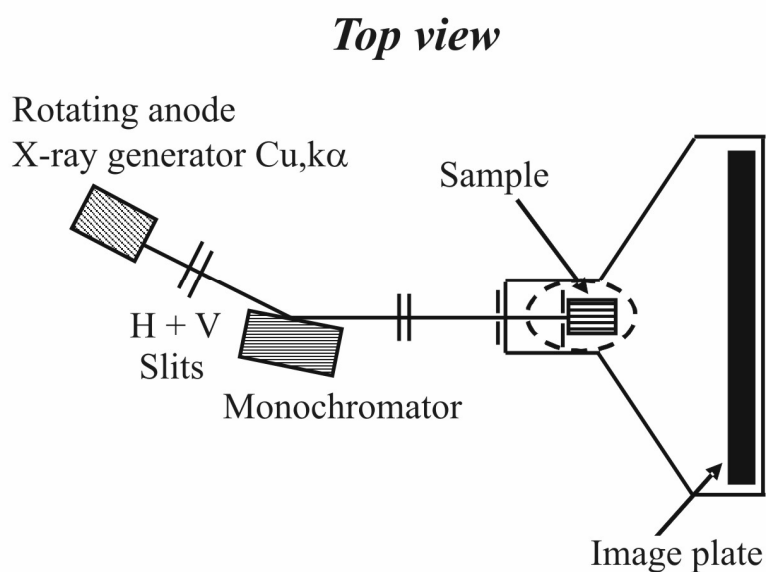
Figure 2.14 Grazing-incidence wide-angle X-ray scattering setup.

The image plate was mounted on a standard Risø goniometer, which allows translation, rotation and tilting, making it possible to accurately align samples in the grazing incidence reflection geometry. Air scattering is eliminated by evacuating the entire camera, which at the same time reduces the risk of inducing beam-damage on the sample. The measured information on the image plate was digitized and fed into computer as a 2D image for processing. The images were interpolated to reciprocal space units (q_{xy}, q_z). A region near the q_z axis in reciprocal space was not available when using a fixed incidence angle.

To determine the correct peak widths of the reflections obtained in the 2D GIWAXS data in order to estimate the crystalline domain sizes and the degree of

crystallinity, high resolution reciprocal intensity profiles were measured using synchrotron. The experiments were performed using the z-axis diffractometer at the wiggler beamline BW2 at HASYLAB at DESY, Hamburg [92,93,94]. λ = 1.24 Å and α_i was fixed at 0.16°. A scintillation point detector was used and the parallel incoming beam of 1mm (horizontal) × 0.1mm (vertical) was adopted. In the setup shown in figure 2.15, slits of 1×1 mm^2 was placed in front of the flight tube which was some few centimetres from the sample stage. In front of the detector, ~1.2 m from the sample, detector slits of 4 x 4 mm^2. The detector could be set to an in-plane (horizontal) and exit (away from the horizontal) angles with respect to the surface. The sample was mounted horizontally in a chamber which was made from kapton foil and which was flushed with He gas to reduce air scattering. Measurements were carried out at room temperature.

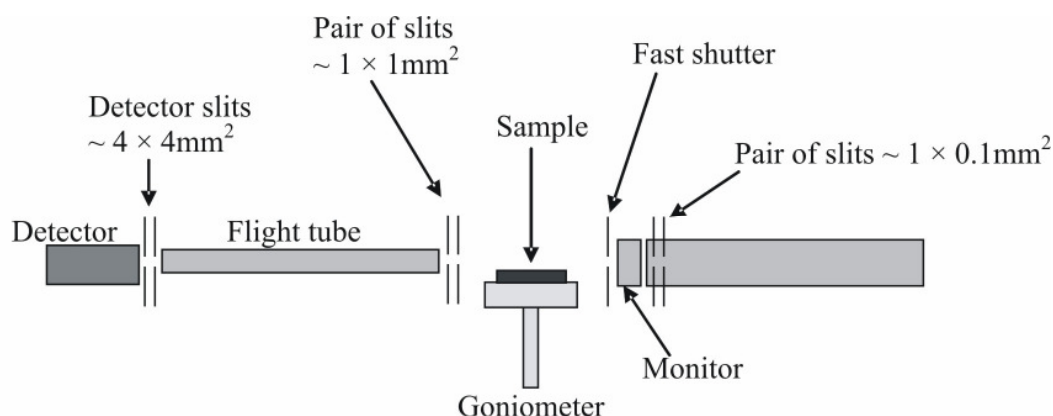**Figure 2.15** Side view schematic diagram of the BW2 beamline setup used for the high resolution X-ray diffraction experiments.

2.2.6.2   Analysis of GIWAXS Data

Simulations

The GIWAXS data were analysed (including indexing) by comparing them to results from simulations using the SimDiffraction software code [95,96,97]. It incorporates the unit cell, including atomic positions, and the geometrical Lorentz

and polarization corrections, and is specifically designed to model samples with preferred orientation as well as variations from this orientation.

The PEO block crystallizes in a monoclinic crystalline lattice defined by the following parameters: a = 8.05 Å, b = 13.04 Å, c = 19.48 Å and β = 125.4° [98]. The conformation of PEO is a (7/2) helix which means that seven monomeric units turn two times per fiber period as shown in figure 2.14. The space group is assigned to be $P2_1/a$-C_{2h}^5 based on the systematic absences of the $h0l$ at h = odd and $0k0$ at k = odd. There are four helical molecules within one unit cell with the c-axis nearly perpendicular to the base. The helix conformation (Fig. 2.16b) is distorted from a D7 point group (Fig. 2.16c) due to the flexibility of the PEO molecular chain and the intermolecular interactions in the crystals. The helical chain conformation is close to a gauche-trans-trans sequence of bond rotations, with the gauche conformation between the two methyl (CH2) groups.
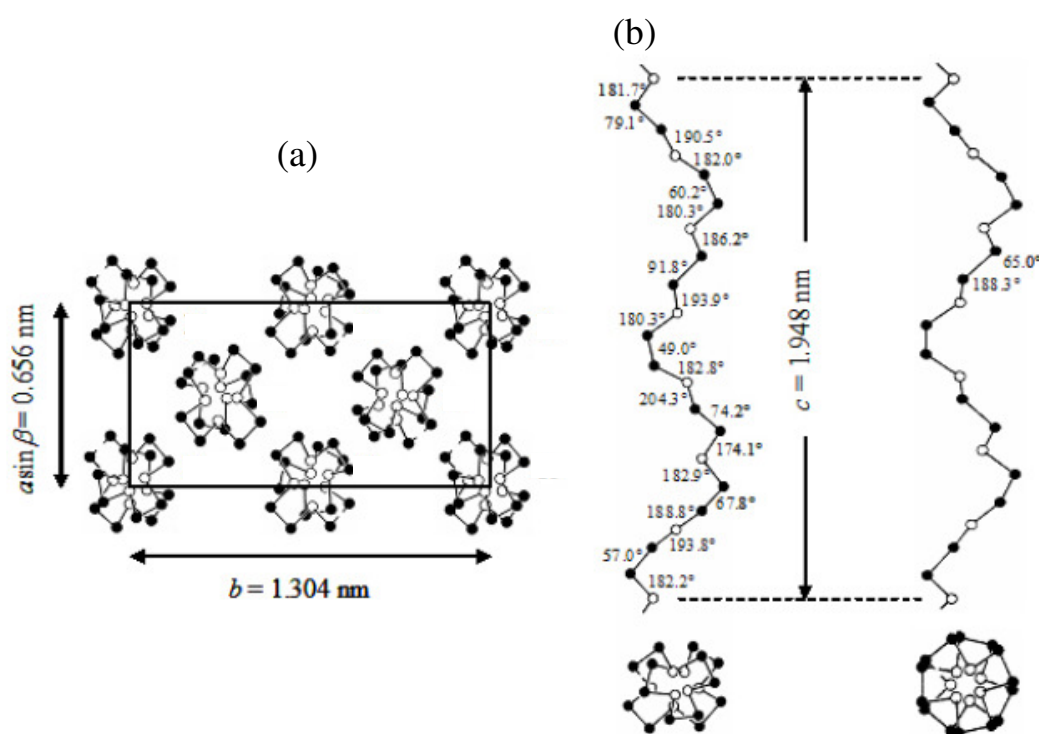

Figure 2.16. Unit cell of monoclinic PEO in the c-axis projection (*a*), molecular model of PEO with the molecular structure (*b*) and with the helical symmetry D7 (*c*). The figures give the internal rotation angles. Adopted from ref 96. The open and black circles represent oxygen and carbon atoms, respectively. The hydrogen, H, atom has been included.

The above PEO crystal structure parameters together with the settings of the actual scattering geometry, such as α_i, the λ and the sample to detector distance were used in the simulations which is Matlab based.

In the classical uniaxial distribution models (e.g. Kratky model, Ref. 99), the director of a crystallite (in polymers often the chain axis, *c*-axis) orients at an angle χ with respect to the sample normal, with an orientational distribution function (ODF), f(χ). On average, all crystallites orienting with a certain χ assume all possible rotation angles about the director. Note that this model assumes no in-plane orientation of the crystallites, often referred to as "2D powder" or cylindrical symmetry. Thus, in the simulations, the *c*-axis orientation ("director") of the PEO crystal unit cell with respect to the film normal was varied systematically according to an ODF with a given width, and the crystallites were rotated about the director while maintaining in-plane isotropy, cf. Breiby (2007) for further details. The "rods in soft matrix" model of Kratky was found to describe the observed scattering well for the samples with a low degree of preferred orientation. In the Kratky model, the crystallites are considered stiff rods in an affine matrix, and when the matrix is stretched by an elongation ratio λ_K, the rods obtain an ODF

$$f(\chi) = \frac{1}{4\pi} \frac{\lambda_K^3}{\left[\lambda_K^3 - \left(\lambda_K^3 - 1 \right) \cos^2 \chi \right]^{3/2}}\tag{4}$$

Hence, we could obtain simulated diffraction pattern for specific crystalline orientation as well as for crystallites having wide orientational distribution.

2D GIWAXS pattern interpretation

In figure 2.17, simulated 2D diffraction pattern with PEO *c*-axis uniaxially oriented perpendicular, inclined and parallel to the film/substrate interface were

obtained. In general, the strongest reflections found in PEO 2D diffraction patterns are the *120* and the *032*.

For *perpendicular* c-axis orientation with respect to the film substrate (Fig. 2.17*a*), the *120* reflections were found at the in-plane direction (i.e. at $q_{xy} = \pm$ 1.356 $\mathring{A}^{-1}$) while the *032* were found at the out-of-plane (i.e. at an angle of 23° to the in-plane, with $q_{xy-z} = 1.645$ $\mathring{A}^{-1}$).

When the *c*-axis is *inclined* with respect to the film substrate (Fig. 2.17*b*), the simulation pattern showed the *120* reflections were shifted into the out-of-plane (i.e. at an angle of 45° to the in-plane) while the *032* were shifted more to the out-of-plane (i.e. at an angle of 28° to the in-plane, with $q_{xy-z} = 1.645$ $\mathring{A}^{-1}$)

For *parallel* c-axis orientation with respect to the film substrate (Fig. 2.17*c*), simulations showed that the *120* and *032* reflections were absent. Meaning, in this preferred orientation, the *120* and *032* reflections was found in the negative direction of the q_z.

The significant changes in the positions of these reflections give strong indication of the PEO *c*-axis preferred orientations.
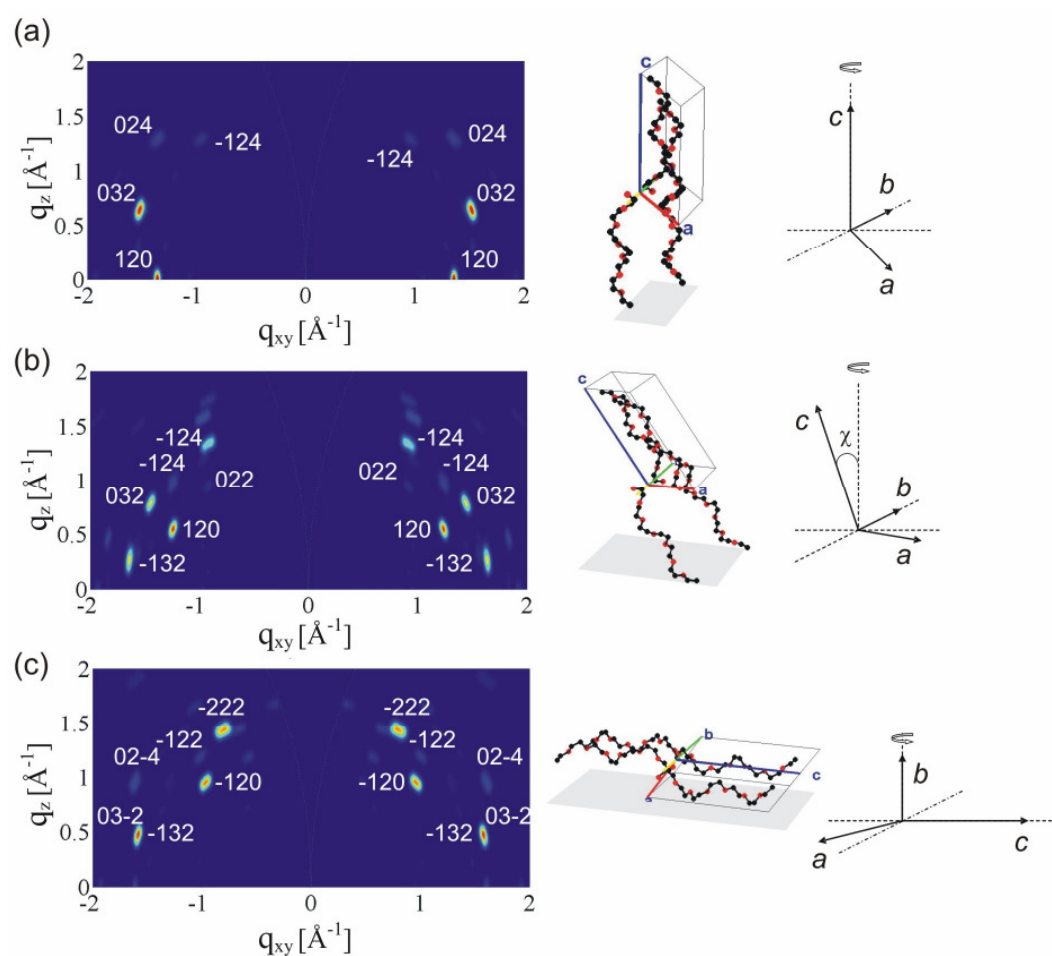
Figure 2.17. Simulated diffraction patterns for PEO crystals with *c*-axis perpendicular (*a*), inclined at an angle χ = 35° (*b*) and parallel (*c*) with respect to the substrate interface. In the unit cell, the red and black dots depict oxygen and carbon atoms, respectively. Hydrogen atoms were ignored since they do not influence the scattering spectra.

Effect of orientational distribution

When the crystalline chains have wide orientational distribution, it creates angular distributions on the simulated 2D pattern. In figure 2.18, such a diffraction pattern was obtained with *c*-axis perpendicular with respect to the film substrate but with orientational distribution width (fwhm), Δθ = 20°. It means that, the crystallite have perpendicular mean orientation with few crystallites deviating from this

38

mean orientation by 10°. Such orientation distribution was described by the Kratky model.
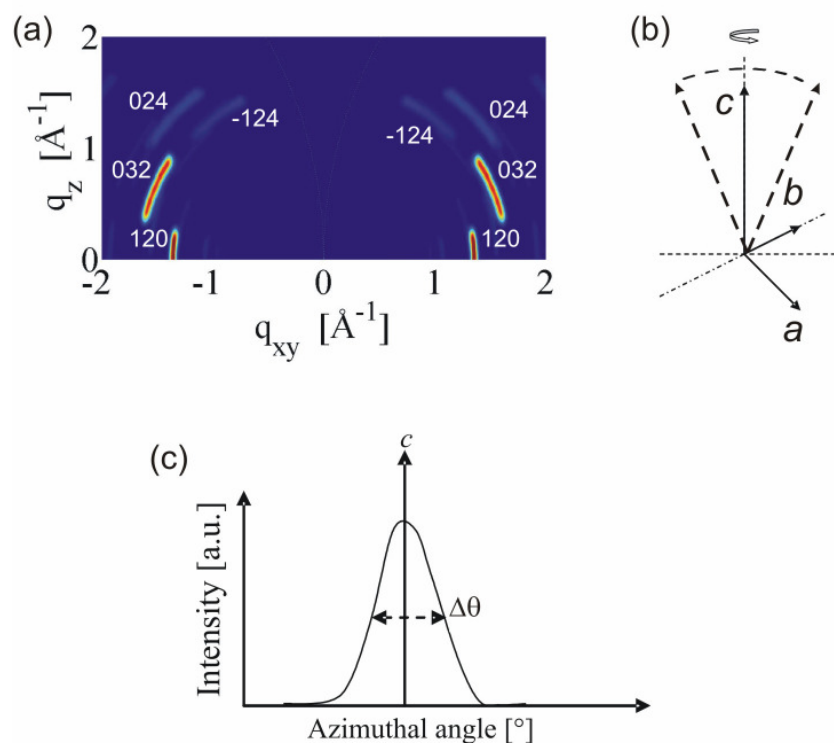
Figure 2.18. Simulated diffraction patterns for PEO crystals with *c*-axis perpendicular having orientational distribution width (fwhm), $\Delta\theta = 20°$ (*a*). (*b*) and (*c*) are schematic diagrams of the *c*-axis orientation and the orientation distribution function, respectively.

High resolution GIWAXS intensity profile interpretation

Using the high resolution synchrotron data which show the intensity profiles for the reflections along the in-plane direction, for example SSEO25 film, we could estimate crystalline sub-domain units and the degree of crystallinity (Fig. 2.19).
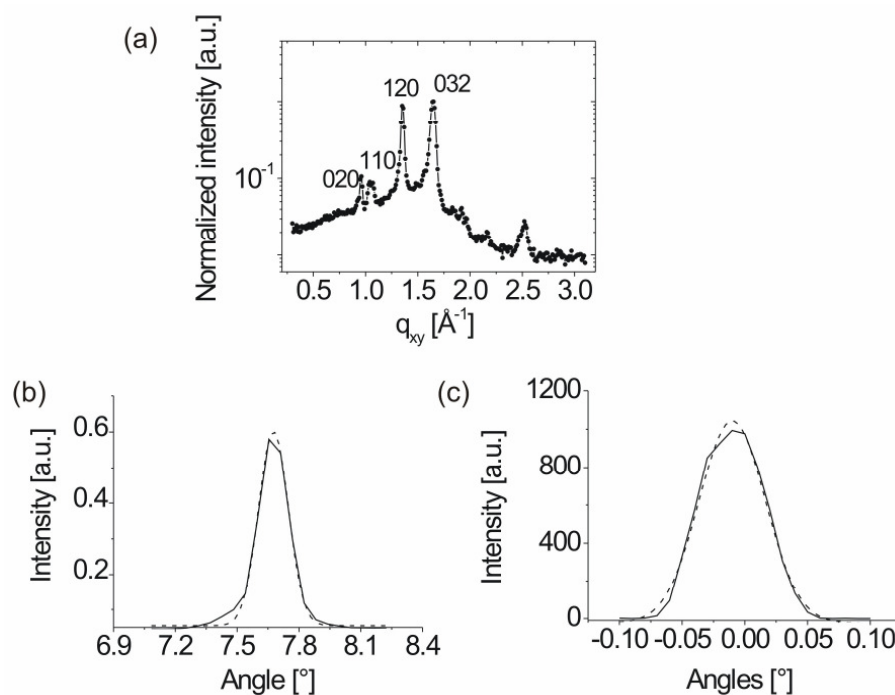
Figure 2.19. (*a*) Synchrotron diffraction intensity profile (●) measured along the film in-plane for SSEO25 film (the line is a guide to the eye). (*b*) And (*c*) are plots of the *120* peak extracted from (*a*) and the direct beam, respectively in degrees. Lines show measured data while dash lines show Gaussians fittings. Full width at half maximum's (FWHM's) were 0.14489° and 0.066° for the *120* peak and the direct beam, respectively were obtained.

From figure 2.19*a*, the degree of crystallinity was estimated by comparing (or dividing) the area of the crystalline peaks and (by) the amorphous halo. To estimate the crystalline domain thickness, the FWHM of the direct beam was subtracted from the *120* FWHM (i.e. 0.14489 – 0.066 = 0.07889°). Using the Scherrer's formula, the crystalline domain sizes (D_{hkl}) were obtained to be ~ 81 nm (see appendix B)[100]:

2.2.7 X-ray reflectivity (XR)

XR is a technique for investigating the near-surface structure of many materials [101]. It probes the electron density with a depth resolution of less than one nm for depths of up to several hundred nm. The method involves measuring the reflected X-ray intensity as a function of X-ray incidence angle (typically, small angles are used). The method is used for studies of thin films and multilayers of metals, semiconductors and polymers. It can accurately determine films thickness, density, average roughness, and the roughness correlation function. We have used the XR to determine the film thickness, the number of lamellae layers as well as the surface roughness of our polymer thin films.

2.2.7.1 Principles of XR

A typical specular reflectivity setup is as shown in figure 2.20. The incident X-rays impinge on the sample at a small angle α and the intensity of the specularly reflected X-rays is detected at an angle α from the surface; the scattering angle is 2α and the scattering vector is normal to the surface. Data are collected as function of α or equivalently $q = (4\pi/\lambda) \sin\alpha$.
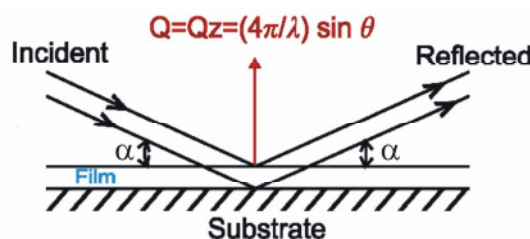

Figure 2.20. Setup of specular reflectivity

2.2.7.2   Experimental

Reflectivity curves were obtained using the X-ray diffractometer Siemens D5000. Cu,Kα source with λ = 1.54 Å was used. The beam was collimated by a knife-edge collimator and a slit system resulting in a width of ~12 nm. A scintillation counter detector was used with a resolution of 0.0014°.

2.2.7.3   Data analysis

The data were analyzed by comparing them with reflectivity curves from a multilayer model which incorporates several variable parameters (e.g. film thickness, density and roughness). The model curves were generated using the Paratt32 software. As depicted in figure 2.20a, our block copolymer films were modelled by parallel packing of multiple layers. The respective real (ρ_s) and imaginary (imρ_s) scattering length densities as well as initial layer thicknesses (d) and numbers were used and were varied until a very good fit was obtained.

In the modelling, ρ_s = 2.015 × 10^{-5} Å^{-2} and imρ_s = 4.588 × 10^{-7} Å^{-2} were used for silicon while ρ_s = 1.891 × 10^{-5} Å^{-2} and imρ_s = 2.445 × 10^{-7} Å^{-2} were used for silicon oxide [102]. For PS block, ρ_s = 9.6 × 10^{-6} Å^{-2} and imρ_s = 1.23 × 10^{-8} Å^{-2} while for PEO block, ρ_s = 1.14 × 10^{-5} Å^{-2} and imρ_s = 2.37 × 10^{-8} Å^{-2}. Also, for PI block, ρ_s = 6.46 × 10^{-6} Å^{-2} and imρ_s = 7.63 × 10^{-9} Å^{-2}.

The resulting model curves were plotted on top of the experimental reflectivity curves to visualize the fitting as depicted in figure (Fig. 2.20b).
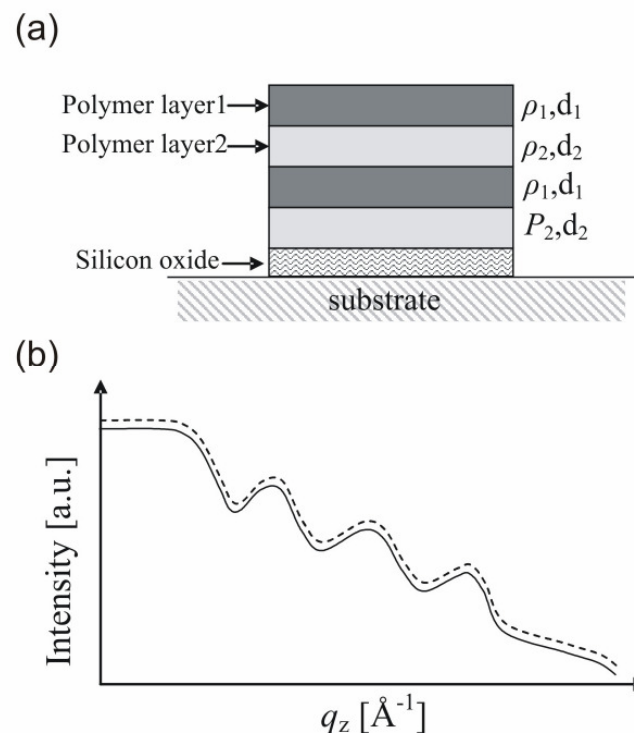
Figure 2.20. Typical schematic diagram showing XR curve modelling. (*a*) Multiple layer model and (*b*) typical reflectivity curve from a good fit (full and dash lines represent supposed experimental and model reflectivity curve)

Chapter 3

Unconfined crystallization

3.1   Aim of work

The aim is to learn about the dependence of crystalline and mesoscopic structures on crystallization kinetics.

In polymer crystallization single chains orient parallel to each other and form two-dimensional lamellae which may be macroscopically large with the chains usually perpendicular to the surface of the lamellae [31]. It involves both, the diffusion of amorphous chains towards the growth front and their folding into regular structures. Recently, more complex processes have been discussed to take place at the growth front, such as the formation of small crystalline domains which finally form the lamella [103,104]. Based on phase-field simulations, the loss of rotational freedom of the chains was proposed as a possible reason [104].

Recently, the existence of a substructure within crystalline polymer lamellae has been discussed [103,105]. The granular substructure has been observed in direct space observations by atomic force microscopy (AFM). However, it is still unclear if an orientation correlation exists between chain stems of different grains. This cannot be revealed in bulk studies either.

In order to allow for an unambiguous identification of the chain orientation and its distribution with respect to the lamellar surface, all lamellae have to be aligned in a unique direction. This has previously been achieved by shear-alignment of bulk block copolymer samples [23,39,106]. Another possibility is provided by the thin film geometry where lamellar structures usually align along the substrate surface, because the two blocks have different surface tensions and different interface

tensions with respect to the substrate material [45,46,107]. In this way, it becomes possible to correlate a possible domain structure to the distribution of chain orientations.

We present here a study on the structures resulting from crystallization of symmetric PS-*b*-PEO diblock copolymers in thin flm geometry. Using block copolymers has the advantage that, upon crystallization, the PEO lamellae microphase-separates from the PS layer, which leads to the creation of lamellae in the film. In this way, the two-dimensional crystal growth could be investigated in a film consisting of several stacked crystallites. We combined real and reciprocal space techniques to determine the orientation of the crystalline PEO blocks within the films. We covered the whole range of length scales from the macroscopic down to the atomistic level. Both surface images and buried structures could be resolved. Moreover, we employed unconfined crystallization which allowed us to distinguish between integer and non-integer folded states, representing alternative ways to accommodate polymer crystals within the pre-set restricted geometry of block copolymer mesophases.

Observations were made on three thin films crystallized at three different temperatures; 25 (strong supercooling), 40 (intermediate supercooling) and 50°C (low supercooling). These films were termed 'crystallized at $T_x = 25$°C, 40°C and 50°C', respectively, for simplicity.

3.2   Results and discussions

3.2.1 Surface analysis

Varying the degree of supercooling has a strong influence on the crystalline growth rate (Fig. 3.1), as known from the literature [108,109]. The growth rate in thin films of PS-*b*-PEO at $T_x = 25$ and 40°C was similar (i.e. 5.4 and 5.5 µm/s, respectively), whereas it was a factor of about 3×10^3 lower at $T_x = 50$°C. In view of this finding, the structure of three samples was studied. At $T_x = 25$°C, the film crystallized completely within 1 min (Fig. 3.2*a* and *b*). In contrast, at $T_x = 50$°C,

the crystals grew much more slowly (Fig. 3.2*c* and *d*). After 30 min at 50°C, the crystalline domain growth front had only moved a little closer to the reference point marked by the arrow in figure 3.2*c*. At this temperature, it took several days to complete the crystallization process of a film of size 2 cm × 2 cm.
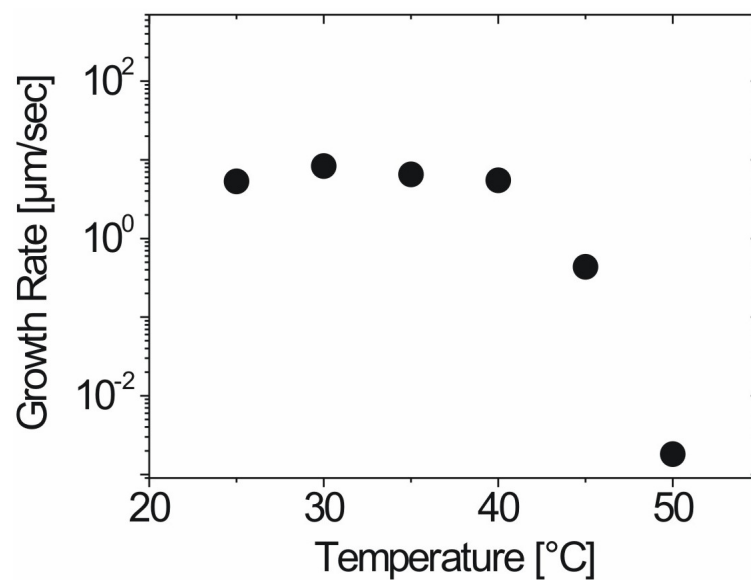

Figure 3.1. Crystalline growth rate as a function of crystallization temperature for the investigated P(S-*b*-PEO) thin films.
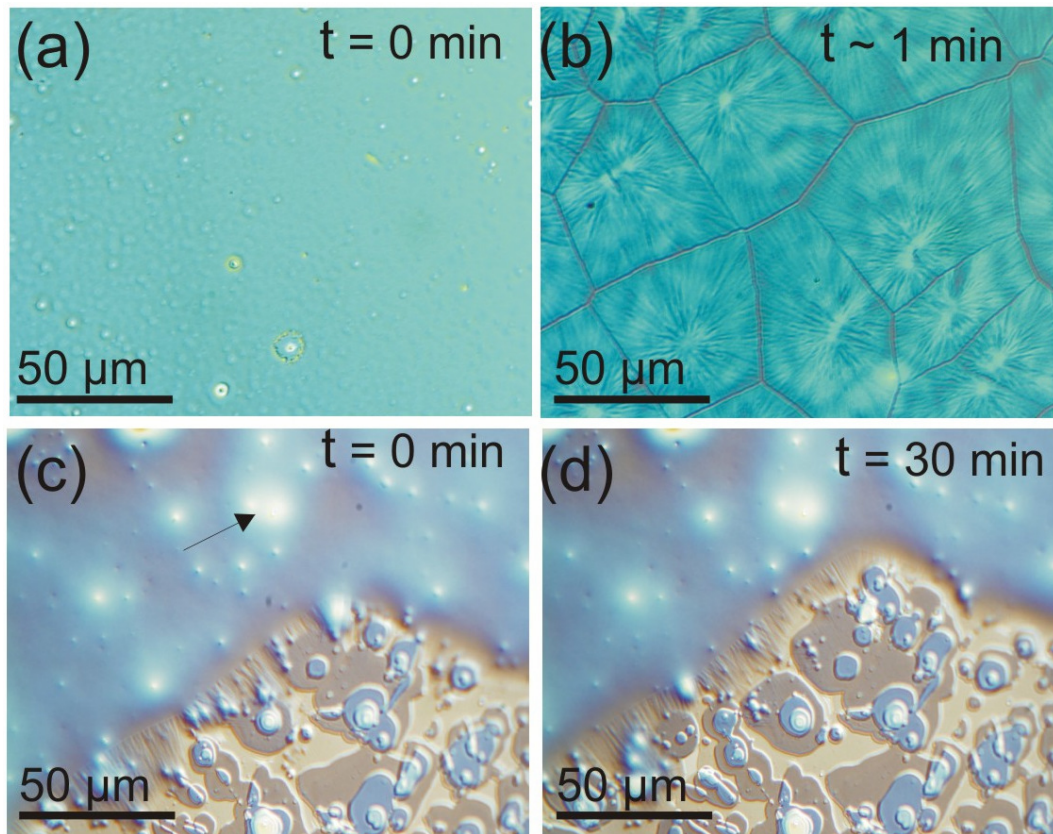
Figure 3.2. Optical micrographs of P(S-*b*-EO) thin films crystallized at (*a,b*) $T_x =$ 25°C and (*c,d*) at $T_x = 50$°C, showing the evolution of the surface morphology with time. The black arrow in (*c*) shows a reference point. The different colours are due to differences in height scale (blue means higher height, brown means lower height) and differences in reflectivity indexes.

The resulting surface morphologies obtained at the three studied crystallization temperatures were distinctly different (Fig. 3.3). At $T_x = 25$°C (Fig. 3.3*a*), a number of nuclei were formed from which they grew outward until they met (i.e. growth of spherulites). A similar surface texture was obtained at $T_x = 40$°C (Fig. 3.3*b*), however, since the density of nuclei was lower than at 25°C, the crystalline domains became relatively large before meeting each other. The boundaries between crystalline domains were always straight. At $T_x = 50$°C, however, the surface texture looked completely different (Fig. 3.3*c*): Staggered terraces were observed at the film surface. The image shown was taken from a single crystalline domain. Not only very few nuclei were formed but also, the growth rate was slowvat $T_x = 50$°C.

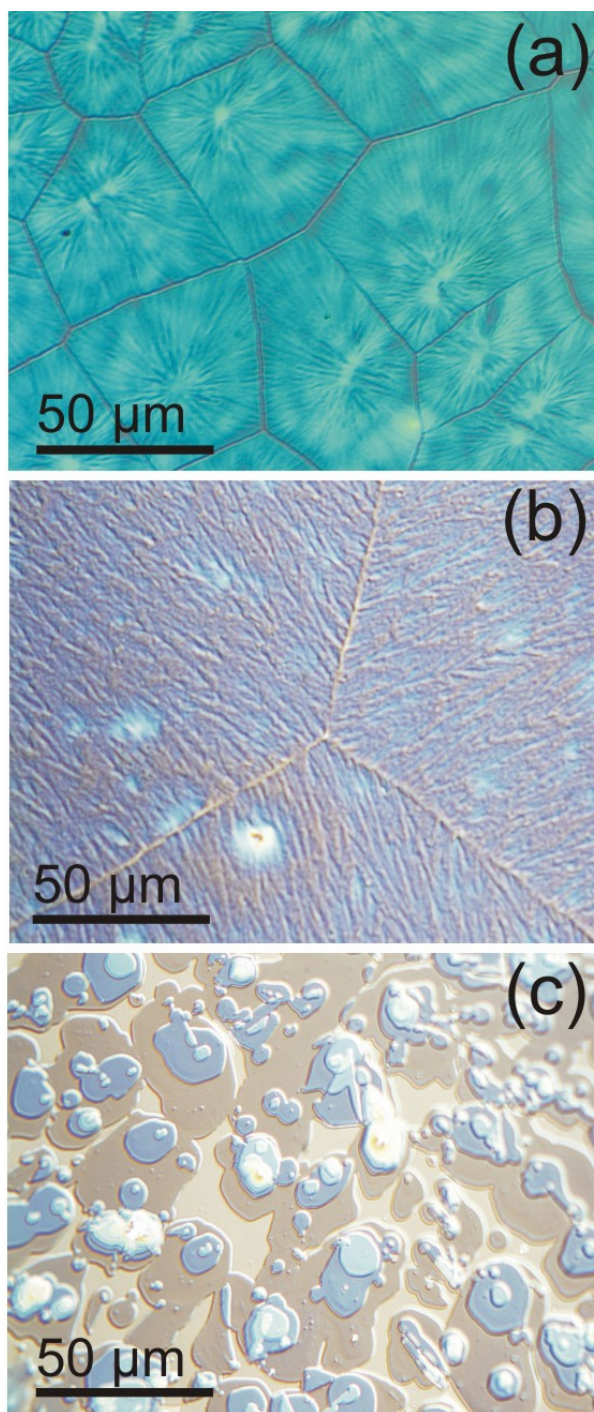**Figure 3.3**. Surface morphologies obtained using optical microscopy at room temperature after complete crystallization at $T_x = 25°C$ (*a*), $T_x = 40°C$ (*b*) and $T_x = 50°C$ (*c*).

Detailed studies of the local surface structures obtained from AFM show that after crystallization at T_x = 25 and 40°C (Fig. 3.4a and b), the surfaces were textured only at small length-scales. Nearly identical granular elongated structures were observed and were assigned to individual PEO crystallites which formed at the advancing growth front. Granular size of ~100 was obtained. The rms surface roughness of these films were 2.3 nm and 1.9 nm for T_x = 25 and 40°C, respectively. For the film crystallized at T_x = 50°C (Fig. 3.4c), the AFM topography image gave a clear magnification of the terraced morphology observed using OM (Fig. 3.3c). The terraces were too large to be contained within the scope of the maximal AFM scan size. From the image shown, the terrace heights were found to be 11.0 ± 0.5 nm (Fig. 3.4d).
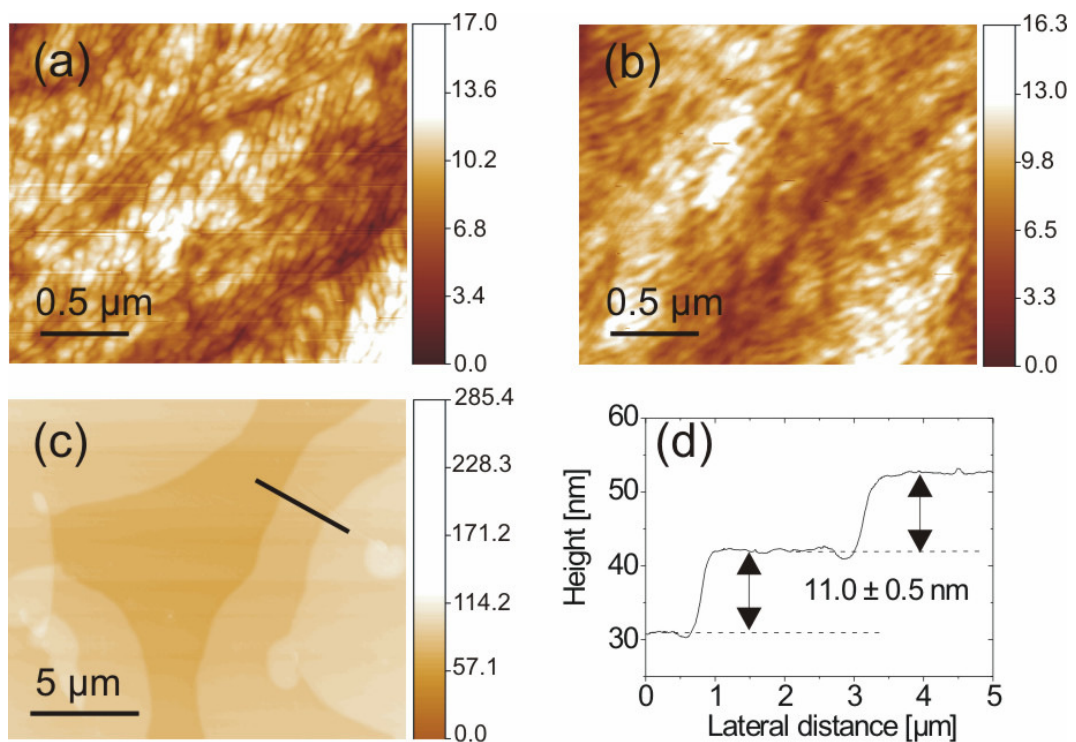
Figure 3.4. AFM topography images of films crystallized at T_x = 25°C (a), T_x = 40°C (b) and T_x = 50°C (c) measured at room temperature. (d) Represents the line cross-section indicated in (c). On (a) and (b), surface granular sizes of ~ 100 nm were obtained by line surface size analysis.

To summarize the microscopy observations, the degree of supercooling has a large effect on the surface texture of the thin films. At strong and moderate supercooling (T_x = 25 and 40°C), the thermodynamic driving force for nucleation was high; hence, a large number of nuclei were formed. Moreover, the strong driving force towards crystallization resulting from strong supercooling promoted fast crystal domain growth. These factors led to the small crystalline domains with straight boundaries as described. For weak supercooling (T_x = 50°C), on the other hand, the thermodynamic driving force for nucleation was low, but the high mobility of the polymers allowed them to diffuse rapidly towards the growth front. Moreover, close to T_m of PEO, the crystalline chains might have the tendency to assume conformations with maximum chain stretching since their mobility is high. In this way, a long time is required to achieve these maximum chain stretching conformations and hence can only be obtained when the crystal domain growth is slow. The maximum chain stretching that might occur at T_x = 50°C, can be confirmed by GISAXS.

3.2.2 Internal film structure

Varying the degree of supercooling has a strong influence on the crystalline orientation as well as the mesophase structure. In order to characterize the inner film structure on the mesoscopic length scale, GISAXS was found to be an ideal tool. GIWAXS was employed to investigate the orientation of the crystalline lamellae and to provide information on the degree of PEO chain folding.

3.2.2.1   Lamellar mesophase

2D GISAXS images of the crystallized films measured at room temperature (Fig. 3.5) show intensity maxima only along the q_z axis; no maxima were observed at finite q_y. We attribute the former to diffuse Bragg sheets from layered structures in the films, being parallel to the film surface. An analysis of their positions allowed us to obtain information on the repeat distance. Figure 3.6 shows the intensity profiles along q_z for the films crystallized at 25, 40 and 50°C,

respectively. In all intensity profiles, weak diffuse Bragg sheets can be observed in addition to the specularly reflected beam and the Yoneda peak of the polymer film. At $T_x = 25°C$, the diffuse Bragg sheets were very weak, whereas at 40 and 50°C, they were more pronounced. This might be due to irregular packing of the lamellae at $T_x = 25°C$ and better packing at $T_x = 40°C$ and $T_x = 50°C$
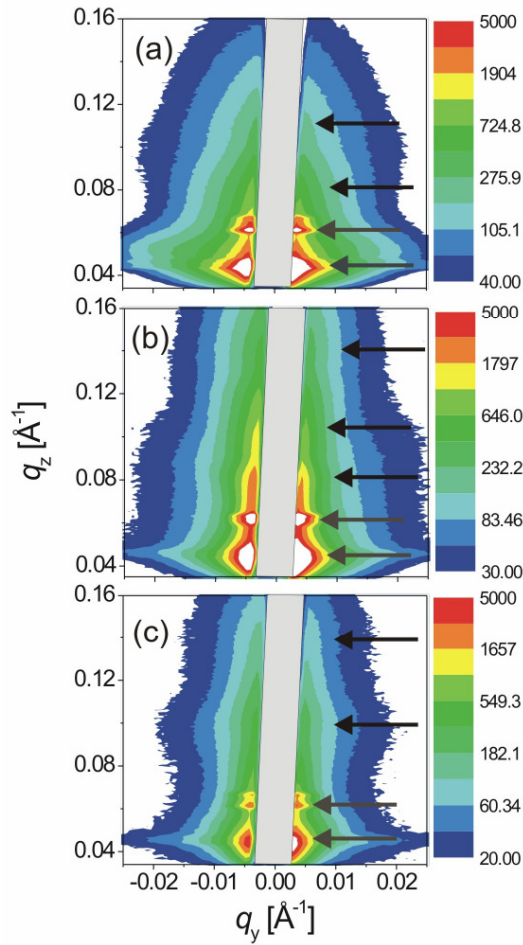
Figure 3.5. GISAXS images of thin films crystallized at $T_x = 25°C$ (*a*) $T_x = 40°C$ (*b*) and $T_x = 50°C$ (*c*), all measured at $\alpha_i = 0.39°$. The grey rectangles indicate the beamstop. The first two arrows (from the bottom) show the position of the Yoneda and specularly reflected peak intensities, respectively, followed by arrows showing the positions of the diffuse Bragg sheets.
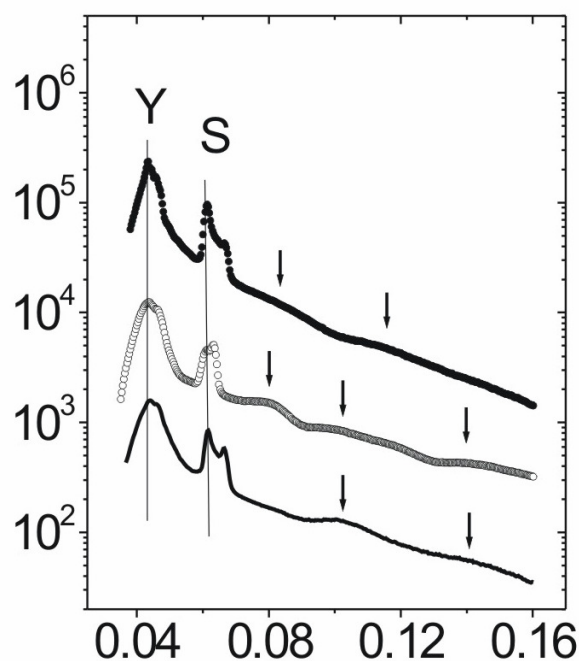
Figure 3.6. Intensity profiles along q_z from the GISAXS images in figure 3.5. T_x = 25°C (●), T_x = 40°C (○) and T_x = 50°C (*line*). The line marked *Y* and *S* show the position of the Yoneda and the specularly reflected peak, respectively while the arrows show the position of the *DBS* (diffuse Bragg sheets).

To quantify the lamellar repeat distances (*L*), the positions of the diffuse Bragg sheets were plotted as a function of k_{iz} together with fits of the DWBA model for stacked lamellae given in equation 3. For T_x = 25, 40 and 50°C (Fig. 3.7), the repeat distances were found to be 16.0 ± 0.5 nm, 20.0 ± 0.7 nm and 21.0 ± 0.5 nm, respectively. Odd and even orders were present which conclude that the lamellae were not symmetric.
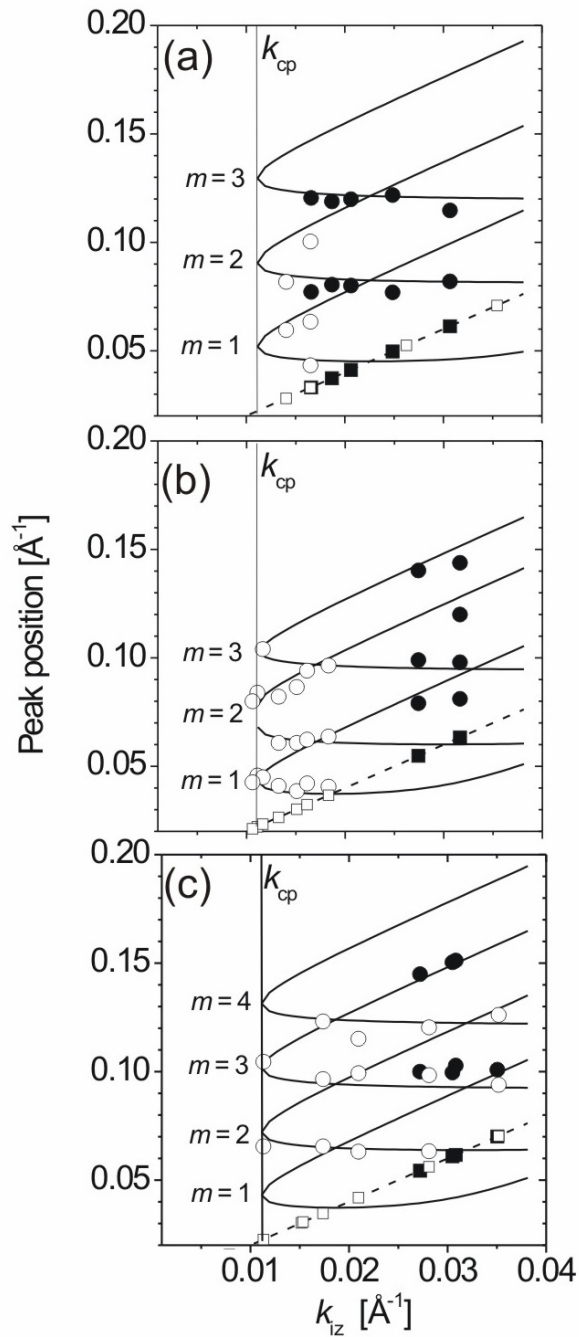
Figure 3.7. Peak positions q_z of the intensity profiles from figure 3.6 as a function of k_{iz}. $T_x = 25°C$ (*a*), $T_x = 40°C$ (*b*) and $T_x = 50°C$ (c). Squares: specularly reflected beam, circles: diffuse Bragg sheets. Lines: fits of Eq. 2. Open symbols: measured at CHESS *D*1, filled symbols: measured at HASYLAB BW4. In (*c*), the DBS with $m = 1$ is close to the intense specularly reflected beam and can therefore not be resolved. The positions of the Yoneda were not included.

In order to relate the lamellar thickness and the terrace height to the chain conformations, we estimate the dimensions of a fully extended and a folded PEO block and of a coiled PS block. The chain length of the fully extended PEO of molar mass 3,000 g/mol is: $\kappa = l_u N \sim 19$ nm (where $l_u = 0.2783$ nm is the monomer length and the degree of polymerization $N = 68$) [110]. The extended chain length of the PS block of equal molar mass is: $\kappa = l_u N \sim 4.5$ nm ($l_u = 0.154$ nm and $N = 29$), but the length of PS block that can be obtained for a once folded PEO chains is: $\kappa = \sim 2$ nm, calculated by dividing the volume of PS (i.e. 0.852 nm^3, $\rho = 1.05$ g/cm^3) by the cross-sectional area of two PEO stems in the crystalline state {i.e. (0.656 nm x 1.304 nm)/2, based on 4 chains per unit cell ref.[98]}. This suggests that the length of a fully extended PS-*b*-PEO diblock copolymer is 19 nm + 4.5 nm = 23.5 nm, whereas the length of PS-*b*-PEO for a once folded PEO chain is 9.5 nm + 2 nm = 11.5 nm (Fig. 3.8). Hence, the AFM surface height for films crystallized at $T_x = 50°C$ (Fig. 3.4*d*) can be attributed to the length of PS-*b*-PEO for a once folded PEO chain (monolayer).
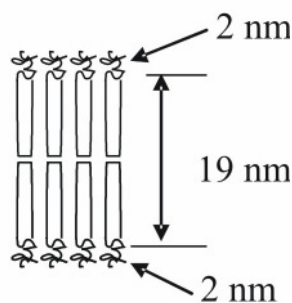
Figure 3.8. Schematic illustration of once-folded PEO chain

The decrease in the repeat distances with decreasing T_x can in principle be caused by a combination of (i) a decrease in the number of folding of the PEO chains, (ii) the PEO crystallites orienting with the *c*-axis more tilted with respect to the lamellar interface and (iii) the lower degree of stretching of the amorphous PS blocks in order to accommodate the increasing interfacial area of the crystalline PEO blocks. In order to distinguish between these different scenarios, we have investigated the crystalline orientation by GIWAXS.

3.2.2.2   Crystalline orientation

In this section, we present GIWAXS results on the crystalline structure of PEO in the films crystallized at T_x = 25 and 50°C. These two films show very different surface morphologies (Figs. 3.3 and 3.4). The Bragg reflections observed in the images (Fig. 3.9*a* and *b*) were indexed by simulating complete 2D diffraction images (Fig. 3.9*c* and *d*). The 2D GIWAXS images obtained experimentally (Fig. 3.9*a* and *b*) show a clear distinction of the crystalline morphology in the two films. At T_x = 25°C (Fig. 3.9*a*), two strong and rather isotropic rings can be observed: The first is from the *120* reflection, whereas the second belongs to a group of reflections, namely *032*, *-132*, *-212*, and *112*. For films crystallized at T_x = 50°C (Fig. 3.9*b*), two peaks with a significantly narrower azimuthal width were observed. These peaks were indexed as *120* and *032* reflections.
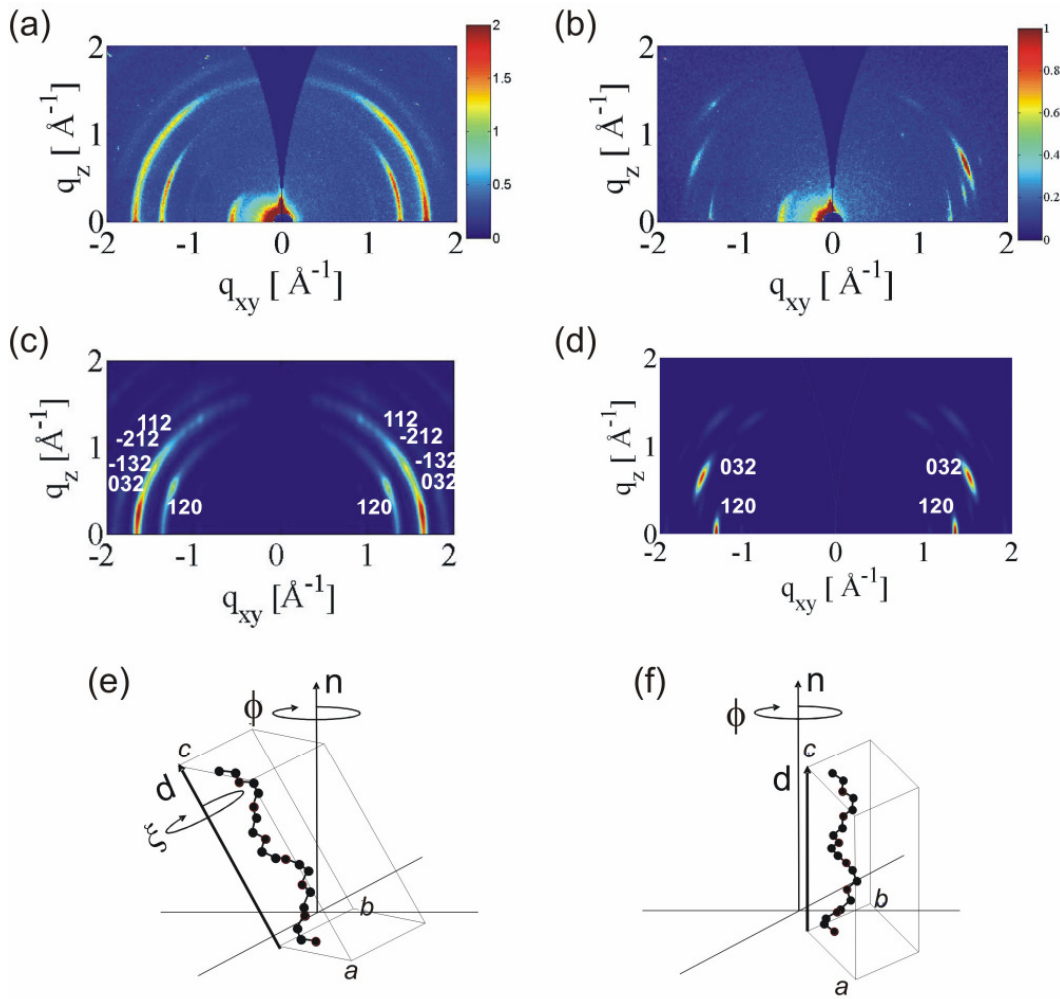
Figure 3.9. Experimental 2D GIWAXS images of thin films crystallized at $T_x = 25°C$ (a) and 50°C (b). The strong intensities close to the origin in (a) and (b) are due to parasitic scattering. Corresponding simulated 2D patterns of the diffraction from PEO crystals for $T_x = 25$ (c) and 50°C (d). (e) and (f) are models used for simulating the 2D patterns at $T_x = 25$ and 50°C, respectively. (For simplicity, only one stem is shown in the unit cell sketches). For the 25°C model, the angle between the sample normal **n** and the dominant direction **d** was 35°, and was allowed to deviate from this angle by a broad Kratky distribution with width (FWHM) ~40°. Similarly, for the 50°C model, **d** was taken parallel to **n**, and the distribution was much narrower, FWHM ~ 6°. Note that for a uniaxial model, all orientations about ξ are equally likely, and with no in-plane orientation, there is no dependence on the angle ϕ.

Attempts were made to simulate both experimental images by changing as few parameters as possible. As it turned out, the simulations shown in figures 3.9*c* and 3.9*d* could be obtained by changing just two parameters; a) the dominant (director) orientation angle χ of the unit cell *c*-axis with respect to the sample surface normal, and b) the width of the ODF. Whereas the 50 °C sample was best modelled assuming that the *c*-axis of the unit cell (and thus the polymer main chains) is parallel to the sample surface normal, the 25 °C sample was better fitted if tilting the director, i.e. the most likely orientation, by an angle of about 35°. The Kratky parameters used in the presented simulations were $\lambda_K \sim 4$ (FWHM ~40°) and $\lambda_K = 1.4$ (FWHM ~6°) for 25 and 50 °C, respectively (where λ_K is the elongation ratio of the stiff rods in the Kratky model). The uncertainty of these widths is about 10%. These results strengthen the observations from the other measuremnts: there are apparently different growth mechanisms for different degrees of supercooling, with a low degree of supercooling resulting in films with a much higher order. We noted that the asymmetry in the intensities of figure 3.9*b* was due to the large crystalline domains: the assumed "2D powder symmetry" breaks down because the scattering volume contains comparably few domains.
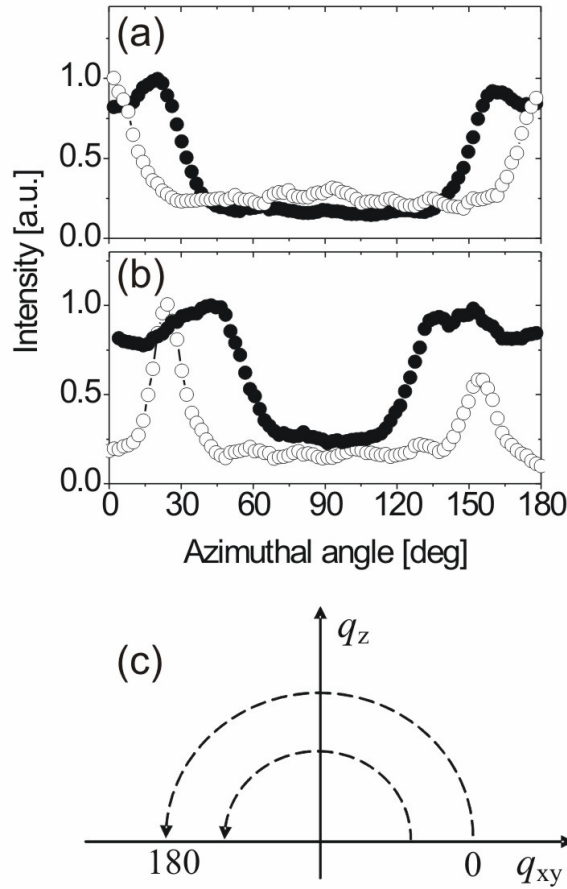
Figure 3.10. Azimuthal intensity profiles obtained from the GIWAXS images (Fig. 3.8*a* and *b*) counter clockwise. (*a*) Intensity profiles at q = 1.356 Å^{-1}, i.e. along the *120* reflections, and (*b*) at q = 1.645 Å^{-1}, i.e. along the *032* and *032, -132, -212, 112* reflections, for films crystallized at T_x = 25°C (●) and at T_x = 50°C (○). (c) illustrations of how intensity profiles were made.

The width of the distribution of inclination angle χ reflected in the azimuthal intensity distributions of the Bragg reflections. The intensity distributions from the two films are as shown in fig. 3.10*a* for q = 1.356 Å^{-1}, i.e. through the *120* reflection, and in figure 3.10*b* for q = 1.645 Å^{-1}, i.e. through the *032* reflection. Also from these plots it was seen that the *120* distribution is broader in the film crystallized at T_x = 25°C than in the film crystallized at T_x = 50°C (Fig. 3.10*a*). For film crystallized at T_x = 25°C, the *120* distribution has maxima around 25° and 155°, but the intensity decreases steadily towards the 40° and 140° (Fig 3.10*a*). At T_x = 50°C, the *120* distribution has the maxima at 0° and 180° with a

59

narrow distribution. In figure 3.10*b*, the intensity distributions for the *032* reflections show a wide angular distribution for the film crystallized at $T_x = 25°C$. These distributions incorporate contributions from the group of reflections *032*, -*132*, *-212*, and *112*. For films crystallized at $T_x = 50°C$ (Fig. 3.10*b*), there are narrower distributions having the peak maxima at 30° and 150° which are attributed to only the *032* reflections. In short, the azimuthal intensity distributions illustrate and quantify the changes in the peak positions as well as the orientation distribution which could not be clearly seen on the experimental 2D data. We have observed how these intensity distributions differ.

3.2.2.3   Crystal grain size and crystallinity

The crystal grain sizes and crystallinity were estimated by comparing the synchrotron GIWAXS intensity profiles (Fig. 3.11) obtained from the two films crystallized at $T_x = 25$ and 50°C. In this high-resolution GIWAXS experiment, the *020*, *110*, *120* and the *032* peaks were observed. The weak *020* and *110* peaks can be observed on the simulated and the experimental data (Fig. 3.8). Our observations from the OM and AFM images (Figs. 3.3 and 3.4) show that the crystalline domain sizes were quite large, namely in the $\delta = 10$ -100 µm range. The diffraction peak widths expected for these domain sizes are thus very small ($\Delta q < 2\pi / \delta \sim 0.0006$ Å^{-1}). We have used the *120* reflections in estimating the above parameters since it represent growth along the film lateral.

We focused on the grain (granular domain) sizes of the film crystallized at $T_x = 25°C$ since the lateral size of the sub-units increased with decreasing supercooling and was already beyond the resolution limit of the instrument for the sample crystallized at $T_x = 50°C$. As shown in section 2.2.6.2, last paragraph (i.e. Fig. 2.19), we obtained a crystal grain size of ~ 81 nm using the Scherrer's formula [100] (see also appendix B).
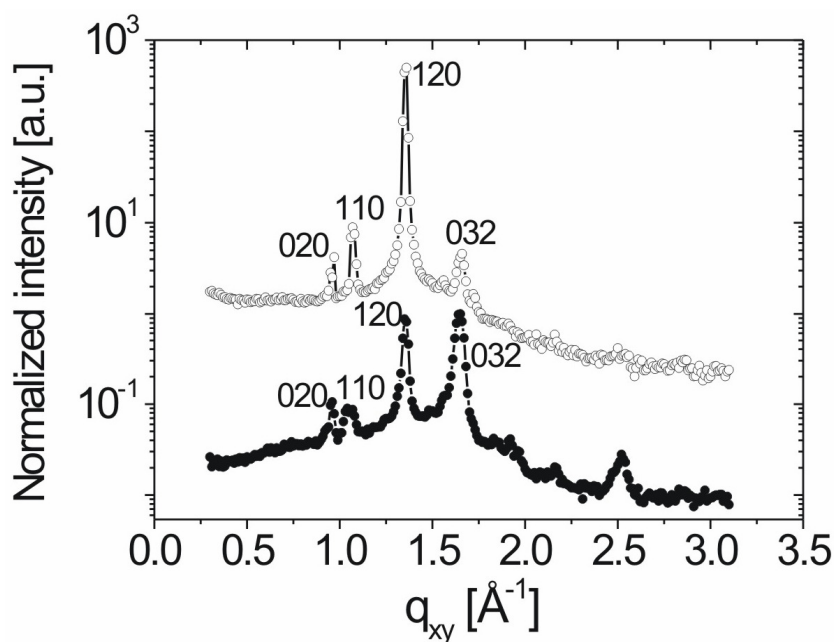
Figure 3.11. GIXD intensity profiles for thin films crystallized at T_x = 25°C (●) and T_x = 50°C (○) measured along the in-plane (i.e. along the lateral direction). The lines are guides to the eye.

A rough estimation of the degree of crystallinity was attempted by comparing the areas under the crystalline peak and the amorphous halo, as observed in the in-plane scans. The percentage of crystalline domains in the films crystallized at T_x = 25 and 50°C was obtained to be 62 and 98 %, respectively (i.e. in the film plane). From the degree of crystallinity, was concluded that chain attachment at the growth front (i.e. along the *b*-axis) were more perfect at T_x = 50°C than at T_x = 25°C.

3.4 Summary

We conclude that by varying the degree of supercooling, different surface textures and internal film structures were obtained. A summary of our results is as shown in table 3.1.

Table 3.1. Summary of results on unconfined crystallization

Samples	T_x (°C)	Growth Rate (µm/s)	AFM terrace height, D (Å)	GISAXS $2D$ (Å)	GIWAXS fwhm χ (°)	[*]Mean orientation (°)	Crystallinity (%)
$T_x = 25°C$	25	5.4	-	160 ± 5	40		62
$T_x = 40°C$	40	5.5	-	200 ± 7	-		
$T_x = 50°C$	50	0.002	110 ± 5	210 ± 5	6		98

[*]Orientation with respect to the film normal.

At weak supercooling, $T_x = 50°C$, we have thus found that only few nuclei form and large crystalline domains grow at a low rate, resulting in surface terraces having a height comparable to a monolayer of once-folded PEO blocks oriented normal to the substrate plane and covered with the corresponding coiled PS blocks (Fig. 3.12). The repeat distance within the film is about twice as high (21.0 ± 0.5 nm), which is consistent with bilayers having the same conformation. This perpendicular orientation of the chain stems is corroborated by the 2D GIWAXS map and is consistent with the observations in the bulk [39]. The low growth rate seems to enable nearly perfect crystal growth within the film plane, as expressed by the very small value of the width of the distribution of tilt angles (GIWAXS) and the rather smooth surface topography (AFM). This is promoted by the relatively high mobility of the PS blocks at this elevated temperature, enabling lateral diffusion of the copolymers towards the growth front.
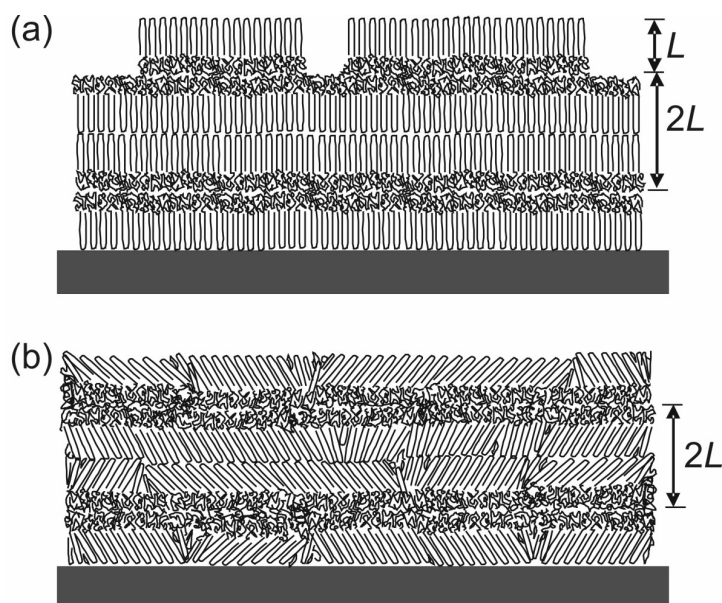
Figure 3.12. Schematics of the structures of films crystallized at $T_x = 25°C$ (*a*) and 50°C (*b*). In (*b*), $D = 11.0 \pm 0.5$ nm obtained from AFM surface analyses (Fig. 3.4*d*) and represent the length of one diblock in the crystalline state while $2D = 21.0 \pm 0.5$ nm measured from GISAXS and represent twice the length of one diblock in the crystalline state for films crystallized $T_x = 50°C$ (Fig. 3.7*c*). In (a), $2D = 16.0 \pm 0.5$ nm measured from GISAXS for films crystallized $T_x = 25°C$ (Fig. 3.7*a*).

In contrast, at strong supercooling, the growth rate is increased by a factor of $\sim 5 \times 10^3$, and large spherulitic regions having diameters of about 50 µm are formed (Fig. 3.2*b*). They consist of small, elongated crystallites. The repeat distance (i.e. 16.0 ± 0.5 nm) inside the film is consistent with an inclination of the PEO chain stems with respect to the crystallite interfaces. The average inclination angle is 35° with a wide distribution. The mean inclination angle of 35° leads to $2D \times \cos (35°) = \sim 17.00 \pm 0.6$ nm (mean value) which is in good agreement with the 16.0 ± 0.5 nm value obtained (as illustrated in figure 3.12). The orientation of the PEO blocks is thus not uniform. We conclude that each of the domains of size 100 nm observed in the AFM image (Fig. 3.4*a*) consists of chains having the same inclination angle. This angle differs from domain to domain and is presumably uncorrelated. We conclude that the spherulitic domains, which grow at a constant growth rate from a single nucleation point, are not built up from uniformly

oriented crystalline molecules. This explains the granular and comparatively rough surface texture seen in Figure 3.4*a*. A possible reason for such loss of unique orientation are repeated nucleation events at the growth front (Fig. 3.13), as demonstrated previously in phase-field simulations [104]. The translational and rotational diffusion of PEO blocks may be hampered by the more rigid PS domain at this low temperature. Such a mechanism cannot directly be identified with bulk samples, but in thin film geometry.
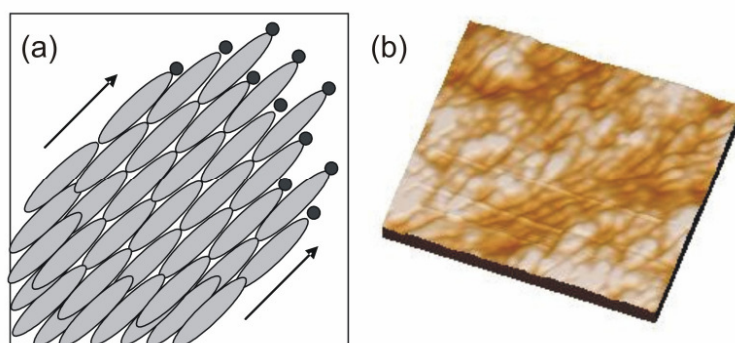
Figure 3.13. (*a*) Schematic illustration of the repeated nucleation for the formation of small sub-unit domains predicted by the phase fields simulations [104]. Oval objects represent small crystalline domains and small black dots represent the nucleation point for the crystalline domain formation. (*b*) Show the AFM image (1.4 µm × 1.2 µm) of the small sub-unit domains observed experimentally.

Interestingly, the size of these crystallites is in the same range as determined by Strobl et al. for various, chemically different polymers at similar degrees of supercooling [105]. In this work, we could observe these sub-units at the surface by AFM (i.e. ~100 nm) and within the thin film by GIWAXS (i.e. ~ 81 nm). This small size of the crystallites was taken as strong evidence for a general route of polymer crystallization leading to a granular substructure of crystalline polymer lamellae. Thus, the experimental results presented here on polymer crystallization provide clear support for the hypothesis that large, quasi two-dimensional crystalline polymer domains (i.e. crystalline lamellae characterized by a well-defined repeat distance) are actually composed of small sub-units. The lateral size of these sub-units increases with decreasing supercooling and are already beyond

the resolution limit of the GIWAXS instrument for the sample crystallized at $T_x = 50°C$.

Accordingly, films crystallized at $T_x = 40°C$ represent an intermediate case between films crystallized at $T_x = 25°C$ and 50°C. For $T_x = 40°C$, the lamellar thickness was as large as the one at $T_x = 50°C$, pointing to a similar crystalline orientation and folding state of the PEO blocks. However, the growth rate and the surface texture closely resembled those obtained at $T_x = 25°C$. We propose that the PEO crystalline chains might have intermediate mean orientations between films crystallized at $T_x = 25°C$ and 50°C.

Our findings are also in qualitative agreement with the observations on shear-aligned PS-*b*-EO in the bulk [39], in spite of the differences in sample preparation and alignment. However, in addition to measuring the mean inclination angle, we have also estimated the width of the variation around this angle and we have found that the lateral extension of crystalline domains is consistent with the characteristic size of surface features observed by AFM.

The decrease of mobility of the PS domain with decreasing T_x enhances the effect of supercooling, in contrast to the previously studied poly(butadiene-*b*-(ethylene oxide)) system [45,111]. Future systematic experiments slowly varying the crystallization temperature may be able to determine whether the transition from tilted to non-tilted chains within the crystalline polymer lamellae is abrupt or gradual.

Our observations show that a detailed structural analysis can explain observed surface morphologies and relate them to the different mechanisms of crystal growth. The thin film geometry used here offers an ideal possibility to correlate detailed structural analyses on various length scales with the direct-space observation of crystal growth via microscopy techniques. The understanding of the crystallization mechanism is important for the use of block copolymers as functional materials, such as templates or inorganic/organic hybrids.

Chapter 4

Soft crystallization confinement

4.1   Aim of work

The aim of this work is to investigate the break away of PEO crystals from the soft rubbery confinement.

Polymer crystallization is frustrated by relatively large free energy barriers, which arise from the necessity to reorganize polymer conformations into ordered states [112,113]. For small molecules, crystallization proceeds by the mechanism of nucleation and growth. For polymers, during the nucleation stage, monomers come from different chains or different locations along the chain contour of the same chain to form nuclei. Hence, there is a competition by several nuclei for the acquisition of monomers from the strands not yet incorporated into the crystalline phase. Confining crystallisable polymers chains in one, two or three dimensions may affect the mechanism of nucleation and growth. One such confinement is by attaching a non-crystallisable monomeric chain (i.e. amorphous chains) covalently to the crystallisable chain to form semicrystalline diblock copolymer.

We present here the time dependent crystallization behaviour in a low molar mass thin film of cylinder-forming PI-*b*-PEO (IEO) diblock copolymer with PEO being the minority block. The rate of crystal nucleation was low but once these nuclei were formed, they grow slowly destroying the rubbery PI matrix. In this study, long time was required to crystallize the system with the focus on the disruption mechanism of the PI matrix by the PEO crystals. The thin film geometry allowed us to visualize the growth of the PEO crystals within the PI domain.

4.2 Results and discussions

In the following, we report our observations made on the surface and inside the thin films from PI-*b*-PEO which was prepared and crystallized for several months. We give detail analysis on the change in surface morphology caused by PEO crystallization which disrupts the microdomain structures. The microdomain structure before and after the crystallization within the thin films were analyzed. We finally compared the findings and proposed mechanisms for structure formation before and after the disruption by crystallization.

4.2.1 Freshly prepared films.

In figure 4.1*a*, the surface morphology obtained (about a few minutes) after spin-coating showed some imbedded small particles (bright dots) on the thin film. These particles were observed at every locations of the film surface. To obtain a homogeneous film, the film was heated above the $T_{m,PEO}$ and the $T_m^{°}{}_{,PI}$ at 62°C for a few minutes. This temperature was chosen to avoid dewetting of the film at higher temperatures. Figure 4.1*b* shows the melt phase of the film surface with absence of the imbedded small particles. Flat layered bright elevations were formed. A few minutes after quenching back to room temperature, flat surface with small (size of ~ 10µm) rounded randomly distributed holes close to circular shape was obtained as shown in figure 4.1*c*. Figure 4.1*d* shows AFM phase image from figure 1*c* with slight phase contrast.
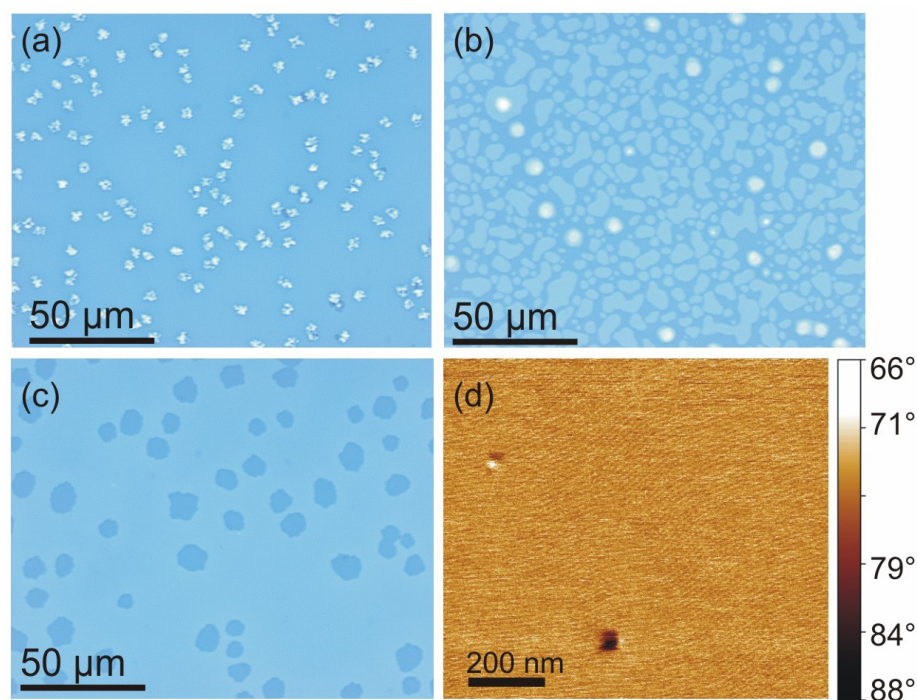
Figure 4.1. Surface analysis of prepared IEO thin film. OM images after spin-coating (*a*), at 62°C (*b*) and after quenching to room temperature (*c*). (*d*) AFM phase image at room temperature.

Our observations show that, after spin-coating, small crystal nuclei were formed indicated by the bright spots on figure 4.1*a*. This might occur directly from solution as a result of crystalline salt aggregation which was transferred onto the film surface. Above the $T_{m,PEO}$, these nuclei were absent. The slight phase contrast from the AFM suggests a parallel mesophase orientation with respect to the film substrate. To proof this, we performed GISAXS measurements to investigate the hidden mesophase structure within the thin film.

Figure 4.2*a* shows 2D GISAXS image with Bragg reflections which are the first order of the hexagonal morphology with the cylinders lying in the film plane. The image shows half of the full reciprocal space lattice because of the thin film geometry. The positions of these reflections were determined from the intensity profiles along q_z at $q_y \approx 0$ (i.e. the vertical, Fig. 4.2*b*) and q_y at $q_z = 0.037$ to $+0.047$ Å^{-1}. (i.e. the horizontal, Fig. 2*c*). The actual *repeat distance, L,* of the

hexagonal cylinders in the reciprocal space is rotated by an angle of 30° into the real space as shown in figure 4.3 [90]. Using the peak position along the film normal and from equation 2, *L* was obtained to be 10.0 ± 0.5 nm.
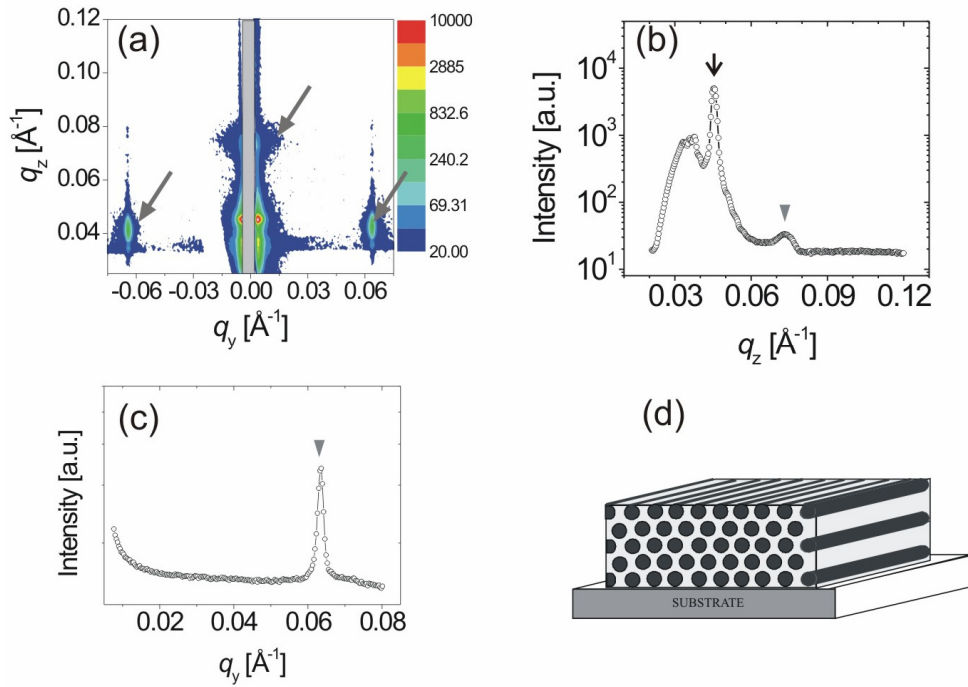
Figure 4.2. GISAXS measurement of prepared PI-*b*-PEO thin film. (*a*) 2D GISAXS image measured at $\alpha_i = 0.3°$. The grey rectangles represent the beamstop. The arrows indicate the positions of the Bragg reflections from the hexagonal lattice. (*b*) Intensity profile made on the GISAXS image along the q_z integrated over the region $q_y = -0.009$ to $+0.009$ Å^{-1}. The ↓ and ▼ symbols represent the position of the specularly reflected peak and the Bragg reflection. (*c*) Intensity profile made on the GISAXS image along the q_y integrated over the region $q_z = 0.037$ to $+0.047$ Å^{-1}. ▼ represent the position of the Bragg reflection. (*d*) Model for hexagonal morphology with the cylinders lying in the film plane.
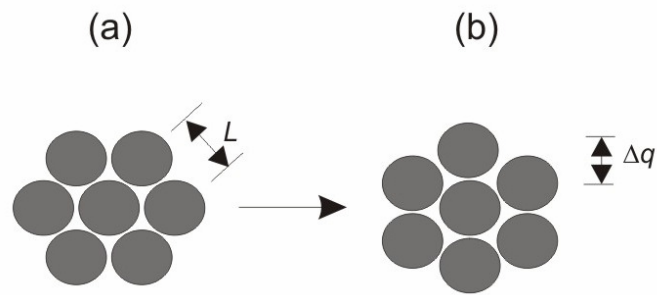
Figure 4.3. One dimension hexagonal packing of cylinders in the real (*a*) and the reciprocal space (*b*). Adopted from ref 90.

From the GISAXS analysis, we concluded that that the freshly prepared film have hexagonal cylinders with the cylinders lying parallel to the film/substrate interface having repeat distance of 10 ± 0.5 nm. This caused the flattening of the surface with less phase contrast in the AFM phase image data. The phase contrast was weak because the minority PEO cylinders are covered by a thin layer of soft PI.

4.2.2 Crystal growth.

In figure 4.4*a* and after 41 days at room temperature, we observed several crystalline domains from the PEO crystals having circular shape and a radius of ~90 µm. In figure 4.4*b*, we observed that the crystalline domain is surrounded by a bright circular ring having dendritic fingers at the outer edges. In the inner part of the crystalline domain, elongated domains were present (Fig. 4.4*c*).
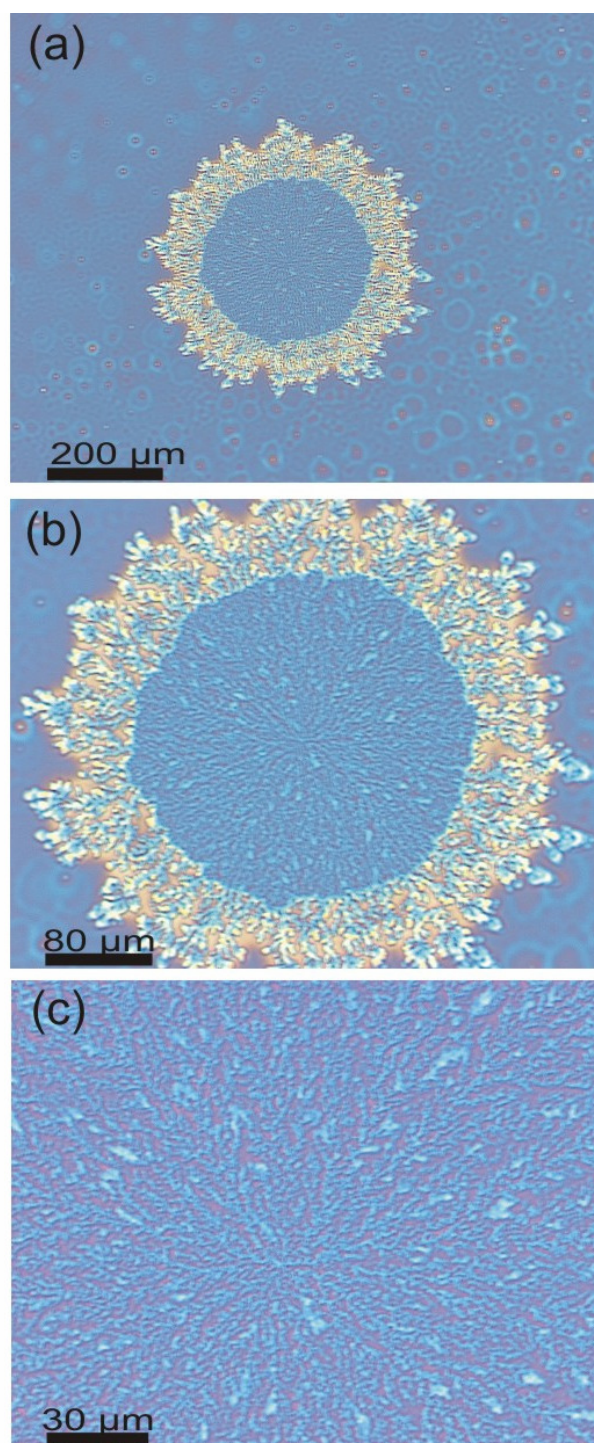
Figure 4.4. OM micrographs of IEO thin film showing growth of crystal domain after 41 days. (*a*) Circular shape crystal domain growth. (*b*) Surface morphology of crystal domain with PEO chain diffusion at growth front (bright regions). (*c*) Flake-like crystalline domain after PEO crystallization.

The long time crystallization can be attributed to the large free energy barriers which must be overcome before crystallization. This was partly caused by the inadequate short PEO chains required to form the crystal nucleus. It might have taken some time for the PEO chains to diffuse through the rubbery PI matrix. Once the nucleus was formed the crystals grow slowly though the soft rubbery PI matrix to assume preferred conformations.

From morphologies obtained, the bright circular outer edges can be attributed to the small crystalline domains, from the phase-field simulations [104], which were built up from uniformly oriented crystalline molecules and formed from repeated nucleation event at the growth front. These dendritic structures from the PEO crystals have been well-studied [48,49,50]. It is interesting to note that, we did not observe any nucleation during the first 7 hours after quenching.

4.2.3 Fully crystallized films.

After 148 days, we observe a complete change in surface morphology at all locations of the film (Fig. 4.5*a,b*). This unique morphology did not change with time. The morphology consisted of several PEO dendrites distributed evenly on the surface having heights greater than the original surface of the polymer matrix. In figure 4.5*c* and *d*, the AFM topography image and the line cut show that these finger-like pattern have flat terraces with terrace heights of 10.0 ± 1.0 nm.
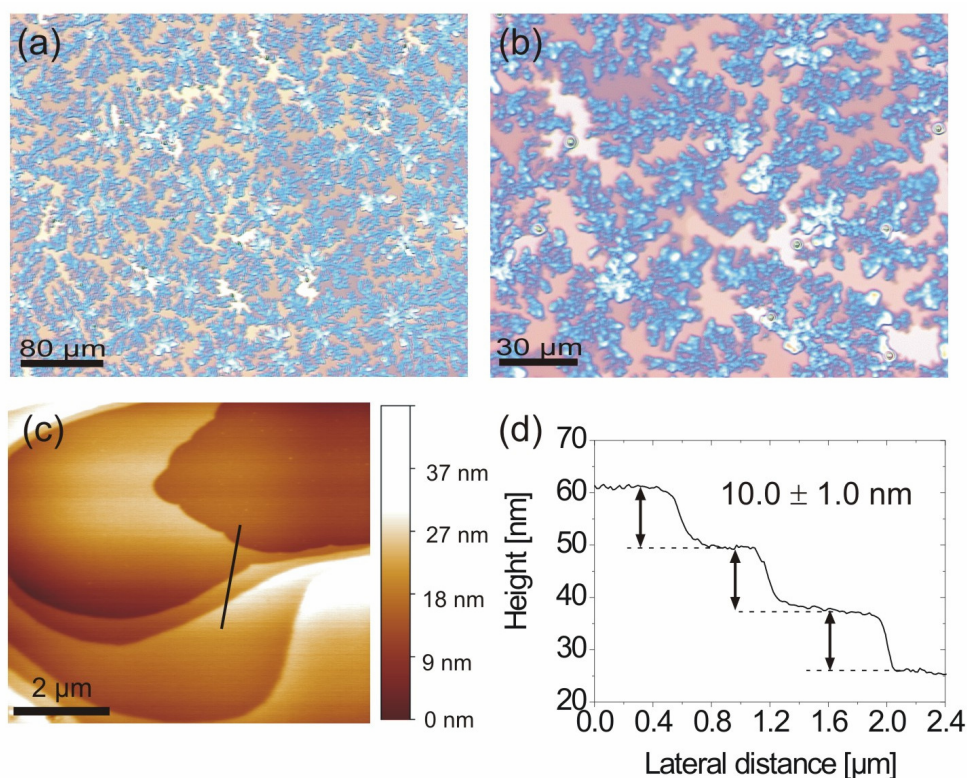
Figure 4.5. Optical micrographs showing global (*a*) and local (*b*) dendritic surface morphology after 148 days of full crystallization. (*c*) AFM topography image of the surface texture and (*d*) cross-section line cut indicated on (*c*).

The finger-like dendritic patterns are completely different from the crystalline domain observed after 41 days on figure 4.4*c*. The crystallized PEO chains might assume preferred conformations after complete crystallization and incorporated chains which were previously not crystallized. The intriguing observations was the elevated texture from the AFM with step-height of 10.0 ± 1.0 nm. At this point, we anticipate the destruction of the hexagonal morphology by crystallization. In this view, we performed GISAXS investigation on the film completely crystallized film.

2D GISAXS image (Fig. 4.6*a*) of the fully crystallized films shows no Bragg reflections from the hexagonal cylinder morphology. Instead, the intensity profiles along the q_z (Fig. 4.6*b*) and q_y (Fig. 4.6*c*) suggest a lamellar morphology: two peaks were observed at $q_z = 0.073$ and 0.110 Å^{-1} whereas no peaks were observed at finite q_y. We attribute the former to diffuse Bragg sheets from layered structures

in the films, being parallel to the film surface. An analysis of their positions allowed us to obtain information on the repeat distance. For this purpose, the positions of the diffuse Bragg sheets were plotted as a function of α_i together with fits of the DWBA model for stacked lamellae given in equation 1 and a fit was obtained with $L = 9.3 \pm 0.3$ nm.
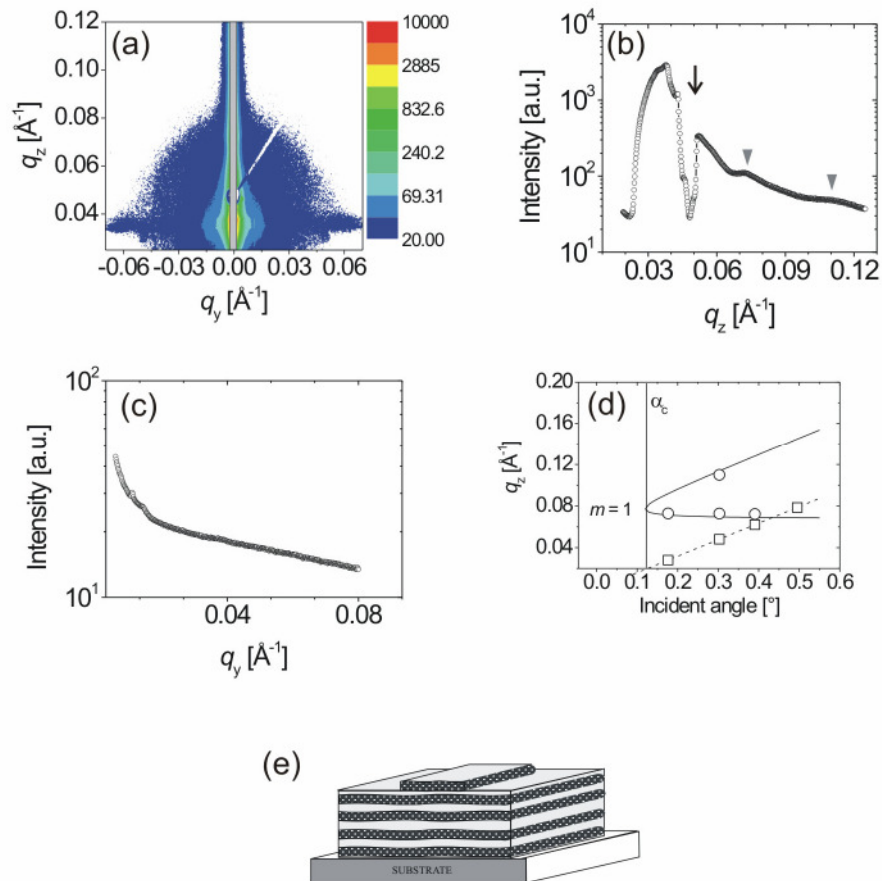
Figure 4.6. GISAXS measurement of IEO thin film after complete crystallization at 148 days. (*a*) 2D GISAXS image measured at $\alpha_i = 0.3°$. The grey rectangle and oval shapes indicate the beamstops for the direct beam and the intense specularly reflected peak, respectively. (*b*) Intensity profile made on the GISAXS image along the q_z integrated over the region $q_y = -0.009$ to $+0.009$ Å^{-1}. The ↓ and ▼ symbols represent the position of the specularly reflected peak and the diffuse Bragg sheets (DBS). (*c*) Intensity profile made on the GISAXS image along the q_y integrated over the region $q_z = 0.037$ to $+0.047$ Å^{-1}. (*d*) Peak positions of the DBS, q_z, from (*b*) as a function of α_i. Squares: specularly reflected beam, circles: DBS. Lines: fits of Eq. 1. (*e*) Model for parallel lamellar morphology.

The GISAXS analysis proofs that hexagonal cylinder morphology has been destroyed by the PEO crystallization. The hexagonal lattice morphology with $L = 10.0 \pm 0.5$ nm was transformed into lamellar sheets parallel to the surface with $L = 9.3 \pm 0.3$ nm. This can be compared to the surface terrace height of 10.0 ± 1.0 nm obtained from the AFM image. To get information on the crystalline orientation, GIWAXS experiments were performed.

GIWAXS experiment for the freshly prepared and the completely crystallized film show significant differences (Fig. 4.7). Whereas no Bragg reflection from PEO was observed in the freshly prepared film, reflection was present after 148 days. The reflection was assigned to the *120* reflection after calculation from the monoclinic crystalline lattice [98]. The *120* peak (from calculation) observed after complete crystallization reveals crystals growth along the *b*-axis of the PEO unit cell. It means that the PEO chain stems (*c*-axis) become perpendicular to the film/substrate interface. The models in figure 4.8 show schematic representation of the non-crystallized PEO chains in the freshly prepared films and the lateral growth of the PEO crystalline chains surrounded by the PI domains.
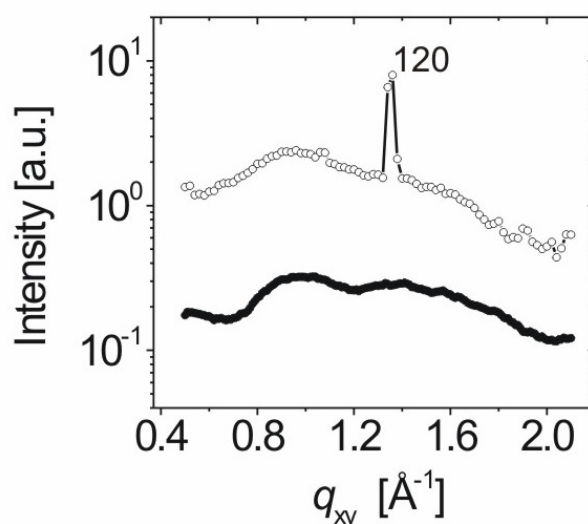
Figure 4.7. GIXD intensity profiles for IEO thin films for the freshly prepared (●) and completely crystallized at 148 days (○). The lines are guides to the eye.
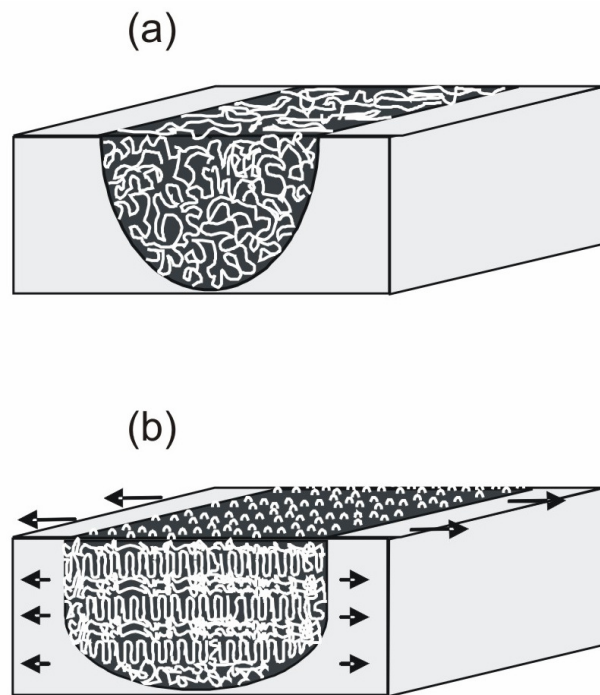
Figure 4.8. Schematic model of the PEO crystalline chains in the freshly prepared (*a*) and completely crystallized (*b*) thin films.

XR measurements (Fig. 4.9) give strong evidence to the fact that the hexagonal morphology has been transformed into lateral structures after complete crystallization. For the freshly prepared film, a large number of well-defined Kiessig fringes with one Bragg reflection were observed. For the completely crystallized film, Kiessig fringes were weak but two lamellar Bragg reflections equidistant at $1q$ and $2q$.
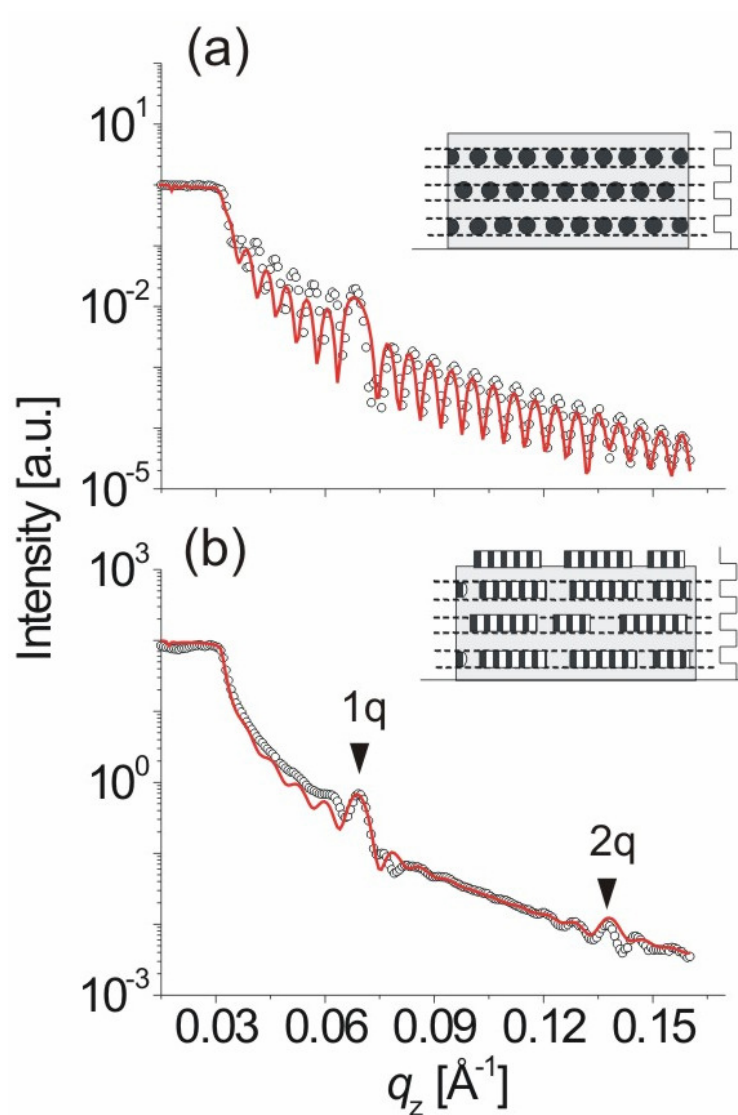
Figure 4.9. X-ray reflectivity curves for the freshly prepared (*a*) and completely crystallized (*b*) IEO thin films. Inserts show models used for the fitting. Dark circles and gray region represent PEO domain and PI matrix, respectively. For the mixture of PI/PEO, scattering length densities of $\rho_s = 4.938 \times 10^{-6}$ Å^{-2} and im$\rho_s = 8.033 \times 10^{-9}$ Å^{-2} were used in the model. In (*b*), Bragg peaks found at $1q = 0.068$ Å^{-1} and $2q = 0.137$ Å^{-1}.

The two XR curves were fitted using the inserted models shown in figure 4.9a and b. For the freshly prepared film (Fig. 4.9a), PEO cylinder diameters of 5 nm with repeat distance of 9.5 nm as well as internal interface roughness of 0.4 nm between the blocks were used. In the fully crystallized films (Fig. 4.9b), 6.2 nm thick PEO crystalline platelets with the repeat distance of 9.2 nm and surface roughness of 10 nm were used (internal block interface roughness of 1.4 nm was used). The 10 nm was because of the terraced height of 10.0 ± 1.0 nm observed on the AFM image (Fig. 4.5c). In all, film thickness of 110 nm was used in both fittings.

The repeat distance of 9.3 ± 0.3 nm for the fully crystallized film speculates either a once-folded or intergiditating chain pattern. The chain length of the fully extended PEO of molar mass 1,100 g/mol is: $\kappa = l_u N \sim 7$ nm (where $l_u = 2.783$ Å is the monomer length and the degree of polymerization $N = 25$) [110]. From this value and from the repeat distance, the PEO crystalline chains can only be fully extended with the chains interdigitating or can be once-folded.

4.3   Summary.

We have observed slow breakout crystallization from PEO crystals confined in the hexagonal cylinder morphology with the cylinders lying in the film plane. The soft confinement provided by the rubbery PI matrix promoted, initially, smooth surface texture. Nucleation could not be observed within the confined cylinders but flake-like crystalline domains with a radius of ~90 µm were observed, which after 41 days were transformed into finger-like patterns after 148 days; disrupting the hexagonal morphology into parallel lamellar morphology with repeat distance of 9.3 ± 0.3 nm and perpendicular PEO chain stems perpendicular to the film/substrate interface.

Our results demonstrate the extent at which the PEO chains confined into the PI domain breakout from its confinement. In this soft confinement, after nucleation, the crystals grow by chain diffusion through the rubbery matrix. The chains in

rubbery PI matrix are stretched, causing the destruction of the pre-existing morphology.

In the bulk, the process of breakout crystallizations has not been fully visualized and the resulting structures after the breakout were not completely resolved [51-60]. In the present study, in addition to fully resolving the structures before and after breakout crystallization, we could follow the effect of the long time crystallization until the final structures were obtained.

Chapter 5

Strong crystallization confinement

5.1 Aim of work

The aim of this work is to investigate the characteristic behaviours and properties in the crystallization processes which are different from those of the normal crystallization confinement (i.e. the unconfined and soft confined crystallization). Such characteristics behaviour and properties are the crystallinity, the orientation of chains and the chain folding mechanisms.

We followed the crystallization of PEO in a very strong confinement (*hard confinement*). We used a high molar mass PS-*b*-PEO (i.e. molar mass of 109k g/mol each) to prepare thin films and to investigate the PEO crystallization in the strong confinement provided by the glassy amorphous PS. The strong confinement comes from the high T_g of the PS and the strong segregation between the PS and the PEO, i.e. high $T_{,ODT}$ (see appendix A). This high molar mass sample promoted chain entanglement within the film and resulted in low PEO chains diffusion during crystallization. Hence, there were difficulties in forming regular crystals.

Observations were made on the surface and within the thin films. The orientation of the crystals and their influence on the surface morphology were discussed. Two films were prepared and were crystallized at $T_x = 25°C$ and $40°C$.

5.2   Results and discussions

5.2.1 Surface Analysis

In figure 5.1a,b, we observed no distinct changes in the surface morphologies for the two films crystallized at T_x = 25°C and 40°C. Crystallization might have occurred within the strong PS confinement. Alternatively, crystallization of the PEO chains might have been frustrated by the long chain length. The chain length of the fully extended PEO of molar mass 109,000 g/mol is: $\kappa = l_u$N ~ 689 nm (where l_u= 0.2783 nm is the monomer length and the degree of polymerization N = 2477) [110].

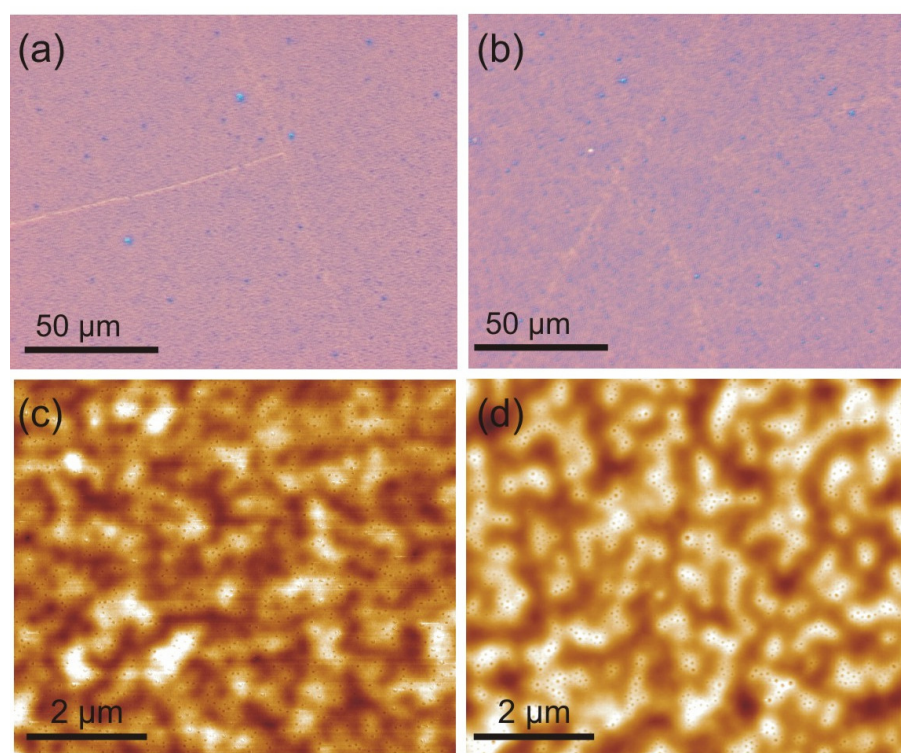**Figure 5.1**. OM images of the films prepared at T_x = 25°C (*a*) and 40°C (*b*). AFM topography images of the films prepared at T_x = 25°C (*c*) and 40°C (*d*). Surface roughness was found to be 3.7 nm for T_x = 25°C and 4.9 nm for T_x = 25°C

A detailed surface analysis on the two films show identical surface textures (Fig. 5.1*c,d*) with almost equal surface roughnesses. The surface textures were not smooth but rather seem undulating.

We conclude that, crystallization was frustrated due to the fact that the PEO chains were quite long, as illustrated in figure 5.2. In this way, it will be very difficult for the long chain to assume several folding conformations (i.e. once-folded, twice-folded etc.). In order to get information on the crystalline structure as well as its orientation to validate the frustrating nature of the long PEO chain crystallization, GIWAXS experiments was performed.
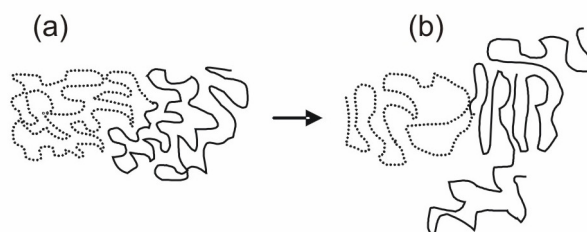
Figure 5.2. Schematic illustration of the chain folding in hard crystallization confinement. (*a*) initial amorphous chains and (*b*) represent frustration in chain folding due to the very long crystallisable chain.

5.2.2. Crystalline orientation

2D GIWAXS images (Fig. 5.3) were obtained for the two films. In all the scattering spectra were not pronounce compared to the spectra obtained for the unconfined crystallization (Fig. 3.9*a,b*). For the film crystallized at $T_x = 25°C$ (Fig. 5.3*a*), we observed isotropic rings which from the *120*, *032*, *-132*, *-212*, and *112* reflections. For films crystallized at $T_x = 40°C$ (Fig. 5.3*b*), we observed a broad isotropic ring as well as some distinct peak intensities from the *120* and *032* reflections.

We conclude that, in all the films there were some degree of crystallites present. However, these crystals were less in number compared to the overall thin films, thus promoting low intensities in the two spectra. At $T_x = 25°C$, crystallization process might be fast and might be highly frustrated since the long PEO chains

cannot come together to form crystals. Hence, chain folding occurred in small number and at different orientations (Fig. 5.4a). For films crystallized at T_x = 40°C, the single broad intensity distributions and the presence of distinct peaks reveal some level of crystalline order. The 2D GIWAXS image can be compared to the simulated spectra obtained in figure 3.9d. Thus, we conclude that there is some order towards the film normal (Fig. 5.4b).
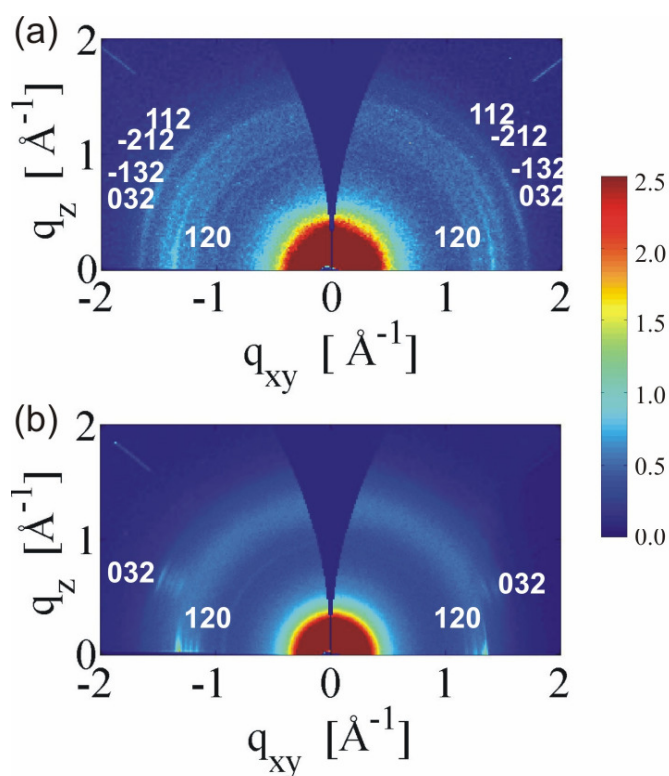
Figure 5.3. 2D GIWAXS images of the films prepared at T_x = 25°C (a) and 40°C (b).
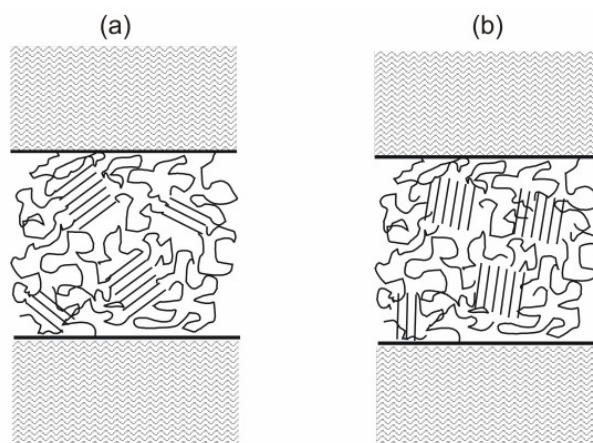
Figure 5.4. Schematic representation of the possible local chain orientation in the films prepared at $T_x = 25°C$ (*a*) and 40°C (*b*).

5.3 Summary

When the long crystallisable chains are strongly confined to noncrystalline medium, adsorption process and diffusion of polymer chains play a major role in the crystallization process. We have noted that under hard confinement, and for long crystallisable chains, diffusion processes to induce growth of a crystal layer were highly hindered. Moreover, it is very difficult for the long chain to fold sereval times to for, crystals. This cannot be compared to the low molar mass PS-*b*-PEO diblock copolymer (i.e. with 3,000 g/mol molar mass each) were diffusion rate of the crystallisable chains were high and hence more nuclear sites were formed. In these high molar mass films, only local movements resulted in the formation of crystals. The surface morphologies were similar suggesting non-dependence of the morphologies on the crystallization temperature. In the near future, in-situ measurements may be employed to study these local movements. Our findings are in good agreement with the bulk studies where PEO-block crystallization kinetics in the hard confinement is much slower than that in the soft confinement [114]. It was noted that the weight percent crystallinity of the PEO crystals in the soft confinement environment were higher than those in the

hard confinement environment which indicated that the PEO crystals developed in the soft confinement environment possess higher thermodynamic stability than in the hard confinement environment.

Chapter 6

Conclusion

Polymer crystallization has been a topic of discussion for the past 50 years, and it will continue to be an active research topic in the future since chemists keep making new polymers and many features are not well understood. Traditional polymer crystallization research is more or less focused on the morphology of the polymer crystals, which are certainly important. Crystallization of block copolymer microdomains can have a tremendous influence on the morphology, properties and applications of these materials. Besides successful applications in surface nanopatterning, efforts have been dedicated to the phase and crystallization behavior of crystalline-amorphous block copolymers forming in different nanoconfined environments, in particular, the crystal (usually the c-axis) orientation has been studied by various ordered phase morphologies.

In this study, the crystallization mechanisms in unconfined, softly confined and strongly confined thin films environment were investigated and the structures formed within the film related to the surface textures obtained.

By combining results from optical and atomic-force microscopy, as well as grazing-incidence X-ray scattering methods, a detailed view of the surface and internal structure of our semicrystalline thin films could be obtained providing essential information for improved understanding of polymer crystallization.

For unconfined crystallization, three thin films from a symmetric low molar mass Poly(styrene-b-ethyleneoxide) (PS-b-PEO) diblock copolymer were rystallized at three different temperatures. The crystal growth rates, the resulting surface textures and the orientation of the PEO chain were vastly different. At low crystallization temperature (room temperature), the crystal growth rate is high but

the crystals grow with a mean inclination angle of 35° from the film normal, building small, slightly differently oriented crystalline domains along the growth front. These growth mechanisms are attributed to repeated nucleation events at the growth front as demonstrated previously in phase-field simulations. It promotes a granular and comparatively rough surface texture. At high crystallization temperature, i.e. temperature just below the melting point, only very few nuclei are formed, and the crystal growth rate is low. Large crystallites grow with the chain stems perpendicular to the film normal. The high mobility of both blocks at this elevated temperature enables the lateral diffusion of the chains towards the growth front promoting large crystalline domains. The resulting surface morphologies consist of terraces with height comparable to a monolayer of once-folded PEO block oriented perpendicular to the substrate plane. Films crystallized at 40°C represented an intermediate case between films crystallized at 25°C and 50°C. The surface morphologies and the growth rates were comparable to films crystallized at 25°C but the lamellar repeat distance was similar to the film crystallized at 50°C. This was attributed to the PEO stems might having intermediate orientations between films crystallized at 25°C and 50°C.

For the crystallization with soft confinement, one thin film was prepared from a low molar mass poly(isoprene-*b*-ethyleneoxide) (PI-*b*-PEO) diblock copolymer. The PEO blocks form hexagonally arranged cylinders lying in the film plane confined in the PI matrix. The PI matrix, which is rubbery, provides a soft confinement. The nucleation rate for crystal formation was low, which we attribute to the confinement of the short PEO chains. Crystallization of the PEO chains, once nucleated, causes destruction of the hexagonal morphology and transforms it into lamellar morphology. This process is only completed after 148 days. The repeat distances before and after crystallization as well as the surface terrace height are comparable which suggest the presence of well defined repeat distances within the thin films.

To investigate the *strongly confined crystallization*, two thin films from a symmetric high molar mass PS-*b*-PEO diblock copolymer were prepared and were crystallized at two different temperatures. The surface morphologies did not

change with temperature. With this long PEO chain, it was difficult for the chains to fold several times to form crystals. Moreover, the glassy amorphous PS hinders the chain diffusion. Only local movements of the chains allowed some ordering of these chains to form crystals within the films.

This present studies have provided new understanding in crystallization of polymers under different nano-confinement and the associated crystallization mechanisms.

Our observations show that a detailed structural analysis can explain the observed surface morphologies and relate them to the different mechanisms of crystal growth. The thin film geometry used offers an ideal possibility to correlate detailed structural analyses on various length scales with the direct-space observation of crystal growth via microscopy techniques. These research topics are fundamental with a direct impact on applications using block copolymers as templates or inorganic/organic hybrids and have contributed to the understanding of polymer crystallization.

Bibliography

[1]   F. S. Bates, and G. H. Fredrickson. *Annu. Rev. Phys. Chem.*, 41:525, 1990.

[2]   H.-G. Elias. *An Introduction to Polymer Science*, p. 294, VCH publishers, Weinheim, New York, 1997.

[3]   L. H. Sperling. *Introduction to Physical Polymer Science*, 3rd Ed., p. 40, Wiley, New York, 2001.

[4]   N. Hadjichristidis, S. Pispas, and G. Floudas. *Block Copolymers: Synthetic Strategies, Physical Properties, and Applications*, John Wiley & Sons, New Jersey, 2003.

[5]   I. W. Hamley. *Block Copolymers in Solution: Fundamentals and Application*, John Wiley & Sons, England, 2005.

[6]   A. P. Smith, J. F. Douglas, J. C. Meredith, E. J. Amis, and A. Karim. *Phys. Rev Lett*. 87: 015503-1, 2001.

[7]   S.-J. Jeong, G. Xia, B. H. Kim, D. O. Shin, S-H. Kwon, S.-W. Kang, and S. O. Kim. *Adv. Mater.*, 9999:1, 2008.

[8]   M. Park, C. Harrison, P. M. Chaikin, R. A. Register, D. H. Adamson. *Science*, 276:1401, 1997.

[9]   R. R. Li, P. D. Dapkus, M. E. Thompson, W. G. Jeong, C. Harrison, P. M. Chaikin, R. A. Register, D. H. Adamson. *Appl. Phys. Lett*., 76:1689, 2000.

[10]   T. Thurn-Albrecht, J. Schotter, G. A. Kästle, N. Emley, T. Shibauchi, L. Krusin-Elbaum, K. Guarini, C. T. Black, M. T. Tuominen, T. P. Russell. *Science* 290:2126, 2000.

[11]   W. A. Lopes and H. M. Jaeger. *Nature*, 414:735, 2001.

[12]   J. Y. Cheng, C. A. Ross, V. Z.-H. Chan, E. L. Thomas, R. G. H. Lammertink, and G. J. Vancso. *Adv. Mater.* 13:1174, 2001.

[13]   V. Z.-H. Chan, J. Hoffman, V. Y. Lee, H. Iatrou, A. Avgeropoulos, N. Hadjichristidis, R. D. Miller, and E. L. Thomas. *Science*, 286:1716, 1999.

[14]   C. T. Black, K. W. Guarini, K. R. Milkove, S. M. Baker, T. P. Russell, and M. T. Tuominen. *Appl. Phys*. Lett., 79:409, 2001.

[15]   B.H. Sohn and S.H. Yun. *Polymer*, 43:2507, 2002.

[16]   P. Busch, D. Posselt, D.-M. Smilgies, M. Rauscher, and C. M. Papadakis. *Macromolecules*, 40:630, 2007.

[17]   M. W. Matsen. *Macromolecules* 39:5512, 2006.

[18]   V. Olszowka, M. Hund, V. Kuntermann, S. Scherdel, L. Tsarkova, A. Böker, and G. Krausch, *Soft Matter 2*, 12:1089, 2006.

[19]   M. A. Hillmyer and F. S. Bates. *Macromol. Symp.*, 117:121, 1997.

[20]   D. J. Quiram, R. A. Register, G. R. Marchand, and D. H. Adamson. *Macromolecules*, 31:4891, 1998.

[21]   I. W. Hamley, J. P. A. Fairclough, F. S. Bates, and A. J. Ryan. *Polymer*, 39:1429, 1998.

[22]   I. W. Hamley. *Adv Polym Sci.*, 148:114, 1999.

[23]   P. Huang, L. Zhu, S. Z. D. Cheng, Q. Ge, R. P. Quirk, E. L. Thomas, B. Lotz, B. S. Hsiao, L. Liu, and F. Yeh. *Macromolecules*, 34:6649, 2001.

[24]   Y. L. Loo, R. A. Register, and A. J. Ryan. *Macromolecules*, 35:2365, 2002.

[25]   H. L. Chen, H. C. Li, Y. Y. Huang, and F. C. Chiu. *Macromolecules*, 35:2417, 2002.

[26]   W. H. de Jeu, In *Lecture Notes in Physics: Polymer Crystallization*: *Observations, Concepts and Interpretations*, edited by G. Reiter and J.-U. Sommer, p. 196. Springer, Berlin, 2003.

[27]   H. Takeshita, N. Ishii, C. Araki, M. Miya, K. Takenaka, and T. Shiomi. *J. Polym. Sci. Part B: Polym. Phys*., 42:4199, 2004.

[28]   Y. L. Loo, and R.A. Register. In *Developments in Block Copolymer Science and Technology*, edited by I. W. Hamley, p 213, Wiley, New York, 2004.

[29]   A. J. Müller, V. Balsamo, and M. L. Arnal. *Adv. Polym. Sci*., 190:1, 2005.

[30]   L. Li, Y. Séréro, M. H. J. Koch, and W. H. de Jeu. *Macromolecules*, 36:529, 2003.

[31]   G. Strobl. *The Physics of Polymers*, 2nd ed. Springer, Berlin, 1997.

[32]   L. H. Sperling. *Introduction to Physical Polymer Science*, Wiley, New York, 1986.

[33]   K. Armistead and G. Goldbeck-Wood. *Adv. Polym. Sci*., 100:219, 1992.

[34]   N. Okui. *Polymer Journal*, 19:1309, 1987.

[35]   N. Okui. *J. Mater. Sci*., 25:1623, 1990.

[36]   S. Umemoto and N. Okui. *Polymer*, 43:1423, 2002.

[37]   J. Brandrup and E.H. Immergut. *Polymer Handbook*, 3rd Edition, 1989.

[38]   K. Mortensen, W. Brown, K. Almdal, E. Alami, A. Jada, *Langmuir*, 13:3635, 1997.

[39] L. Zhu, S. Z. D. Cheng, B. H. Calhoun, Q. Ge, R. P. Quirk, E. L. Thomas, B. S. Hsiao, F. Yeh, and B. Lotz. *J. Am. Chem. Soc.*, 122:5957, 2000.

[40] L. Zhu, P. Huang, W. Y. Cheng. Q. Ge, R. P. Quirk, S. Z. D. Cheng, E. L. Thomas, B. Lotz, B. S. Hsiao, F. Yeh, and L. Liu. *Macromolecules*, 35:3553, 2002.

[41] L. Zhu, S. Z. D. Cheng, P. Huang, Q. Ge, R. P. Quirk, E. L. Thomas, B. Lotz, B. S. Hsiao, F. Yeh, and L. Liu. *Advanced Materials*, 14:31, 2002.

[42] T. Shiomi, H. Takeshita, H. Kawaguchi, M. Nagai, K. Takenaka, and M. Miya. *Macromolecules*, 35:8056, 2002.

[43] L. Sun, L. Zhu, Q. Ge, R. P. Quirk, C. Xue, S. Z. D. Cheng, B. S. Hsiao, C. A. Avila-Orta, I. Sics, and M. E. Cantino. *Polymer*, 45:2931, 2004.

[44] G. Reiter and J.-U. Sommer. *Phys. Rev. Lett.*, 80 :3771, 1998.

[45] R. Opitz, D. M. Lambreva, and W. H. de Jeu. *Macromolecules*, 35:6930 2002.

[46] G.-D. Liang, J. -T. Xu, Z. -Q. Fan, S. -M. Mai, and A. J. Ryan, *Macromolecules*, 39 :5471, 2006.

[47] G. Reiter, I. Botiz, L. Graveleau, N. Grozev, K. Albrecht, A. Mourran, and M. Möller, In *Lecture Notes in Physics 714: Progress in Understanding of Polymer Crystallization*, edited by G. Reiter and G. R. Strobl, p. 179. Springer, Berlin, 2007.

[48] G. Reiter. *J. Polym. Sci. Part B: Polym. Phys.*, 41:1869, 2003.

[49] G. Reiter, and L. Vidal. *Eur. Phys. J. E.* 12:497, 2003.

[50] G. Reiter, G. Castelein, and J.-U. Sommer. In *Lecture Notes in Physics: Polymer Crystallization*: *Observations, Concepts and Interpretations*, edited by G. Reiter and J.-U. Sommer, p. 131. Springer, Berlin, 2003.

[51]   A. J. Ryan, I. W. Hamley, W. Bras, and F. S. Bates. *Macromolecules*, 28:3860, 1995.

[52]   M. A. Hillmyer, and F. S. Bates. *Macromol. Symp.*, 117:121, 1997.

[53]   D. J. Quiram, R. A. Register, and G. R. Marchand. *Macromolecules*, 30:4551, 1997.

[54]   G. Floudas, R. Ulrich, and U.Wiesner. *J. Chem. Phys.*, 110:652, 1999.

[55]   J. –T. Xu, J. P. A. Fairclough, S.-M. Mai, A. J. Ryan, and C. Chaibundit. *Macromolecules*, 35:6937, 2002.

[56]   Y. -L. Loo, R. A. Register, and A. J. Ryan. *Macromolecules*, 35:2365, 2002.

[57]   J.-T. Xu, , J. P. A. Fairclough, S.-M. Mai, C. Chaibundit, M. Mingvanish, C. Booth, and A. J. Ryan. *Polymer* 44:6843, 2003.

[58]   L. Li, Y. Séréro, M. H. J. Koch, and W. H. De Jeu. *Macromolecules*, 36:529, 2003.

[59]   R.-M.. Ho, T.-M. Chung, J.-C. Tsai, J.-C. Kuo, B. S. Hsiao, and I. Sics. *Macromol. Rapid Commun.*, 26:107, 2005.

[60]   D. M. Lambreva, R. Opitz, G. Reiter, P. M. Frederik, and W. H. De Jeu. *Polymer*, 46:4868, 2005.

[61]   J. Lee, M. Christopher Orilall, S. C. Warren, M. Kamperman, F. J. Disalvo, and U. Wiesner. *Nature Materials*, 7:222, 2008.

[62]   L. Zhu, Y. Chen, A. Zhang, B. H. Calhoun, M. Chun, R. P. Quirk, S. Z. D. Cheng, B. S. Hsiao, F. Yeh, and T. Hashimoto. *Phys. Rev. B*, 60:10022, 1999.

[63]   T. Miura, and M. Mikami. *Phys. Rev. E*, 75:031804, 2007.

[64] H. Frielinghaus1, N. Hermsdorf, K. Almdal, K. Mortensen, L. Messé, L. Corvazier, J. P. A. Fairclough, A. J. Ryan, P. D. Olmsted, and I. W. Hamley. *Europhys. Lett.*, 53:680, 2001.

[65] G. Floudas, B. Vazaiou, F. Schipper, R. Ulrich, U. Wiesner, H. Iatrou, and N. Hadjichristidis. *Macromolecules*, 34:2947, 2001.

[66] N. Hadjichristidis, S. Pispas, and G. Floudas. *Block Copolymers: Synthetic Strategies, Physical Properties, and Applications*, pp. 292 – 297, John Wiley & Sons, New Jersey, 2003.

[67] J. H. Richardson. *Optical microscopy for the materials sciences*, Dekker, New York, 1971.

[68] S. Morita. *Noncontact atomic force microscopy*, Springer Verlag, Berlin, 2002.

[69] V. J. Morris, A. R. Kirby, and A. P. Gunning. *Atomic force microscopy for biologists*, Imperial College Pr., London, 1999.

[70] H. G. Tompkins. *Handbook of ellipsometry*, Springer, Heidelberg, 2005.

[71] G. W. H. Höhne, W. Hemminger, H.-J. Flammersheim. *Differential scanning calorimetry*, 2nd ed., Springer, Berlin, 2003.

[72] V. Holý, U. Pietsch, T. Baumbach. *High-Resolution X-ray Scattering from Thin Films and Multilayers*, Springer, Berlin, 1999.

[73] U. V. Desnica, P. Dubcek, I. D. Desnica-Frankovic, M. Buljan, K. Salamon, O. Milat, S. Bernstorff, and C. W. White. In *Nuclear Instruments and Methods in Physics Research Section B: Beam Interactions with Materials and Atoms*, pp. 191-195, Elsevier publishers, 2003.

[74] C. Revenant, F. Leroy, R. Lazzari, G. Renaud, and C. R. Henry. *Phys. Rev. B*, 69:035411, 2004.

[75] P. Müller-Buschbaum. In Polymer Surfaces and Interfaces: Characterization, Modification and Applications, edited by M. Stamm, pp. 17-46, Springer Berlin, 2008.

[76] M. W. Tate, E. F. Eikenberry, S. L. Barna, M. E. Wall, J. L. Lowrance, and S. M. Gruner. *J. Appl. Cryst.*, 28:196, 1995.

[77] D. J. Thiel, S. E. Ealick, M. W. Tate, S. M. Gruner, and E. F. Eikenberry. *Rev. Sci. Instr.*, 67:3361, 1996.

[78] S. K. Sinha, E. B. Sirota, S. Garoff, and H. B. Stanley. *Phys. Rev. B*, 38:2297, 1988.

[79] M. Rauscher, T. Salditt, and H. Spohn. *Phys. Rev. B*, 52:16855, 1995.

[80] S. V. Roth, R. Döhrmann, M. Dommach, M. Kuhlmann, I. Kröger, R. Gehrke, H. Walter, C. Schroer, B. Lengeler, P. Müller-Buschbaum, *Rev. Sci. Instr.*, **77**:085106, 2006.

[81] D.-M. Smilgies, P. Busch, D. Posselt, and C. M. Papadakis. *Synchrotron Radiation News*, 15(5):35, 2002.

[82] B. Lengeler, C. G. Schroer, M. Kuhlmann, B. Benner, T. F. Günzler, O. Kurapova, F. Zontone, A. Snigirev, and I. Snigireva. *J. Phys. D: Appl. Phys.*, 38:A218, 2005.

[83] M. N. Groves, M. A. Singh, G. Beydaghyan, M. S. Muller, E. Sheridan, and D. K. Schneider. *J. Appl. Cryst.*, 39:120, 2006.

[84] G. Vineyard. *Phys. Rev. B*, 26:4146, 1982.

[85] V. Holý, J. Kubena, I. Ohlidal, K. Lischka, and W. Plotz. *Phys. Rev. B*, 47:15896, 1993.

[86] J. Stettner, L. Schwalowsky, O.H. Seeck, M. Tolan, W. Press, C. Schwarz, and H. v. Känel. *Phys. Rev. B*, 53:1398, 1996.

[87]   V. Holý and T. Baumbach. *Phys. ReV. B*, 49:10668, 1994.

[88]   P. Busch, M. Rauscher, D. -M. Smilgies, D. Posselt, and C. M. Papadakis. *J. Appl. Cryst.*, 39:433, 2006.

[89]   P. Busch, D. Posselt, D. -M. Smilgies, M. Rauscher, and C.M. Papadakis. *Macromolecules*, 40:630, 2007.

[90]   J. Als-Nielsen and D. McMorrow. *Elements of Modern X-ray Physics*, John Wiley and Sons, New York, 2001.

[91]   D. Apitz, R. P. Bertram, N. Benter, W. Hieringer, J. W. Andreasen, M. M. Nielsen, P. M. Johansen, and K. Buse. *Phys. Rev. E.*, 72:036610, 2005.

[92]   O. Bunk and M. M. Nielsen. *J. Appl. Cryst.*, 37:216, 2004.

[93]   D. W. Breiby, O. Bunk, W. Pisula, T. I. Sølling, A. Tracz, T. Pakula, K. Müllen, and M. M. Nielsen. *J. Am. Chem. Soc.*, 127:11288, 2005.

[94]   D. W. Breiby, F. Hansteen, W. Pisula, O. Bunk, U. Kolb, J. W. Andreasen, K. Müllen, and M. M. Nielsen. *J. Phys. Chem. B*, 109:22319, 2005.

[95]   D. W. Breiby and E. J. Samuelsen. *J. Polym. Sci.Part B: Polym. Phys.*, 41:2375, 2003.

[96]   D. W. Breiby, S. Sato, E. J. Samuelsen, and K. Mizoguchi. *J. Polym. Sci. B: Polym Phys.*, 41:3011, 2003.

[97]   D. W. Breiby, O. Bunk, J. W. Andreasen, H. T. Lemke, and M. M. Nielsen. *J. Appl. Cryst.*, 41:262, 2008.

[98]   Y. Takahashi and H. Tadokoro. *Macromolecules*, 6:672, 1973.

[99]   O. Kratky. *Colloid Polym. Sci.*, 64:213, 1933.

[100]   A. Guinier. *X-Ray Diffraction*, pp. 121-126, San Francisco, 1963.

[101] J. Daillant, and A. Gibaud. *X-ray and neutron reflectivity; principles and applications*, Springer, Berlin, 1999.

[102] http://www.ncnr.nist.gov/resources/sldcalc.html.

[103] T. Hugel, G. Strobl, and R. Thomann. *Acta Polymerica*, 50:214, 1999.

[104] L. Gránásy, T. Pusztai, T. Börzsönyi, J. A. Warren, and J. F. Douglas. *Nature Materials*, 3:645, 2004.

[105] T. Hippler, S. Jiang, and G. Strobl. *Macromolecules*, 38:9396, 2005.

[106] I. W. Hamley, J. P. A. Fairclough, N. J. Terrill, A. J. Ryan, P. M. Lipic, F. S. Bates, and E. Towns-Andrews. *Macromolecules*, 29:8835, 1996.

[107] G. Reiter, G. Castelein, P. Hoerner, G. Riess, J.-U. Sommer, and G. Floudas. *Eur. Phys. J. E*, 2:319, 2000.

[108] J. Huang, M. S. Lisowski, J. Runt, E. S. Hall, R. T. Kean, N. Buehler, J. S. Lin. *Macromolecules*, 31:2593, 1998.

[109] Y. He, Z. Fan, J. Wei, and S. Li. *Polym. Eng. & Sci*, 46:1583, 2006.

[110] A. Kovacs, C. Straupe, and A. Gonthier. *J. Polm. Sci. B, Polym. Symp.*, 59:31, 1977.

[111] S. Hong, L. Yang, W. J. Macknight, and S. P. Gido. *Macromolecules*, 34:7009, 2001.

[112] J.–U. Sommer, and G. Reiter. *Lecture Notes in Physics: Polymer Crystallization: Observations, Concepts and Interpretations*, edited by G. Reiter and J.-U. Sommer, Springer, Berlin, 2003.

[113] G. Strobl, and G. R. Reiter. *Lecture Notes in Physics 714: Progress in Understanding of Polymer Crystallization*; p 1., Springer, Berlin, 2007.

[114] L. Zhu, B. R. Mimnaugh, Q. Ge, R. P. Quirk, S. Z. D. Cheng, E. L. Thomas, B. Lotz, B. S. Hsiao, F. Yeh, and L. Liu. *Polymer*, 42:9121, 2001.

Appendix A

Calculation of the ODT temperature

From H. Frielinghaus et. al., Europhys. Lett, 53, 680, 2001, the Flory-Huggins interaction parameter, χ, for PS-*b*-PEO is described by;

$$\chi = 29.8 \text{ K}/T - 0.0229$$

based on a common segment volume of 70.5 cm^3/mol

Mean-field prediction for order-to-disorder transition: $\chi N = 10.5$

$$\text{i.e. } T_{\text{ODT}} = (29.8 \text{ K} \times N) / (10.5 + 0.0229 \times N)$$

Calculation of the molar volume for PS-*b*-PEO 3k-3k molar masses:

Molar volume of PS-monomer:

$$= M/\rho = (104 \text{ g/mol}) / (1.05 \text{ g/mol}) = 99.05 \text{ cm}^3/\text{mol}$$

(where, M = Molar mass and ρ = density)

Molar volume of PS-block ($N_{\text{PS}} = 29$, for 3,000 g/mol):

$$V_{\text{PS-block}} = 29 \times 99.05 = 2872.5 \text{ cm}^3/\text{mol}$$

Molar volume of PEO-monomer

$$= (44 \text{ g/mol}) / (1.229 \text{ g/mol}) = 35.8 \text{ cm}^3/\text{mol}$$

Molar volume of PEO-block ($N_{\text{PS}} = 68$, for 3,000 g/mol):

$$V_{\text{PEO-block}} = 68 \times 35.8 = 2434.4 \text{ cm}^3/\text{mol}$$

Total PS-PEO volume:

$$V_{\text{PS-PEO}} = 2872.5 + 2434.4 = 5306.9 \text{ cm}^3/\text{mol}$$

Calculation of degree of polymerization N

Common segment volume of 70.5 cm^3/mol (see Frielinghaus et. al., 2001)

$$N = V_{PS-PEO}/70.5 = 5306.9/70.5 = 75.3$$

ODT calculation

Therefore, $T_{ODT} = (29.8 \text{ K} \times N) / (10.5 + 0.0229 \times N) = 183.5 \text{ K} = -90°C$

Hence, for PS-*b*-PEO;

$$T_{ODT} = 184 \text{ K} = -90°C \text{ for 3k-3k}$$

$$T_{ODT} = 1114 \text{ K} = 841°C \text{ for 109k-109k}$$

Appendix B

Calculation of the crystalline domain size

Using the Scherrer's formula,

$$D_{hkl} = \frac{0.9 \times \lambda}{\beta \times \cos \alpha_i}$$

Full width at half maximum, FWHM, for direct beam

$$= 0.066°$$

Full width at half maximum, FWHM, for 120 reflection from the USEO25 film

$$= 0.07889°$$

Calculating the crystalline domain sizes (D_{hkl});

The FWHM of the direct beam was subtracted from the *120* FWHM
(i.e. 0.14489 – 0.066 = 0.07889°)

β = 0.14489 – 0.066 = 0.07889 °

     = 0.07889 × (3.142/180) radians

     = 0.00137689 radians

$\cos\alpha_i$ = (0.16/2)= 0.9999

λ = 0.124 nm

D_{hkl} ~ 81nm

A Symbols and abbreviations

Here is a list of the used symbols and abbreviations.

PS   Polystyrene block

PEO   Polyethyleneoxide block

T_g Glass transition temperature

T_m Melting temperature

$T_{g,PS}$ Glass transition temperature of polystyrene block

$T_{g,PEO}$ Glass transition temperature of polyethyleneoxide block

$T_{m,PEO}$ Melting temperature of polyethyleneoxide block

T_x Crystallization temperature

$T_m°$ Equilibrium melting temperature

N_1 degree of polymerization of PS

N_2 degree of polymerization of PEO

M_1 degree of polymerization of PI

A   amorphous domain

B   Crystalline domain

D Single layer repeat units (A and B)

L Double layer repeat units (period)

h Thin film thickness

n   Integer

ODT   Order-disorder transition

$T_{,ODT}$ Order-disorder transition temperature

DBM   Densily branched morphology

OM   Optical microscopy

AFM   Atomic-force microscopy

TM-AFM   Tapping mode atomic force microscopy

Δ   Relative phase change

Ψ   Relative amplitude change

$\tilde{R}_p$	Amplitudes of the *s* (oscillating perpendicular to the plane of incidence) component
$\tilde{R}_s$	Amplitudes of the *p* (oscillating parallel to the plane of incidence) component.
$n_{polymer}$	Polymer refractive index
DSC	Differential scanning calorimetry
GISAXS	Grazing-incidence small-angle X-ray Scattering
GIWAXS	Grazing-incidence wide-angle X-ray Scattering
GIXD	Grazing-incidence X-ray Diffraction
χ_f	Flory-Huggins interaction parameter
q_z	Scattering components of the scattering vector perpendicular to the sample surface
α_i	Incident angle
D_{hkl}	Crystalline domain
β	Peak width in radians
α_{cp}	Critical angle of the polymer
λ	wavelength
q_y	lateral components of the scattering vector used in the detector coordinates
α_f	Exit angle
α_{sio2}	Critical angle of the silicon substrate surface
k_{iz}	Vertical component of the incident wave vector
$\lambda_{Cu,k\alpha}$	wavelength of X-ray generated by Copper K-alfa radiation
DWBA	Distorted-wave Born approximations
m	Order of reflections in the DWBA repeat unit estimations
$P2_1/a\text{-}C_{2h}^5$	Space group symbol for the monoclinic lattice
c-axis	*c*-components of the monoclinic unit cell
χ	Angle between the film normal and the orientation of the *c*-axis
ODF	Orientational distribution function, f(χ)
λ_K	Elongation ratio

ξ Orientation degree of the monoclinic unit cell along the vertical

   axis (*c*-axis)

ϕ.   Orientation degree of the monoclinic unit cell along the film

   Normal

S   Position of the specular peak

δ   Crystalline domain size

κ Fully extended chain length

M   Molar mass of sample

ρ density

$V_{\text{PS-block}}$ Molar volume of PS

$V_{\text{PEO-block}}$ Molar volume of PEO

$V_{\text{PS-PEO}}$ Total volume of PS-b-PEO diblock copolymer

N   Degree of polymerization of a polymer
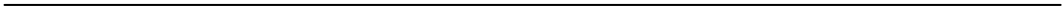
B Publications and presentations

B1 Publications

E. Metwalli, U. Slotta, **C. Darko**, S. V. Roth, T. Scheibel, C. M. Papadakis: "*Structural changes of thin films from recombinant spider silk proteins upon post-treatment*", **Appl. Phys. A** 89, 655-661 (2007).

K. Troll, A. Kulkarni, W. Wang, **C. Darko**, A.M.B. Koumba, A. Laschewsky, P. Müller-Buschbaum, C.M. Papadakis: "*The Collapse Transition of Poly(styrene-b-(Nisopropyl acrylamide)) Diblock Copolymers in Aqueous Solution and in Thin Films*", **Colloid and Polymer Science**, in print.

C. M. Papadakis, Z. Di, **C. Darko**, D. Posselt, D. -M. Smilgies, M. A. Singh: "*The Effect of Heat Treatment on the Internal Structure of Nanostructured Block Copolymer Films*", **Lecture Notes in Physics: Applications of Synchrotron Light to Non-Crystalline Diffraction in Materials and Life Sciences**, edited by M. C. García-Gutierrez, A. Nogales, M. Gómez and T. A. Ezguerra, in print.

C. Darko, I. Botiz, G. Reiter, D.W. Breiby, J. W. Andreasen, S.V. Roth, D.-M. Smilgies, E. Metwalli1, C.M. Papadakis: "*Influence of the crystalline growth kinetics on the mesoscopic structure and the crystalline orientation in thin diblock copolymer films*", **Phys. Rev. Lett.**, to be submitted.

C. Darko, I. Botiz, G. Reiter, D.W. Breiby, J. W. Andreasen, S.V. Roth, D.-M. Smilgies, E. Metwalli, C.M. Papadakis: "*Surface & internal structures of thin diblock copolymer films crystallized at different temperatures*", **Eur. Phys. J. E**, to be submitted.

C. Darko, K. Troll, Z. Di, D.-M. Smilgies, A. Timmann, S. Förster, C. M. Papadakis: "*Breakout Crystallization in PI-b-PEO Diblock Copolymer Thin Films*", **Macromolecules**, to be submitted.

B2   Presentations

Annual Hasylab Users' Meeting: "*Thin films of diblock copolymers having one crystalline block*", January 2008, Hamburg, Germany (POSTER).

Annual Hasylab Users' Meeting: "*Breakout Crystallization in PI-b-PEO Diblock Copolymer Thin Films*", January 2008, Hamburg, Germany (POSTER).

FRM II Workshop: *"Thin Films of Crystalline Diblock Copolymers*: Studied by GISAXS, GIWAXS & GIXD", July 2007, Rothenfels, Germany (TALK).

Annual meeting of the German Physical Society: "*Thin Films of Crystalline Diblock Copolymers: Structure and Nano-pore Formation*", March 2007, Regensburg, Germany (POSTER).

Edgar-Lüscher Seminar: "*Thin Films of Crystalline Diblock Copolymers*", February 2007, Klosters, Switzerland (POSTER).

Annual Hasylab Users' Meeting: "*Thin Films of Diblock Copolymers having One Crystalline Block*", January 2007, Hamburg, Germany (POSTER).

COST P12 Conference on Crystallisation and Structure Formation of Polymers: "*Thin Films of Crystalline Diblock Copolymers*", 9-11 October 2006, Mittelwihr Center, France (TALK).

National Conference on Research with Synchrotron Radiation, Neutrons and Ions (SNI): "*Thin Films of Crystalline Diblock Copolymers*", 5 - 6 October 2006, Hamburg, Germany (POSTER).

Annual meeting of the German physical society: "*Thin Films of Crystalline Diblock Copolymers*", March 2006, Dresden, Germany (POSTER).

Annual Hasylab Users' Meeting: "*Thin Films of Diblock Copolymers having One Crystalline Block*", January 2006, Hamburg, Germany (POSTER).